

May 2014

Wetting, Superhydrophobicity, and Icephobicity in Biomimetic Composite Materials

Vahid Hejazi

University of Wisconsin-Milwaukee

Follow this and additional works at: <https://dc.uwm.edu/etd>

 Part of the [Materials Science and Engineering Commons](#), [Mechanical Engineering Commons](#), and the [Physical Chemistry Commons](#)

Recommended Citation

Hejazi, Vahid, "Wetting, Superhydrophobicity, and Icephobicity in Biomimetic Composite Materials" (2014). *Theses and Dissertations*. 529.

<https://dc.uwm.edu/etd/529>

This Dissertation is brought to you for free and open access by UWM Digital Commons. It has been accepted for inclusion in Theses and Dissertations by an authorized administrator of UWM Digital Commons. For more information, please contact open-access@uwm.edu.

WETTING, SUPERHYDROPHOBICITY, AND
ICEPHOBICITY IN BIOMIMETIC COMPOSITE
MATERIALS

by

Vahid Hejazi

A Dissertation Submitted in
Partial Fulfillment of the
Requirements for the Degree of
Doctor of Philosophy
in Engineering

at

The University of Wisconsin-Milwaukee

May 2014

ABSTRACT
WETTING, SUPERHYDROPHOBICITY, AND
ICEPHOBICITY IN BIOMIMETIC COMPOSITE
MATERIALS

by

Vahid Hejazi

The University of Wisconsin-Milwaukee, 2014
Under the Supervision of Professor Michael Nosonovsky

Recent developments in nano- and bio-technology require new materials. Among these new classes of materials which have emerged in the recent years are biomimetic materials, which mimic structure and properties of materials found in living nature. There are a large number of biological objects including bacteria, animals and plants with properties of interest for engineers. Among these properties is the ability of the lotus leaf and other natural materials to repel water, which has inspired researchers to prepare similar surfaces. The Lotus effect involving roughness-induced superhydrophobicity is a way to design nonwetting, self-cleaning, omniphobic, icephobic, and antifouling surfaces. The range of actual and potential applications of superhydrophobic surfaces is diverse including optical, building and architecture, textiles, solar panels, lab-on-a-chip, microfluidic devices, and applications requiring antifouling from biological and organic contaminants.

In this thesis, in chapter one, we introduce the general concepts and definitions regarding the wetting properties of the surfaces. In chapter two, we develop novel models and conduct experiments on wetting of composite materials. To design sustainable superhydrophobic metal matrix composite (MMC) surfaces, we suggest using hydrophobic reinforcement in the bulk of the material, rather than only at its surface. We experimentally study the wetting properties of graphite-reinforced Al- and Cu-based composites and conclude that the Cu-

based MMCs have the potential to be used in the future for the applications where the wear-resistant superhydrophobicity is required.

In chapter three, we introduce hydrophobic coating at the surface of concrete materials making them waterproof to prevent material failure, because concretes and ceramics cannot stop water from seeping through them and forming cracks. We create water-repellant concretes with CA close to 160° using superhydrophobic coating.

In chapter four, experimental data are collected in terms of oleophobicity especially when underwater applications are of interest. We develop models for four-phase rough interface of underwater oleophobicity and develop a novel approach to predict the CA of organic liquid on the rough surfaces immersed in water. We investigate wetting transition on a patterned surface in underwater systems, using a phase field model. We demonstrated that roughening on an immersed solid surface can drive the transition from Wenzel to Cassie-Baxter state. This discovery improves our understanding of underwater systems and their surface interactions during the wetting phenomenon and can be applied for the development of underwater oil-repellent materials which are of interest for various applications in the water industry, and marine devices.

In chapter five, we experimentally and theoretically investigate the icephobicity of composite materials. A novel comprehensive definition of icephobicity, broad enough to cover a variety of situations including low adhesion strength, delayed ice crystallization, and bouncing is determined. Wetting behavior and ice adhesion properties of various samples are theoretically and experimentally compared. We conclude superhydrophobic surfaces are not necessarily icephobic. The models are tested against the experimental data to verify the good agreement between them. The models can be used for the design of novel superhydrophobic, oleophobic, omniphobic and icephobic composite materials.

Finally we conclude that creating surface micro/nanostructures using mechanical abrasion or chemical etching as well as applying low energy materials are the most simple, inexpensive, and durable techniques to create superhydrophobic, oleophobic, and icephobic materials.

© Copyright by Vahid Hejazi, 2014
All Rights Reserved

*This dissertation is dedicated to my loving parents for their
encouragement, care, support, and patience, and to my brothers who
have never left my side throughout these years*

Acknowledgement

I would like to formally thank:

Dr. Michael Nosonovsky, my research advisor, for his support, excellent guidance, and great advice during past three years. I have learned so much during the course of this PhD, and without him, this would not have been possible.

Dr. Pradeep Rohatgi, Dr. Rioychi Amano, Dr. Konstantin Sobolev, and Dr. Junhong Chen for serving on my dissertation committee. They really helped me with their valuable insight and guidance.

Table of Contents

ABSTRACT	ii
List of Figures.....	x
List of Tables.....	xv
CHAPTER ONE	1
1. INTRODUCTION.....	1
1.1. Biomimetic surfaces.....	5
1.1.1. Superhydrophobic materials in living nature.....	9
1.1.2. Lotus effect and self-cleaning	13
1.1.3. Self-lubrication and self-healing.....	14
1.2. General principles of wetting.....	16
1.2.1. Interfacial energy and surface tension.....	16
1.2.2. Polar and non-polar substances and intermolecular forces.....	18
1.3. Contact angle and superhydrophobicity.....	19
1.3.1. Smooth surface	20
1.3.2. Wenzel model.....	21
1.3.3. Cassie-Baxter model	23
1.4. Contact angle hysteresis.....	26
1.5. The phenomenon of superhydrophobicity.....	26
1.6. Composite materials and surfaces	29
1.6.1. Types of composite materials.....	31
1.6.2. Surface of composite materials.....	34
CHAPTER TWO	36
2. METAL MATRIX COMPOSITES (MMCs).....	36
2.1. Methods of MMC fabrication.....	36
2.2. Modeling of wetting.....	38
2.3. Experimental.....	42
2.3.1. Sample preparation.....	43
2.3.2. Sample characterization	44
2.3.3. Contact angle measurement.....	45
2.4. Superhydrophobicity discussion	46
2.5. Effect of wear on superhydrophobicity.....	49
2.6. Oleophobic metal matrix composites	50
2.7. Contact angle hysteresis on metal matrix composites.....	51

2.7.1.	Origins of contact angle hysteresis.....	56
2.7.2.	Modeling wetting/dewetting in multiphase systems	59
2.7.2.1.	CA in multiphase systems.....	60
2.7.2.2.	CA hysteresis in multiphase systems.....	61
2.7.3.	Experimental observation.....	63
2.7.4.	Contact angle hysteresis discussion.....	68
2.8.	Beyond Wenzel and Cassie-Baxter: second order effects.....	69
2.8.1.	Modeling of wetting for a surface with hierarchical roughness.....	73
2.8.2.	Experimental observation.....	77
2.8.2.1.	Sample preparation.....	77
2.8.2.2.	Sample characterization	79
2.8.3.	Discussion	81
2.9.	Conclusion	84
CHAPTER THREE.....		86
3.	CONCRETE	86
3.1.	Wetting of concrete	87
3.2.	Modeling of superhydrophobic concrete	91
3.2.1.	Contact angle measurement.....	95
3.2.2.	Contribution of hierarchical roughness.....	96
3.3.	Conclusion	98
CHAPTER FOUR.....		99
4.	Oleophobicity.....	99
4.1.	Oleophobic/philic surfaces and types of oleophobicity	99
4.1.1.	Modeling of underwater oleophobicity	103
4.1.1.1.	Two-phase interface of solid oil (Wenzel regime).....	103
4.1.1.2.	Three-phase interface of solid-oil-water (Cassie-Baxter regime).....	107
4.1.1.3.	Four-phase interface of solid-oil-water-air.....	109
4.1.1.4.	Arbitrary number of phases	111
4.2.	Wetting transitions.....	111
4.2.1.	Wetting transitions as a phase transition.....	111
4.2.2.	Experimental study	114
4.2.3.	Mechanisms of wetting transitions	118
4.2.4.	Effect of surface topography on wetting transitions.....	121
4.2.5.	Wetting transitions discussion.....	126
4.3.	Conclusion	128

CHAPTER FIVE.....	130
5. ICEPHOBICITY.....	130
5.1. Literature survey.....	131
5.2. Forces and interaction analysis.....	134
5.2.1. Water droplet.....	134
5.2.2. Ice.....	139
5.3. Experimental study.....	140
5.3.1. Adhesion strength of ice.....	140
5.3.2. Concrete-ice adhesion strength.....	144
5.3.3. Water impact test.....	147
5.4. Icephobicity of superhydrophobic surfaces.....	148
5.5. Discussion.....	151
5.6. Conclusion.....	154
CHAPTER SIX.....	156
6. CONCLUSION.....	156
APPENDIX.....	160
Materials and experimental procedure.....	160
Preparation of hydrophobic coatings.....	163
Sample tile preparation.....	164
Results and discussion.....	166
Characterization of coatings.....	166
REFERENCES.....	169
CURRICULUM VITAE.....	184

List of Figures

Figure 1. Montage of some examples from nature (National geographic): (a) lotus leaf, (b) moth eye, (c) water strider, (d) sand skink, (e) shark skin, (f) gecko (http://www.nationalgeographic.com).....	3
Figure 2. Schematic of the experimental flow channel connected with a differential manometer. The H, W and L are the thickness, width and the length of the channel, respectively (Jung and Bhushan, 2010a).....	8
Figure 3. (a) SEM micrograph of shark skin replica. (b) Optical microscope images of the rib patterned surface fabricated as a model of artificial shark skin surface (Jung and Bhushan, 2010a).....	8
Figure 4. SEM micrographs of Lotus (<i>Nelumbo nucifera</i>) leaf surface, and image of water droplet sitting on the Lotus leaf (Bhushan et al., 2009b).....	11
Figure 5. Image of antifogging properties of mosquito compound eyes (Gao et al., 2007).	12
Figure 6. (a) SEM image showing hierarchical structure of duck feather. (b) SEM image of tomenta of a duck feather (Eadie and Ghosh, 2011).....	13
Figure 7. Schematic of healing mechanism in hollow tube approach (Wu et al., 2008)...	15
Figure 8. Schematic of healing mechanism in microencapsulation approach (Wu et al., 2008).....	16
Figure 9. A water-vapor surface coming to the solid surface at the contact angle of θ ...	20
Figure 10. Schematics of configurations described by the (a) Wenzel equation for the homogeneous interface, (b) Cassie-Baxter equation for the composite interface with air pockets, and (c) the Cassie equation for the homogeneous interface (Nosonovsky and Bhushan, 2008d).....	22
Figure 11. Contact angle for rough surface (θ) as a function of the roughness factor (R_f) for various contact angles of the smooth surface (θ_0) (Nosonovsky and Bhushan, 2005).	22
Figure 12. (a) Schematic of formation of a composite solid-liquid-air interface for rough surface, (b) contact angle for rough surface (θ) as a function of the roughness factor (R_f) for various f_{LA} values on the hydrophilic surface and the hydrophobic surface, and (c) f_{LA} requirement for a hydrophilic surface to be hydrophobic as a function of the roughness factor (R_f) and θ_0 (Jung and Bhushan, 2006).....	25
Figure 13. Comparison between conventional monolithic materials and composite materials (Deutsch, 1978).....	31
Figure 14. Schematic of different types of matrices.....	33
Figure 15. The water contact angle as a function of graphite reinforcement volume fraction for different values of f_{SLm}	42
Figure 16. The variation of the reinforcement volume fraction, f_r , versus f_{SLm}	42
Figure 17. SEM images of polished samples.....	44

Figure 18. Images of water droplet on non-etched samples.	45
Figure 19. Images of water droplet on etched samples.	46
Figure 20. The schematic of surface before and after etching for a matrix reinforced with particles.	47
Figure 21. Advancing and receding contact angles for a droplet on a tilted solid surface.	51
Figure 22. Schematic of nine wetting regimes for a rough surface characterized by no penetration, partial penetration, and complete penetration of water into microroughness, nanoroughness and both micro and nanoroughnes (Bhushan and Nosonovsky, 2010).	56
Figure 23. Schematic of advancing and receding contact angles (a) due to surface slope and (b) heterogeneity (c) water column suspended in a capillary due to CA hysteresis.	57
Figure 24. Schematic of a four-phase interface showing both water and vapor trapped at the interface between the solid and oil.	61
Figure 25. CA hysteresis for different values of the constant c . (a) Two-phase interface, (b) Three-phase interface, (c) Four-phase interface, (d) Comparison of the CA hysteresis of two-, three- and four-phase interfaces.	63
Figure 26. Advancing and receding CAs of water droplet on gray iron in air for the three samples with roughness. The angle between the surface and horizontal line is 0, 9, 22 and 90 degrees from left to right, respectively. (a) $R_a=0.1 \mu\text{m}$ (b) $R_a =0.2 \mu\text{m}$ (c) $R_a =0..$	65
Figure 27. Advancing and receding CAs of air bubble on gray iron submerged in water for the three samples. (a) $R_a=0.1\mu\text{m}$. The angle between the surface and horizontal line is 0, 9, and 22 degrees from left to right, respectively. (b) $R_a=0.2 \mu\text{m}$. The angle between the surface and horizontal line is 0, 9, and 27 degrees from left to right, respectively.	66
Figure 28. Advancing and receding CAs of oil droplet on gray iron submerged in water for three samples. The angle between the surface and horizontal line is 0, 25, and 90 degrees from left to right, respectively. (a) $R_a=0.1 \mu\text{m}$ (b) $R_a=0.2 \mu\text{m}$ (c) $R_a=0.3 \mu\text{m}$	67
Figure 29. (a) Thin film in equilibrium with the bulk liquid of the droplet (b) Disjoining pressure versus the film thickness, h , (c) Energy profile of the liquid film.	70
Figure 30. Multiscale roughness.	73
Figure 31. Wetting regimes.	74
Figure 32. CA versus liquid film thickness, h	76
Figure 33. SEM image of the samples polished with the sand paper grit size 600 (a) aluminum (b) stainless steel.	78
Figure 34. SEM image of etched samples (a) aluminum (b) stainless steel.	79
Figure 35. Water CA profile of (a) aluminum and (b) stainless steel samples before processing (c) aluminum and (d) stainless steel after grinding (grit size 400) (e) aluminum and (f) stainless steel after etching (120 seconds).	80

Figure 36. CA versus average roughness, R_a , (a) Aluminum samples (b) Stainless Steel samples.	80
Figure 37. (a) 1D Roughness profile (b) 3D roughness profile of etched aluminum (c) 3D roughness profile of abraded aluminum.....	82
Figure 38. The hydrophilic ($0^\circ \leq \theta < 90^\circ$), hydrophobic ($90^\circ \leq \theta$), “over-hydrophobic” ($120^\circ \leq \theta < 150^\circ$) and superhydrophobic ($150^\circ \leq \theta \leq 180^\circ$) surfaces, where θ is the CA (Flores et al., 2013).....	88
Figure 39. Schematics of water droplets on the rough surfaces: (a) Wenzel (b) Cassie-Baxter (Flores et al., 2013).	89
Figure 40. Schematics of the proposed hydrophobic concrete concept (Flores et al., 2013).....	90
Figure 41. (a) Aggregate fractional area, f_a versus the cementitious matrix fractional area, f_{cw} (b) CA versus aggregate fractional area, f_a for various values of fractional the cementitious matrix -water contact area, f_{cw} (Flores et al., 2013).....	92
Figure 42. (a) Schematics of the aggregate patterns at the interface. (b, c, d, e) CA versus distance between the aggregates, L , for $\theta_a = \theta_c \approx 95^\circ$ and (b) $D=500 \mu\text{m}$, $R_{fc}=1$ (c) $D=500 \mu\text{m}$, $R_{fc}=3$ (d) $D=1000 \mu\text{m}$, $R_{fc}=1$ (e) $D=1000 \mu\text{m}$, $R_{fc}=3$ (Flores et al., 2013).....	93
Figure 43. The effect of the droplet size of the emulsion on the irregularity of the coatings (Flores et al., 2013).....	95
Figure 44. The contact angle of specimens with single (Mk)- and double (DMk)- coatings (Flores et al., 2013).....	96
Figure 45. The profile of surfaces of mortar specimens: (a) Collapsed cellular structure, (b) particle coating, (c) bubbles on the surface (Flores et al., 2013).	97
Figure 46. CA versus distance of the aggregates, L , for $D=500 \mu\text{m}$, $R_{fc}=1$ and $\theta_a = \theta_c \approx 95^\circ$ (a) $n=30$ and $d=2 \mu\text{m}$ (Mk1) (b) $n=100$ and $d=5 \mu\text{m}$ (Mk2) (c) $n=20$ and $d=10 \mu\text{m}$ (Mk3) (Flores et al., 2013).....	97
Figure 47. Water droplet on a microstructured surface forming (a) Wenzel (two-phase solid-water) (b) Cassie-Baxter (three-phase solid-water-air) (d) oil droplet (immersed in water) on four-phase solid-oil-water-air interface (d) slippery lubricant-infused porous.....	102
Figure 48. Wetting of a microstructured surface in the homogeneous (Wenzel, solid-oil) regime.....	104
Figure 49. Schematics showing CAs and interfacial energies (a) in four different systems (solid-water-air, solid-oil-air, solid-oil-water, and oil-water-air) (b) together form a tetrahedron.	105
Figure 50. Wetting of a microstructured surface in the composite (Cassie-Baxter, solid-oil-water) regime.....	107
Figure 51. Oleophobic and oleophilic regimes for the three-phase rough solid-oil-water interface for $R_f = 5$	109

Figure 52. Oleophobic and oleophilic regimes for the four-phase rough solid-oil-water interface for $R_f = 5$.	110
Figure 53. Interfacial energy as a function of order parameters.	112
Figure 54. Experimental observation of the Wenzel and Cassie-Baxter wetting regimes in a solid-oil-water system for two materials (Al base alloy and Al-graphite composite) with different roughness (a) non-etched samples (b) samples etched for 10 seconds (c) samples etched for 20 seconds.	116
Figure 55. Cassie-Wenzel transition showing the oil-air interface parallel to the pillar base penetrating into the crevices between the pillars.	117
Figure 56. Contact angles in the Wenzel, stable and metastable Cassie-Baxter regimes as a function of surface roughness.	117
Figure 57. A typical net free energy dependency on the position of the interface, h .	118
Figure 58. Schematic of a four-phase interface.	119
Figure 59. The contact angle versus the spacing factor, S_p^2 for Al and Al-graphite composite.	121
Figure 60. Schematic of underwater interface (a) Wenzel state. (b) CB state.	123
Figure 61. SEM of samples and underwater oil droplet pics. (a) Brass 360 abraded with SiC paper (336 μm particle size), (b) Brass 360 abraded with SiC paper (201 μm particle size), (c) Brass 360 abraded with SiC paper (82 μm particle size), (d) Brass 360 abraded with SiC paper (46 μm particle size), (e) Brass 360 abraded with SiC paper (26 μm particle size), (f) Brass 360 abraded with SiC paper (15 μm particle size), (g) Brass 360 abraded with soft cloth (1 μm particle size).	124
Figure 62. Oil CA, Water CA and underwater oil CA of samples versus average roughness, R_a .	125
Figure 63. CA of oil with a rough Brass surface under water versus surface roughness, R_a , for W ($f_{so}=1$), CB with a constant solid-oil contact area fraction ($f_{so}=0.15$) and CB with solid-oil contact area fraction dependent on roughness.	128
Figure 64. Schematic of the water droplet and ice on the surface (a) Side view of the water droplet placed on the surface with the tilt angle ψ (b) Top view of a water droplet placed on the surface (c) Side view of the water droplet placed on the tilted surface and forces and the moment applied to it (d) Side view of the ice formed on the vertical surface, forces applied to it. Ice detachment occurs as the Mode I (crack opening) and Mode II (shear) fracture (Hejazi et al., 2013).	135
Figure 65. Force and moment versus A . (a) F_x versus the constant A for various values of ξ (b) F_z versus the constant A for various values of ξ (c) The moment versus the constant A for various values of ξ and $\gamma=0.072 \text{ Jm}^{-2}$ for $\theta_0=60^\circ$, $\psi=90^\circ$, $P_L=144 \text{ Pa}$ and $r=2$, $d_1=1$, $d_2=1\text{mm}$ (Hejazi et al., 2013).	139
Figure 66. Schematic of the apparatus (a) PASCO stress/strain apparatus (b) Horizontal force applied to the ice column (c) Force versus time of deformation. Color lines show the applied forces to the ice on various substrates versus time (Hejazi et al., 2013).	141

Figure 67. Contact angle and contact angle hysteresis. Right axis shows the data corresponding to CA hysteresis (Red dots) and left axis shows the data related to advancing and receding CA (Black squares and triangles)	144
Figure 68. Coated and non-coated ice-concrete samples.....	145
Figure 69. Schematic of the compression test set-up (b) compression test set-up (c) broken ice on non-coated concrete (d) broken ice on coated concrete.....	146
Figure 70. Force versus displacement for coated and non-coated concrete samples.....	147
Figure 71. The water droplet jumped off a tilted glass substrate coated by soot at -20°C (Hejazi et al., 2013).....	148
Figure 72. Parallelism of hydrophobic interaction and ice formation (a) The attractive force between hydrophobic molecules (hydrocarbons) is a result of Gibbs energy $\Delta G = \Delta H - T\Delta S$ minimization due to entropy increase ΔS in water molecular network (hydrocarbon-water- hydrocarbon system) prevailing over enthalpy ΔH (b) The synchronization of branch growth during formation of a snow crystal due to ΔS prevailing over ΔH (ice-saturated vapor-ice system) (Hejazi et al., 2013).....	154
Figure 73. SEM images of metakaolin (left) and portland cement (right), (2000x magnification) (Flores et al., 2013).....	161
Figure 74. X-ray diffraction of MK (top) and PC (bottom) (Flores et al., 2013).....	162
Figure 75. The explanation of simple, core and shell concepts used to design PMHS emulsions (Flores et al., 2013).....	164
Figure 76. The procedure for preparation of PHMS emulsions (Flores et al., 2013).....	164
Figure 77. The surface of mortar tiles observed by SEM at 500x (left) and 2000x (right) magnifications (Flores et al., 2013).....	165
Figure 78. Emulsion images taken by optical microscope at 1000x magnification for: (a) Mk1; (b) Mk2; and (c) Mk3 (Flores et al., 2013).....	166
Figure 79. SEM images of superhydrophobic coatings at 500x magnification for: a) Mk1; b) Mk2; c) Mk3; and d) Mk2 at 2000x magnification (Flores et al., 2013).....	168

List of Tables

Table 1. Chemical composition of the samples.....	43
Table 2. Measured and calculated surface roughness and contact angles.....	46
Table 3. Effect of wear on contact angle.....	50
Table 4. Advancing and receding contact angles and hysteresis	64
Table 5. Forces contributing to the droplet/bubble adhesion to solid.	69
Table 6. Oleophobic and oleophilic interfaces.....	106
Table 7. Contact angle of oil on submerged surface.....	115
Table 8. Water CAs of the samples and shear strength of the ice.....	142
Table 9. The comparison of the hydrophobicity and icephobicity.....	152
Table 10. Test results of portland cement Type I compared to ASTM C150 requirements.	162

CHAPTER ONE

1. INTRODUCTION

The term "biomimetics" is derived from the Greek word "biomimesis" which means mimicking the nature. The word was coined by the American biophysicist and polymath Otto Schmitt during the 1950s. He was working on his doctoral research when he developed the Schmitt trigger by studying the nerves in squid, attempting to engineer a device that mimicked the electrical action of a nerve. The other word used is "bionic" which was coined by Jack E. Steele in 1958, possibly originating from the technical term *bion* (from Ancient Greek), meaning "unit of life" and the suffix *-ic*, meaning "like" or "in the manner of". Other words used include biomimicry, biognosis and bio-inspiration.

Biomimetics is the application of biological methods and systems found in nature to the study and design of engineering systems and modern technology. It is a highly interdisciplinary field and crosses the boundaries between academic disciplines such as physics, chemistry, biology and material science.

The term biomimetic found its way into Webster`s dictionary by 1974 when it was used by Schmitt to title one of his papers. It is used to study of the biological mechanisms and processes to fabricate similar products by artificial mechanisms which mimic natural ones` (Bhushan, 2009). The understanding of the processes and the functions found in the nature can help us to imitate and duplicate micro and nanomaterials and devices (Bhushan, 2009). This concept may be applied to various areas of engineering, e.g., artificial intelligence and neural networks in information technology are inspired by the desire to mimic human brain. The existence of biocells and deoxyribonucleic (DNA) serves as a source of inspiration for nanotechnologists

who hope to one day build self-assembled molecular-scale devices. In the field of biomimetic materials, there is also a whole area of bio-inspired ceramics based on sea shells and other biomimetic materials.

There are a large number of objects, including bacteria, animals and plants with properties of commercial interest. Many people have presented a number of ideas in the field of biomimetic surfaces (Barthlott and Neinhuis, 1997; Bar-Cohen, 2006; Gorb, 2005; Rechenberg and Kheyri, 2007) including the lotus-leaf surface, which has self-cleaning property; shark skin, which can suppress turbulence while moving underwater; the gecko foot, which has very high adhesion with the surface; the moth eye, which does not reflect light; the water strider leg, which stays dry atop the water pool; the sand skink, which decreases the friction using nanothresholds and the darkling beetle, which collects dew using hydrophilic microspots. Most of these objects have a feature in common which is hierarchical roughness with rough details ranging from nanometers to millimeters (Nosonovsky and Bhushan, 2008a). A montage of some example found in nature is shown in Figure 1.

As mentioned, some leaves such as *Nelumbo nucifera* (Lotus), can repel water due to its hierarchical roughness as well as a hydrophobic wax coating (Barthlott and Neinhuis, 1997). This makes them to be known as superhydrophobic and self-cleaning objects. Water droplets on these surfaces easily sit on the top of the protrusions of nanostructures because air bubbles fill in the crevices of the structure under the droplet. Therefore, these leaves apparently show superhydrophobic property (Figure 1a).

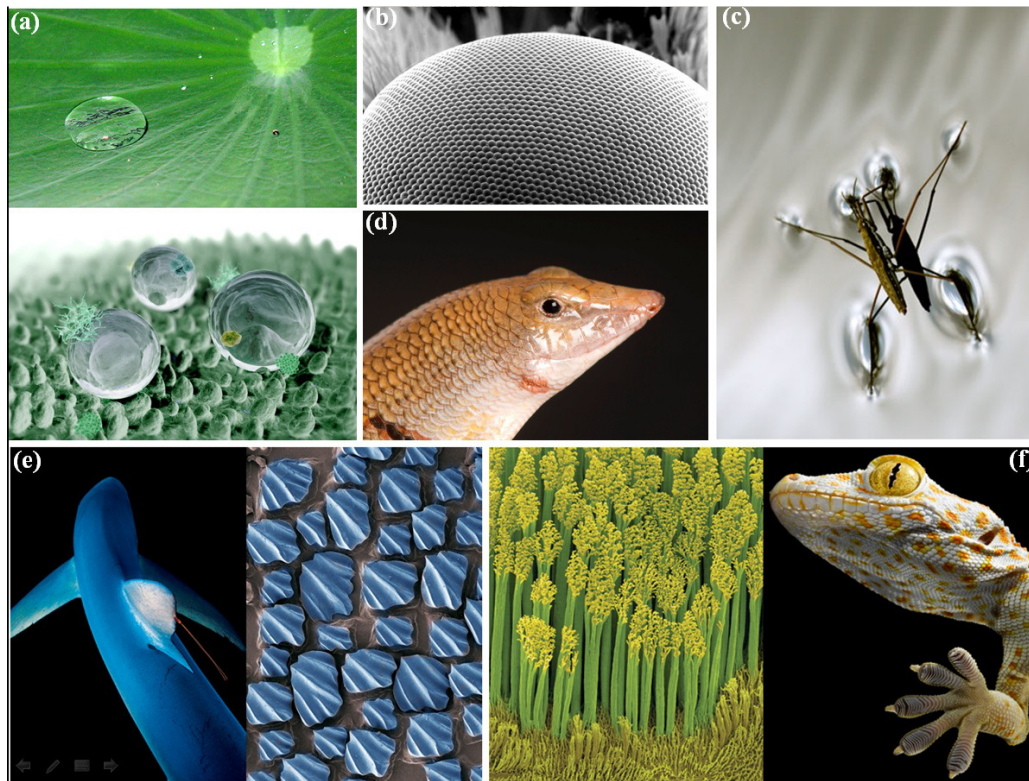


Figure 1. Montage of some examples from nature (National geographic): (a) lotus leaf, (b) moth eye, (c) water strider, (d) sand skin, (e) shark skin, (f) gecko (<http://www.nationalgeographic.com>).

The eyes of moths consist of hundreds of hexagonal nanoscopic pillars. These nanopillars (200 nm in diameter and height) result in a very low reflectance for visible light and make the eyes of moth nearly anti-reflective to visible light in any direction (Figure 1b) (Genzer and Efimenko, 2006; Mueller, 2008).

Water striders (Pond skaters) can stand and walk upon a water surface without getting wet (Figure 1c). It can skate on water surface even under the impact of rain droplets with a size greater than the pond skater's size and the rain does not make it immerse in the water. Gao and Jiang (2004) showed that the water strider's legs, are covered by a large number of oriented tiny hairs with fine nano grooves which make a special hierarchical structure. These hairs (microsetae) as well as a cuticle wax cover

on them make the legs surface superhydrophobic and resistant to water so that the strider can stand upon water surface.

Sand skink is a lizard that lives in desert (Figure 1d). Due to very low friction and abrasion properties of skink`s scales, it can virtually dive and swim beneath the surface of loose sand. This skink specie`s scale are covered by “nanothresholds”, long ridges with submicron height and distance of 10 μm or less. Rechenberg and El Kheyri (2007), who brought attention to the desert sand skink (*Scincus scincus*) and what they called the “sandfish-effect“, proposed the electrostatic charge created by submicron sized thresholds on the scale plays a role in friction reduction by creating a repulsive force between the scale and sand grains (Nosonovsky and Bhushan, 2008a).

Shark skin is covered by special types of tooth-like scales called dermal denticles (little skin teeth) that form small V-shaped bumps, ribbed with longitudinal grooves which are parallel to the local flow direction of the water (Figure 1e). These groove scales and rough skin surface reduce friction and the formation of vortices present on smooth surface which makes sharks very quick and efficient swimmers (Bechert et al., 2000). The control of the streamwise vortices in the turbulent flow can yield a significant drag reduction. Wainwright et al. (1978) also found that the internal pressure of the shark increases more than ten-fold from slow to fast swimming. This pressure increase causes the shark`s skin to deform faster (Ball, 1999; Itoh et al., 2006; Polidori et al., 2006). Several commercial products such as boats, aircrafts, swimming suits and so on have used shark-skin-effect (Nosonovsky and Bhushan, 2008a).

Using micro or nano setae, animal can cling and crawl on a wide range of surfaces. The gecko or Gekko gecko is a lizard which has the most advanced ability for attachment to the surfaces or detachment from surfaces. The gecko ability had

been observed even in ancient times; almost 2500 years ago by Aristotle (Bhushan, 2007a). However the reason for this phenomenon was not known until the late nineteenth century when the microscopic hairs covering the gecko's toe were observed. Then in the 1950s, after the advent of the scanning electron microscope (SEM), the hierarchical morphology of the gecko's toe was discovered.

This complex hierarchical structure consists of lamellae, setae, branches, and spatula (Autumn et al., 2000; Gao et al., 2005; Bhushan, 2007a). The area of the attachment pads on two feet of the gecko is approximately 220 mm^2 (Figure 1f). To produce the required vertical force (approximately 20 N) for clinging ability, there are approximately 3×10^6 setae on gecko's toes which allow it to climb vertical surfaces at speeds of over 1 m/s, with the capability to attach or detach their toes in milliseconds (Bhushan, 2007a).

1.1. Biomimetic surfaces

The term biomimetics signifies mimicking the nature to develop materials and devices of commercial interest by engineers. The main goal in the area of biomimetic materials is to explore a radically new approach for the design of bio-inspired artificial devices with high quality properties.

Many clever devices in nature are made by very simple materials such as keratin, silica, calcium carbonate and so on, which nature manipulates them into structures with unbelievable strength, persistence, complexity and toughness. For example the shell of an abalone is made by calcium carbonate same as soft chalk. However the abalone creates its shell like an armor which is approximately 3000 times harder than soft chalk. In fact it makes a staggered structure of nanoscale bricks as tough as Kevlar through an ingenious play of proteins and calcium carbonates. To

re-create an artificial material synthetically, understanding the micro/nanoscale structure of a similar living material's exceptional properties is vital.

The bio-inspired robot is potentially one of the most applicable samples of natural design. This robot could be employed in situations where people would be in hazard, or killed. For instance, consider a miniature robotic fly which is very small and quick with wings beating 150 times per second which can dive, soar or hover with fantastic agility. It is maneuverable enough to use in surveillance and rescue operations. Approximately 20 muscles are deployed by each fly's wing, and some of which only fire every fifth wing beat. For making this micromechanical insect, the key is not to copy the fly, but to understand the structures crucial of flying, while trying to design a simpler or even better model. However such robots are apparently expensive and laborious to build.

Spenko et al. (2008) tried to design a climber robot inspired from the gecko. People have wondered how the gecko manages its gravity to run up or down the tree even with the head downward. The gecko feet are dry and no sticky. The gecko has approximately 20 million spatula-tipped filaments per square millimeter on its toe pads. These filaments are so small and with the thickness of a hundred nanometers. To produce the robot's toe pads, he used urethane fabric with very small bristles which end in 30 micrometer points. They could hold a 500-gram robot on a vertical surface, it was not as adherent as gecko though. Spenko found the adhesion is only one side of the gecko ability to run up a vertical surface at one meter per second speed, and the other side is to unstick the feet easily and instantly from the surface. He did the slow-motion analysis of gecko movement on vertical surface as well as the painstaking anatomical study, to understand the attachment and detachment mechanisms of lizard's toes. He discovered that the toes attach only when dragged

downward and detach when the direction of pull is upward. He used a combination of metals, polymers and fabrics to create legs and feet of his robot as flexible and stiff as gecko's limbs. He made his robot with seven-segmented toes which attach and detach just like the gecko. He found that the gecko uses branching tendons to distribute its weight uniformly across the surface of its toes. Accordingly, he embedded a branching tendon made by polyester cloth to his robot's legs and feet to distribute its weight in the same way. Then the robot could walk up vertical surfaces of plastic, glass and ceramic tile. However, its toes did not have the dry adhesive and self-cleaning properties like gecko's toes and they were quickly clogged by dirt and dust. Although this gecko inspired robot does not have a real-world application so far, but it would play a lifesaving or humanitarian role in the offing.

Another biomimetics paradigm which is using as a household product is Velcro which was invented in 1948 by Swiss chemist George de Mestral. He got the idea by seeing the way that cockleburs clung to his dog's coat.

One of the other examples found in nature is the drag reduction in fluid flow and the shark skin can be a nice model from nature with this property. Drag reduction in fluid flow is of interest in micro/nanofluidics based biosensor applications (Bhushan, 2007b). In fact, minimizing the drag force in the solid-liquid interface yields to reduce pressure drop and volume loss in micro/nanochannels. The artificial surfaces from the shark skin have been created, and the influence of structure on drag reduction efficiency is discussed.

Jung and Bhushan, 2010a conducted experiments using air and water flows to measure pressure drop inside a rectangular channel (Figure 2).

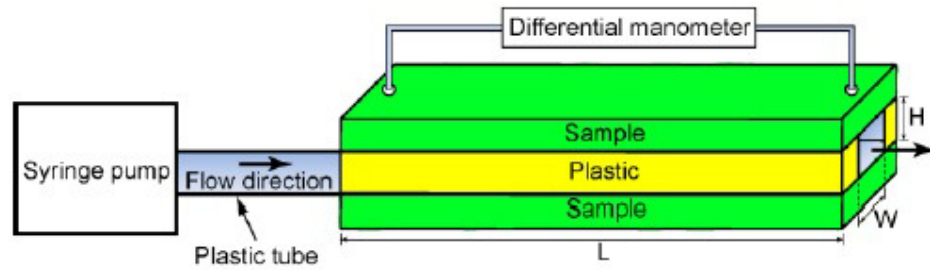


Figure 2. Schematic of the experimental flow channel connected with a differential manometer. The H, W and L are the thickness, width and the length of the channel, respectively (Jung and Bhushan, 2010a).

Mimicking the shark skin replica (Figure 3a), they fabricated rib patterned surfaces on a flat acrylic resin to observe the effect of artificial shark skin pattern on fluid drag reduction in the channel (Figure 3b).

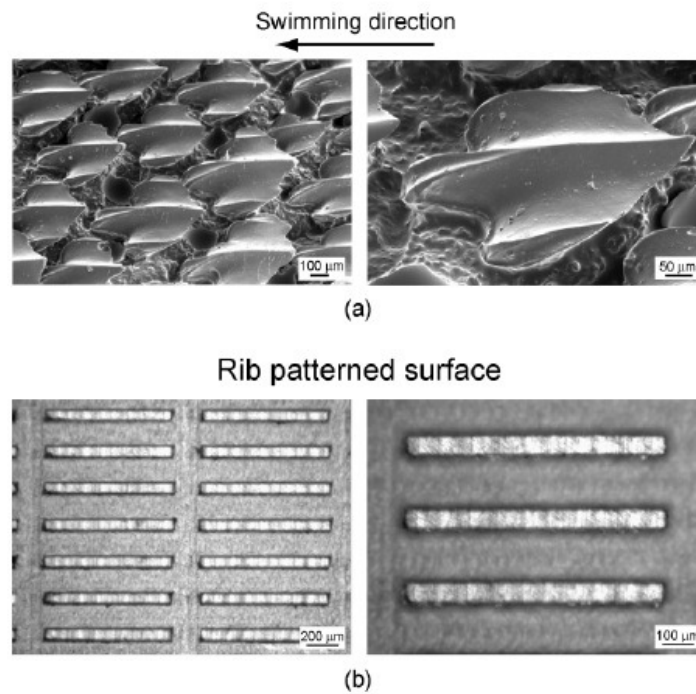


Figure 3. (a) SEM micrograph of shark skin replica. (b) Optical microscope images of the rib patterned surface fabricated as a model of artificial shark skin surface (Jung and Bhushan, 2010a).

Their results showed that the Reynolds number of water flow was 4200 which indicates that the flow is turbulent and the Reynolds number of air flow was between 200 and 4600 which indicates both laminar and turbulent flows. They showed that a reduction up to 30% in pressure drop can be obtained in turbulent flow by mimicking the shark skin replica pattern. The results showed that ribs are more benefit to produce drag reduction in turbulent flow rather than in laminar flow.

They found that the introduction of roughness increases the hydrophobicity of the surfaces responsible for reduction in drag or pressure drop. The highest reduction of pressure drop was obtained for the hierarchical structure with highest contact angle and lowest contact angle hysteresis. They believed that air pockets trapped inside the grooves result in pressure drop reduction by reducing the contact area between fluid and surface. Therefore they concluded that the superhydrophobicity can lead to drag reduction in fluid flow (Jung and Bhushan, 2010a).

These paradigms show that the gap with nature is gradually closing. Scientists and researchers are using technologies such as electron force microscopes, atomic force microscopes, X-ray microtomography, and high-speed computers to peer deeper into the micro/nanoscale secrets of the nature, and employing new advanced materials to mimic them more accurately than ever before. And even before biomimetics matures into a commercial industry, it has itself developed into a powerful new tool for understanding life.

1.1.1. Superhydrophobic materials in living nature

Superhydrophobic or highly hydrophobic (hydro/water+phobic/fearing) surfaces are surfaces which repel water and it is extremely difficult to wet their surfaces. There are a large number of biological surfaces which are known to be superhydrophobic and self-cleaning.

For a long time the hydrophobicity property of many plant leaves have been known. Since 1970s, scientists knew that the water repellency of the plant leaves is due to their microstructure. The outer cells which cover plant leaves are called epidermis cells. The epidermis cells themselves are covered by a composite membrane called cuticle which built up of a hydrophobic wax and a cutin network (Barthlott and Neinhuis, 1997; Koch et al., 2008a, 2009a). Koch et al., 2009c showed that waxes diffuse through the cuticle via a lipidic pathway. If this wax removes, the plants repair it by self-assembly.

Another important ability of the plant related to the hydrophobicity is keeping the leaves clean even after being immersed in dirty water, known as self-cleaning. The most famous plant with this ability is Lotus (*Nelumbo nucifera*). Therefore the phenomenon of self-cleaning and water repellency was called “Lotus effect”. The self-cleaning ability of the lotus leaf is for defense against the pathogens binding to the leaf surface.

Many researchers have studied the wetting and superhydrophobicity of lotus leaves (Neinhuis and Barthlott, 1997; Barthlott and Neinhuis, 1997; Wagner et al., 2003; Burton and Bhushan, 2006; Bhushan and Jung, 2006; Bhushan, 2009; Koch et al., 2008a, 2009a). Neinhuis and Barthlott, 1997 studied the water repellency of almost 200 plants and found the various types and shapes of wax crystals at the surface. Their SEM study revealed that the lotus leaf surface is covered by a lot of bumps called papillae (Figure 4). The papillae themselves are covered by a layer of epicuticular wax (Barthlott and Neinhuis, 1997; Koch et al., 2006a, 2008a, 2009a). The wax is intrinsic hydrophobic and the papillae magnify the water-repellency of the leaf. The bumpy surfaces of the leaf with a thin layer of wax showed water-repellency for shorter periods of time comparing to the surfaces with a thick layer of wax.

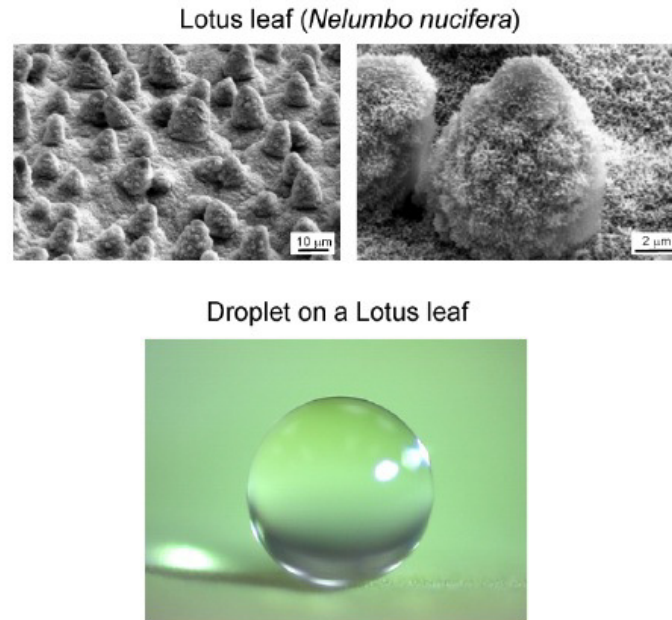


Figure 4. SEM micrographs of Lotus (*Nelumbo nucifera*) leaf surface, and image of water droplet sitting on the Lotus leaf (Bhushan et al., 2009b).

It was found the hierarchical structure of the lotus leaves is responsible for superhydrophobicity (Burton and Bhushan, 2006; Bhushan and Jung, 2006). The water droplets easily sit on the top of the nanostructures so that the air bubbles fill in the crevices of the structure beneath the droplets. Therefore the lotus leaves show significant superhydrophobicity.

Gao and Jiang, 2004 studied the wetting property of water strider's legs. Water striders (*Gerris remigis*) have considerable non-wetting legs that enable them to stand easily and move quickly on water. They believed that this feature can be due to a surface-tension effect caused by secreted wax layer on strider's legs. They showed that the main reason is the special hierarchical structure of the legs, which are covered by large numbers of oriented tiny hairs (microsetae) with fine nanogrooves, that is more important in inducing this water resistance.

Gao et al., 2007 studied the surface structure of mosquito (*Culex pipiens*) compound eyes (Figure 5). They showed the antifogging properties of mosquito eyes

result from their elaborate superhydrophobic surface structure, which consists of hexagonally non-close-packed nipples at the nanoscale and hexagonally close-packed hemispheres at the microscale. They used a soft-lithography approach to fabricate artificial compound eyes for exploring the effects of the hierarchical micro- and nanostructure on surface hydrophobicity.

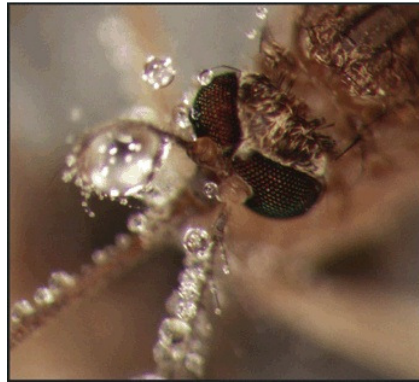


Figure 5. Image of antifogging properties of mosquito compound eyes (Gao et al., 2007).

Duck feathers and butterfly wings are the other examples of superhydrophobic surfaces (Bhushan, 2009). Liu et al., 2008 claimed that duck feathers exhibit highly ordered and hierarchical branched structures built around a micro-sized backbone. Branches of various sizes of a duck feather are made up of micro-sized tomenta (Figure 6a). These tomenta in turn have nanoscale undulates on the surface as shown in Figure 6b. Their surfaces have a corrugated structure with trapped air pockets inside grooves which prevent water from completely touching the surface. Therefore the duck feathers exhibit considerable superhydrophobicity.

Similar to the above examples, many others show noticeable superhydrophobic behavior such as taro leaf, rice leaf, and so on.

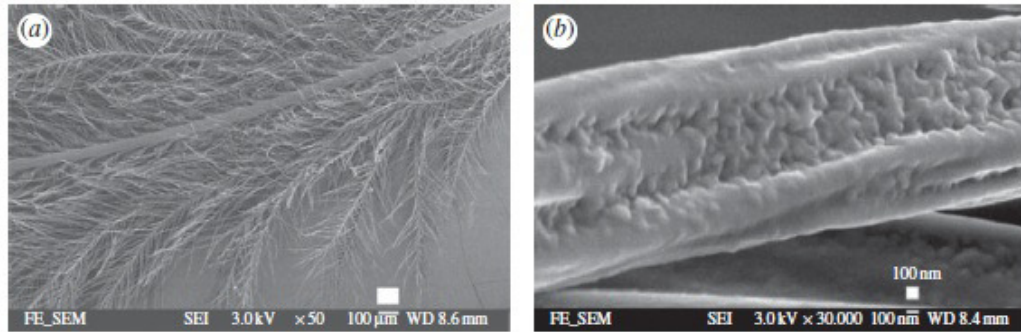


Figure 6. (a) SEM image showing hierarchical structure of duck feather. (b) SEM image of tomenta of a duck feather (Eadie and Ghosh, 2011).

1.1.2. Lotus effect and self-cleaning

The self-cleaning property of plant leaves is due to especially textured topography of the surface as well as the chemical constituents of the cuticle covering their surface (Barthlott and Neinhuis, 1997; Neinhuis and Barthlott, 1997; Wagner et al., 2003; Eadie and Ghosh, 2011). While self-cleaning property is present in many plant surfaces, the self-cleaning behavior of lotus leaves has drawn iconic interest. Water drops on lotus leaves readily roll upon the surface, picking up the dirt particles along the way, in a mechanism known as self-cleaning. The hierarchical micro/nano-sized structures are responsible for this behavior (Barthlott and Neinhuis, 1997; Neinhuis and Barthlott, 1998; Eadie and Ghosh, 2011). The first level of structures is micro-sized protrusions or bumps consisting of papillose epidermal cells. The second level of structure consists of nano-sized hair-like growths present on the outer surface of epidermal cells. The epicuticular wax layer with low surface energy on the surface magnifies the superhydrophobicity behavior. The air pockets trapped inside the crevices between papillae lead to a reduced contact area between the surface and a liquid drop or a dirt particle (Tuteja et al., 2007). The water droplets place only on the apex of the epidermal cells, and as a consequence, dirt particles can be collected by the liquid and carried away as the liquid droplet rolls upon the leaf (Eadie and Ghosh,

2011). This happens because the van der Waals forces present between the leaf surface and the dirt particles are much weaker than the strong capillary forces between the water droplet and the dirt (Koch et al., 2009b).

1.1.3. Self-lubrication and self-healing

Self-lubricating surfaces have the advantage of having permanent lubrication built in. Self-lubrication is characterized by the ability of the bearings to transfer microscopic amounts of material to the mating surface. Due to this transfer, a thin film that provides lubrication is created over the surface. The transfer process continues throughout the whole operational life of the device and reduces friction and wear.

Self-healing may refer to automatic, homeostatic processes of the body that are controlled by physiological mechanisms inherent in the organism. Inspiring this ability of the body, a class of smart materials that have the structurally incorporated ability to repair damage caused by mechanical usage over time are created. They have the ability to heal after being cut, scratched or wounded. When a crack initiates on a microscopic level of a material, it changes thermal, electrical, and acoustical properties, and eventually lead to failure of the material. Repairing the cracks by hand is difficult because it is usually hard to detect a crack. A material that can basically mend damage caused by normal usage could reduce production costs of a number of different industrial processes through longer part lifetime, reduction of inefficiency over time caused by degradation, as well as prevent costs incurred by material failure. In fact a material is called self-healing, if the healing process occurs without human intervention.

For example there are two well-known methods for making self-healing polymers. In the first method, called hollow tube approach, fragile glass capillaries or

fibers are embedded within a polymeric material (Figure 7). Some fibers are filled with a monomer whereas the others are filled by a hardening agent. When damage occurs in the material, the fibers also crack and the monomer as well as hardening agent are released into the crack, causing the crack to be healed.

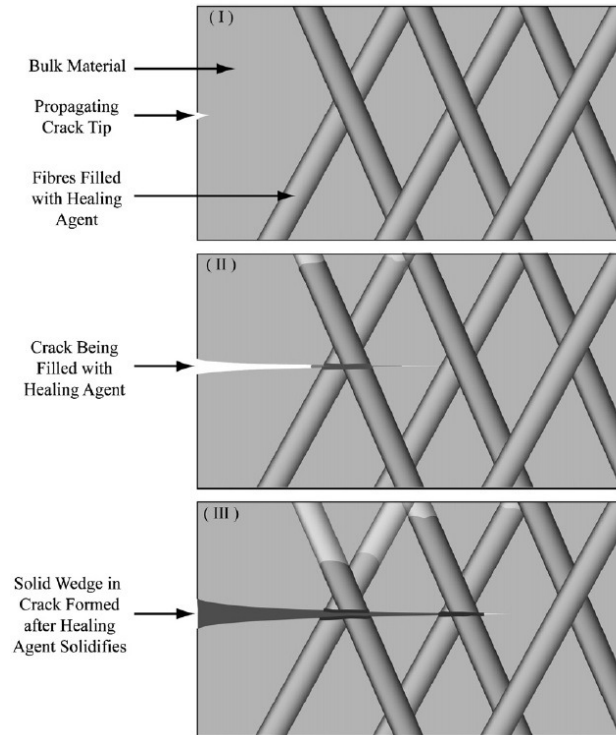


Figure 7. Schematic of healing mechanism in hollow tube approach (Wu et al., 2008).

The second method, called microencapsulation approach, is similar to the first method, except the monomer which is encapsulated and embedded within the polymer material. When the crack reaches the microcapsule, the capsule breaks and the monomer releases into the crack, where it can fill and repair the crack (Figure 8).

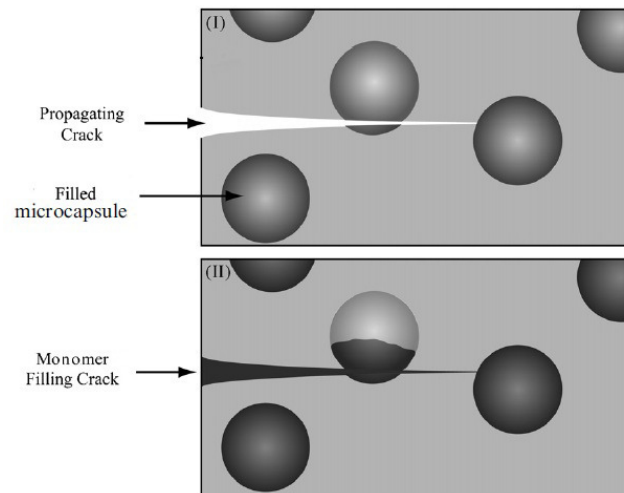


Figure 8. Schematic of healing mechanism in microencapsulation approach (Wu et al., 2008).

Rohatgi et al., 2010 demonstrated a self-healing aluminum-fly ash composite material. The healing is accomplished by including microscopic "balloons" in metals while they are still in liquid form. The balloons burst if the finished metal product is damaged, causing the materials inside to leak out and fill the cracked area. This material has been formed into prototype engine components for field research by use in diesel truck engines. They also could be used for quick repairs in machines ranging from automobiles to power plant turbines. Other types of self-healing material such as concrete, which can mend cracks with only water and carbon dioxide needed to trigger the process, has been introduced so far.

1.2. General principles of wetting

1.2.1. Interfacial energy and surface tension

The interfacial energies can be thought of either as energies per unit area needed to create an interface or as generalized forces per unit length acting along the interfaces at the triple line in equilibrium. Note that unlike conventional mechanical forces, the tension forces are not applied to the triple line (which is a geometrical line

and not a material object with mass) but rather constitute derivatives of the interfacial energies per the advancement distance of the triple line. These forces reflect the tendency of the system to reduce its energy (and increase entropy). The high energy of an interface causes wetting of the solid surface and spreading of liquid on it while low energy produces nonwetting interfaces.

The molecules sitting at a free surface of materials have less binding with adjacent molecules than the molecules in the bulk, so they have potential to make new bindings. Materials with higher potential have higher wetting ability.

In other word, the atoms or molecules at the surface of the liquids or solids can be treated as a relatively thin layer, different than those of the bulk, because the surface atoms or molecules have fewer bonds with neighboring atoms, and therefore, they have higher energy than similar atoms in the interior. This energy difference is attributed to the surface tension or free surface energy. This surface energy, γ , is equal to the required work to create a unit area of the surface at a constant pressure and temperature (Jung and Bhushan, 2009a). The concept of interfacial free energy was introduced by J. W. Gibbs in the 1870s. Although the surface tension (measured in Nm^{-1}) and interfacial energy (measured in Jm^{-2}) are often assumed to be identical, they are not exactly the same. The surface tension or, more exactly, the surface stress is the reversible work per unit area needed to elastically stretch a pre-existing surface.

The surface stress tensor is defined as

$$f_{ij} = \gamma\delta_{ij} + \partial\gamma/\partial\varepsilon_{ij} \quad (1.1)$$

where ε_{ij} is the elastic strain tensor and δ_{ij} is the Kronecker delta. For a symmetric surface, the diagonal components of the surface stress can be calculated as

$$f = \gamma + \partial\gamma/\partial\varepsilon \quad (1.2)$$

For liquids, the interfacial free energy does not change when the surface is stretched, however, for solids $\partial\gamma/\partial\varepsilon$ is not zero because the surface atomic structure of a solid are modified in elastic deformation (Cammarata, 1994).

1.2.2. Polar and non-polar substances and intermolecular forces

The arrangement or geometry of the atoms in some molecules is such that one end of the molecule has a positive electrical charge and the other side has a negative charge. If this is the case, the molecule is called a polar molecule, meaning that it has electrical poles. Otherwise, it is called a non-polar molecule. Whether molecules are polar or non-polar determines if they will mix to form a solution or that they do not mix well together. Note that solid-water and solid-oil adhesion is quite different in its physical nature. Oil is a non-polar liquid and as Bormashenko (2010) showed recently, the main contributor to the surface tension is the London dispersion force. However, for water the situation is different since it has polar molecules capable of forming hydrogen bonds. For water in contact with air or with a non-polar solid or liquid, the Gibbs free surface energy $\Delta G = \Delta H - T\Delta S$ is a consequence of missing hydrogen bonds (yielding excess enthalpy ΔH) and the entropic “hydrophobic effect” (excess entropy ΔS times temperature T) due to the reorientation of the network of hydrogen bonds. The entropic effect is several times stronger than the enthalpic one leading to the anomalously high surface tension of water $\gamma_{LV} = 72$ mN/m (Israelachvili, 2011). The study of water droplets in air versus air bubbles in water and versus oil bubbles in water allowed us to separate these effects. For a water droplet on a solid surface in air, missing hydrogen bonds and the reorientation of the network of hydrogen bonds contribute to the surface tension. The interactions at the solid-water interface are due to the London dispersion forces. For an air bubble the latter component is weak or absent, unlike in the case of an oil bubble.

1.3.Contact angle and superhydrophobicity

The primary parameter that characterizes wetting is the static contact angle, which is defined as the angle that a liquid makes with a solid. The contact angle depends on several factors, such as surface energy, surface roughness, and its cleanliness (Adamson, 1990; Israelachvili, 1992; Bhushan, 1999, 2002, 2008; Nosonovsky and Bhushan, 2008a). If the liquid wets the surface (referred to as wetting liquid or hydrophilic surface), the value of the static contact angle is between 0 and 90°, whereas if the liquid does not wet the surface (referred to as a non-wetting liquid or hydrophobic surface), the value of the contact angle is between 90° and 180°.

Contact angle is normally measured using a contact angle goniometer. The contact angle is not limited to a liquid/vapour interface; it is equally applicable to the interface of two liquids. Adhesion is a general term for several types of attractive forces that act between solid surfaces, including the van der Waals force, electrostatic force, chemical bonding and the capillary force, owing to the condensation of water at the surface. The effect of adhesion (which is often unfavorable) as a relatively short-range force is significant for micro or nanosystems that have contacting surfaces. The adhesion force strongly affects friction, mechanical contact and tribological performance of such system surfaces, for example can lead to 'stiction' which is a combination of adhesion and static friction (Bhushan1996, 2008). The stiction makes microelectromechanical switches and actuators being in ineffective operating and functioning. It is therefore desirable to produce non-adhesive surfaces.

1.3.1. Smooth surface

When a liquid droplet or air bubble meet a solid surface, the appeared angle between the droplet or bubble and the solid surface is called contact angle. The equilibrium contact angle is specific for any given system and is determined by the interactions across the three interfaces. Most often the concept is illustrated with a small liquid droplet resting on a smooth horizontal solid surface. The shape of the droplet is determined by the Young-Laplace equation, with the contact angle playing the role of a boundary condition.

When a liquid droplet or air bubble comes in contact with a smooth solid surface under the angle θ (Figure 9), the net energy change for propagation of the liquid front for a small distance dx is equal to $(\gamma_{SL} - \gamma_{SV} + \gamma_{LV} \cos\theta)dx$. Thus, for the liquid front being at equilibrium, the Young equation should be satisfied (Rowlinson and Widom, 1982), and the contact angle is given by

$$\cos\theta = \frac{\gamma_{SV} - \gamma_{SL}}{\gamma_{LV}} \quad (1.3)$$

where γ_{SL} , γ_{SV} and γ_{LV} are solid-liquid, solid-vapor and liquid-vapor interfacial energies, respectively.

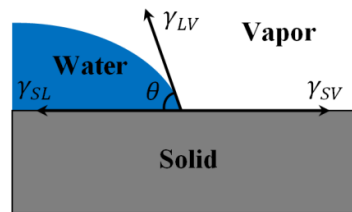


Figure 9. A water-vapor surface coming to the solid surface at the contact angle of θ .

From equation 1.3, it is obvious that three situations are likely. If $(\gamma_{SV} - \gamma_{SL})/\gamma_{LV} > 1$, the surface is completely wetted with the liquid fully absorbed by the solid surface ($\theta=0$), if $(\gamma_{SV} - \gamma_{SL})/\gamma_{LV} < -1$, the liquid is completely repelled by the

solid surface ($\theta=180^\circ$), and the last situation is when $-1 < (\gamma_{SV} - \gamma_{SL})/\gamma_{LV} < 1$ in which $0 < \theta < 180^\circ$.

1.3.2. Wenzel model

In this section, we investigate the equation that govern the contact angle of liquid with a rough surface. Consider a water droplet on a rough surface with a homogeneous interface. Comparing to smooth surface, the interface area for a rough surface is increased. Using the surface force balance and empirical considerations, the contact angle of a water droplet upon a rough solid surface, θ , is related to that upon a smooth surface, θ_0 , for a homogeneous interface (Figure 10), through the non-dimensional surface roughness factor, $R_f > 1$, equal to the ratio of the surface area, A_{SL} , to its flat projected area, A_F (Wenzel, 1936)

$$\cos \theta = \frac{dA_{LA}}{dA_F} = \frac{dA_{SL}}{dA_F} \frac{dA_{LA}}{dA_{SL}} = R_f \cos \theta_0 \quad (1.4)$$

$$R_f = \frac{A_{SL}}{A_F} \quad (1.5)$$

This is called the Wenzel equation. Figure 11 shows the dependence of the contact angle on the roughness factor for different values of θ_0 . The Wenzel model predicts that a hydrophobic surface ($\theta_0 > 90^\circ$) becomes more hydrophobic with an increase in R_f , while a hydrophilic surface ($\theta_0 < 90^\circ$) becomes more hydrophilic with an increase in R_f (Nosonovsky and Bhushan, 2005; Jung and Bhushan, 2006). The size and shape of the asperities can be optimized for a desired roughness factor.

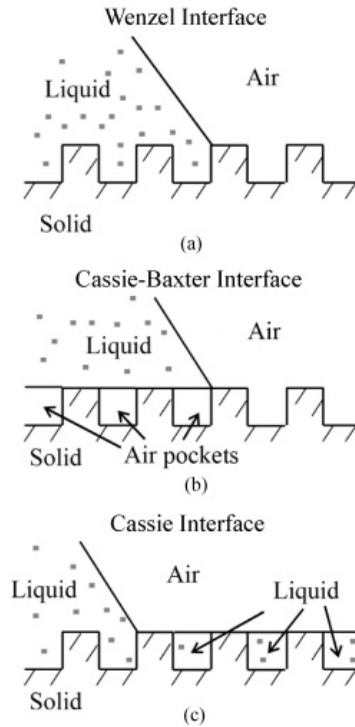


Figure 10. Schematics of configurations described by the (a) Wenzel equation for the homogeneous interface, (b) Cassie-Baxter equation for the composite interface with air pockets, and (c) the Cassie equation for the homogeneous interface (Nosonovsky and Bhushan, 2008d).

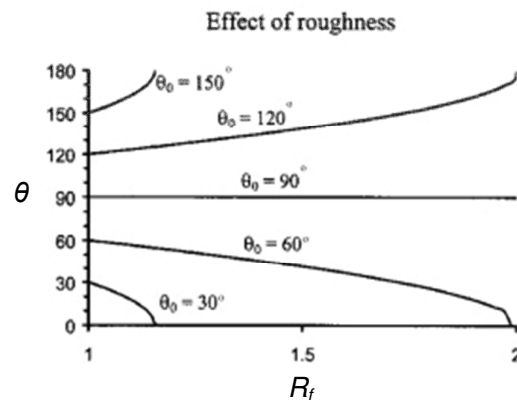


Figure 11. Contact angle for rough surface (θ) as a function of the roughness factor (R_f) for various contact angles of the smooth surface (θ_0) (Nosonovsky and Bhushan, 2005).

1.3.3. Cassie-Baxter model

For a surface composed of two fractions, one with the fractional area f_1 and the contact angle θ_1 and the other with f_2 and θ_2 , respectively (so that $f_1 + f_2 = 1$), the contact angle for the heterogeneous interface is given by the Cassie equation (Cassie and Baxter, 1944)

$$\cos \theta = f_1 \cos \theta_1 + f_2 \cos \theta_2 \quad (1.6)$$

For the case of a composite interface (Figure 10b), consisting of a solid-liquid fraction ($f_1 = f_{SL}, \theta_1 = \theta_0$) and liquid-air fraction ($f_2 = f_{LA} = 1 - f_{SL}, \cos \theta_2 = -1$), combining equations (1.5) and (1.6) yields the Cassie-Baxter equation (Cassie and Baxter, 1944)

$$\cos \theta = R_f f_{SL} \cos \theta_0 - 1 + f_{SL} = R_f \cos \theta_0 - f_{LA} (R_f \cos \theta_0 + 1) \quad (1.7)$$

The opposite limiting case of $\cos \theta_2 = 1$ ($\theta_2 = 0^\circ$ corresponds to the water-on-water contact) yields the Cassie equation (Nosonovsky and Bhushan, 2008a,d)

$$\cos \theta = 1 + f_{SL} (\cos \theta_0 - 1) \quad (1.8)$$

Equation (1.8) is used sometimes for the homogeneous interface instead of equation (1.4), if the rough surface is covered by holes filled with water (de Gennes et al., 2004) (Figure 10c).

Two situations in wetting of a rough surface should be distinguished: the homogeneous interface without any air pockets shown in Figure 10a (called the Wenzel interface, since the contact angle is given by the Wenzel equation or Eq. 6), and the composite interface with air pockets trapped between the rough details as shown in Figure 10b (called the Cassie or Cassie-Baxter interface, since the contact angle is given by equation (1.4)).

Equation (1.7) for the composite interface was derived using equations (1.4) and (1.6), and it could also be obtained independently. For this purpose, two sets of

interfaces are considered: a liquid-air interface with the ambient and a flat composite interface under the droplet, which itself involves solid-liquid, liquid-air, and solid-air interfaces. For fractional flat geometrical areas of the solid-liquid and liquid-air interfaces under the droplet, f_{SL} and f_{LA} , ($f_{SL} = 1 - f_{LA}$) the flat area of the composite interface is (Nosonovsky and Bhushan, 2005,2008a)

$$A_C = f_{SL}A_C + f_{LA}A_C = R_f A_{SL} + f_{LA}A_C \quad (1.9)$$

In order to calculate the contact angle in a manner similar to the derivation of equation (1.4), the differential area of the liquid-air interface under the droplet, $f_{LA}dA_C$, should be subtracted from the differential of the total liquid-air area dA_{LA} , which yields the Cassie-Baxter equation (equation (1.7)),

$$\cos \theta = \frac{dA_{LA} - f_{LA}dA_C}{dA_C} = \frac{dA_{SL}}{dA_F} \frac{dA_F}{dA_C} \frac{dA_{LA}}{dA_{SL}} - f_{LA} = R_f f_{SL} \cos \theta_0 - f_{LA} \quad (1.10)$$

The dependence of the contact angle on the roughness factor and fractional liquid-air area for hydrophilic and hydrophobic surfaces with a composite interface (Figure 12a) is presented in Figure 12b.

According to equation (1.10), even for a hydrophilic surface, the contact angle increases with an increase of f_{LA} . At a high value of f_{LA} , a surface can become hydrophobic; however, the value required may be unachievable, or the formation of air pockets may become unstable. Using the Cassie-Baxter equation, the value of f_{LA} at which a hydrophilic surface could turn into a hydrophobic one, is given by (Jung and Bhushan, 2006)

$$f_{LA} \geq \frac{R_f \cos \theta_0}{R_f \cos \theta_0 + 1} \quad \text{for } \theta_0 < 90^\circ \quad (1.11)$$

Figure 12c shows the value of f_{LA} requirement as a function of for four surfaces R_f for four surfaces with different contact angles, θ_0 . Hydrophobic surfaces

can be achieved above a certain with different contact angles, θ_0 . Hydrophobic surfaces can be achieved above a certain f_{LA} value as predicted by equation (1.11).

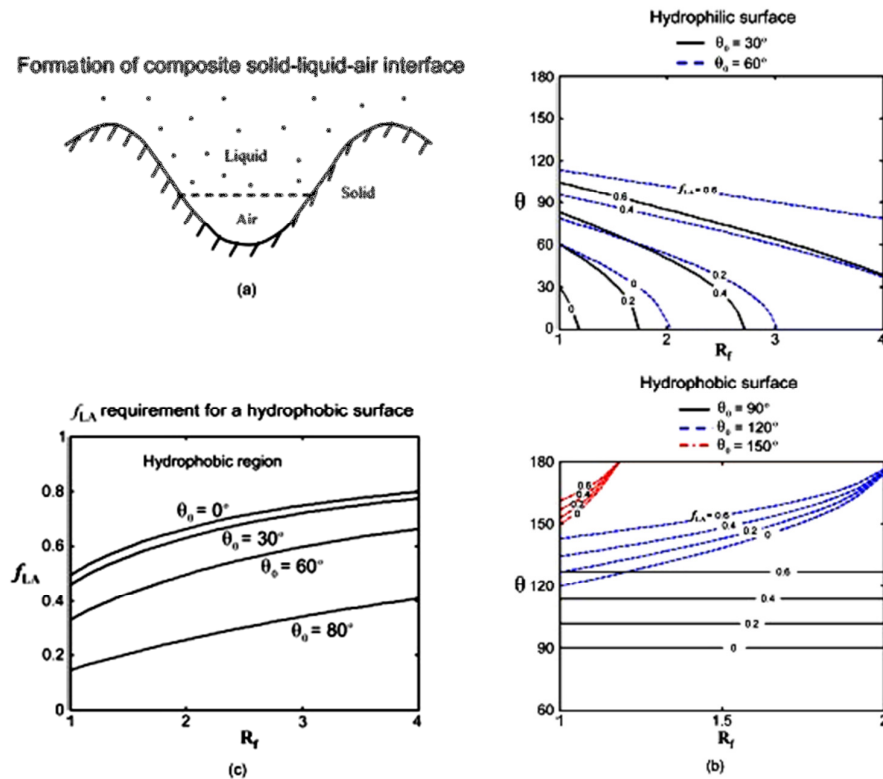


Figure 12. (a) Schematic of formation of a composite solid-liquid-air interface for rough surface, (b) contact angle for rough surface (θ) as a function of the roughness factor (R_f) for various f_{LA} values on the hydrophilic surface and the hydrophobic surface, and (c) f_{LA} requirement for a hydrophilic surface to be hydrophobic as a function of the roughness factor (R_f) and θ_0 (Jung and Bhushan, 2006).

The upper part of each contact angle line is the hydrophobic region. For the hydrophobic surface, contact angle increases with an increase in f_{LA} both for smooth and rough surfaces. Nosonovsky and Bhushan (2008a, 2009b) showed that spreading of a liquid over a rough solid surface continues until simultaneously equation (1.3) (the Young equation) is satisfied locally at the triple line and the surface area is minimum over the entire liquid-air interface.

1.4. Contact angle hysteresis

Contact angle hysteresis is another important characteristic of a solid-liquid interface. Contact angle hysteresis occurs due to surface roughness and heterogeneity. Since the concept of the contact angle was introduced, it was realized that this single parameter cannot completely characterize wetting. Furthermore, there is no one single value of the contact angle, but it can have a range of values $\theta_{rec} \leq \theta \leq \theta_{adv}$, where θ_{rec} and θ_{adv} denote the receding and advancing contact angles, respectively. The difference between the advancing and receding contact angle is called contact angle hysteresis.

Although for surfaces with roughness carefully controlled on the molecular scale it is possible to achieve contact angle hysteresis as low as $< 1^\circ$ (Gupta et al., 2005), hysteresis cannot be eliminated completely, since even atomically smooth surfaces have a certain roughness and heterogeneity.

1.5. The phenomenon of superhydrophobicity

There are lots of applications such as micro/nanoelectromechanical systems (MEMS/NEMS) which require surfaces with low adhesion and stiction (Bhushan, 1998, Bhushan, 2003; Bhushan, 2005a; Bhushan, 2005b; Bhushan, 2007b; Bhushan, 2007c; Bhushan. Et al., 1995). When the size of these devices decreases, the surface forces increase comparing to the volume forces, and adhesion and stiction incorporate and make a challenging problem for proper operation of these devices. Therefore the development of non-adhesive surfaces is crucial for many of emerging applications. It has been suggested by many researchers that using the highly water-repellent (superhydrophobic) surfaces may satisfy the need for the non-adhesive surfaces. This highly water-repellency property can be achieved by applying a micropatterned

roughness combined with hydrophobic coatings (Nosonovsky and Bhushan, 2005, 2006a, b, 2007b; Bhushan et al., 2007).

The wetting is characterized by the static contact angle, which is defined as the measurable angle that a liquid makes with a solid. There are several factors which affect the contact angle such as roughness and the manner of surface preparation, and its cleanliness (Adamson, 1990; Israelachvili, 1992). If the value of the static contact angle is $0 \leq \theta \leq 90^\circ$, the liquid wets the surface and the surface is called hydrophilic, whereas if the value of contact angle is $90^\circ \leq \theta \leq 180^\circ$, the liquid does not wet the surface and the surface is called hydrophobic. The term hydrophobic/philic, which was originally applied only to water (“hydro-” means “water” in Greek), is often used to describe the contact of a solid surface with any liquid. The term “oleophobic/philic” is used sometimes with regard to the wetting by oil. Surfaces with high energy, formed by polar molecules, tend to be hydrophilic, whereas those with low energy and built of non-polar molecules tend to be hydrophobic (Nosonovsky and Bhushan, 2008a).

Surfaces with the contact angle between 150° and 180° are called superhydrophobic. For liquid flow and other applications requiring low solid-liquid friction, in addition to high contact angle, superhydrophobic surfaces should also have very low water contact angle hysteresis. The contact angle hysteresis is the difference between the advancing and receding contact angles, which are two stable values.

One of the ways to increase the hydrophobicity or hydrophilicity is to make the surface rougher, so roughness-induced hydrophobicity has become a subject of extensive investigation. The effect of roughness on contact angle was studied by Wenzel (1936) and he found that the contact angle of a liquid with a rough surface is different from that with a smooth surface. Cassie and Baxter (1944) showed there are

some air pockets trapped in the crevices between the asperities of a rough surface, resulting in a composite solid-liquid-air interface, as opposed to the homogeneous solid-liquid interface. Shuttleworth and Bailey (1948) studied spreading of a liquid over a rough solid surface and found that the contact angle at the absolute minimum of surface energy corresponds to the values predicted by Wenzel (1936) or Cassie and Baxter (1944). Johnson and Dettre (1964) showed that the homogeneous and composite interfaces correspond to the two metastable equilibrium states of a droplet. Many researchers studied the metastability of the artificial superhydrophobic surfaces and found that if the interface is homogeneous or composite may depend on the history of the system (Bico et al. (2002), Marmur (2003, 2004), Lafuma and Quèrè (2003), Patankar (2003, 2004a), He et al. (2003)). However Extrand (2002) showed that whether the interface is homogeneous or composite depends on droplet size, due to the gravity. It was suggested also that the so-called two-level roughness, composed by superposition of two roughness patterns at different length-scale (Herminghaus, 2000; Patankar, 2004b; Sun et al., 2005), and fractal roughness (Shibushi et al., 1996) may lead to superhydrophobicity. Herminghaus (2000) showed that certain self-affine profiles may result in superhydrophobic surfaces even for wetting liquids, in the case the local equilibrium condition for the triple line (line of contact between solid, liquid and air) is satisfied. Nosonovsky and Bhushan (2005, 2006a) pointed out that such configurations, although formally possible, are likely to be unstable. Nosonovsky and Bhushan (2006a, b) proposed a stochastic model for wetting of rough surfaces with a certain probability associated with every equilibrium state.

It has been demonstrated experimentally, that roughness changes contact angle in accordance with the Wenzel model. Yost et al. (1995) found that roughness enhances wetting of a copper surface with Sn-Pb eutectic solder, which has a contact

angle of 15-20° for smooth surface. Shibuichi et al. (1996) measured the contact angle of various liquids (mixtures of water and 1,4-dioxane) on alkylketen dimmer (AKD) substrate (contact angle not larger than 109° for smooth surface). They found that for wetting liquids the contact angle decreases with increasing roughness, whereas for non-wetting liquids it increases. Semal et al. (1999) investigated effect of surface roughness on contact angle hysteresis by studying a sessile droplet of squalane spreading dynamically on multilayer substrates (behenic acid on glass) and found that an increase in microroughness slows the rate of droplet spreading. Erbil et al. (2003) measured the contact angle of polypropylene (contact angle of 104° for smooth surface) and found that the contact angle increases with increasing roughness. Burton and Bhushan (2005) measured contact angle with roughness of patterned surfaces and found that in the case of hydrophilic surfaces, it decreases with increasing roughness, and for hydrophobic surfaces, it increases with increasing roughness. Jung and Bhushan (2006; 2007) studied wetting properties of hydrophobic and hydrophilic leaves and patterned surfaces and found similar trends.

Researchers showed that superhydrophobic surfaces can be constructed by chemically treating surfaces with low-surface-energy substances, such as polytetrafluoroethylene, silicon, or wax, or by fabricating extremely rough hydrophobic surfaces directly (Shibuichi, 1996; Miwa et al., 2000; He et al., 2003; Kijlstra et al., 2002). Sun et al. (2005) studied an artificial polydimethylsiloxane (PDMS) replica of a lotus leaf surface and found the water contact angle of 160° for the rough surface, whereas for the smooth PDMS surface it is about 105°.

1.6.Composite materials and surfaces

It is readily realized that the most advanced turbine or aircraft design is of no use if adequate materials to bear the service loads and conditions are not available.

Whatever the field may be, the final limitation on advancement depends on materials. Composite materials in this regard represent nothing but a huge step in the ever constant endeavor of optimization in materials.

Nature is full of examples wherein the idea of composite materials is used. For example, the coconut palm leaf is nothing but a cantilever using the concept of fiber reinforcement. Wood is a composite of cellulose fibers in a lignin matrix. Bone is another example which consists of short and soft collagen fibers embedded in a mineral matrix. Besides these natural composites, there are many other engineering materials which are composites (Chawla, 1998; Wainwright et al., 1976). Glass fibers in resin, Portland cement, asphalt mixed with sand, and the carbon black in rubber are some examples. Thus the idea of the composite materials is not a new or recent one and they have been in use for a long time.

The origin of a distinct discipline of composite materials is not known. However one can roughly mark it as the beginning of the 1960s because more than 80 percent of all research in the field of composite materials has been done since 1965 (Clouser, 1973). From that time, there has been an increasing demand on stronger, stiffer and lighter materials with better overall performance and composite materials are increasingly providing the answers. According to Schier and Juergens (1983) which studied the impact of using composite materials on fighter aircraft, “composites have introduced an extraordinary fluidity to design engineering, in effect forcing the designer-analyst to create a different material for each application as he pursues savings in weight and cost”.

Figure 13 shows the comparison between composite materials and monolithic materials such as aluminum and steel in terms of mechanical properties. It clarifies the priorities of composite materials over the monolithic materials.

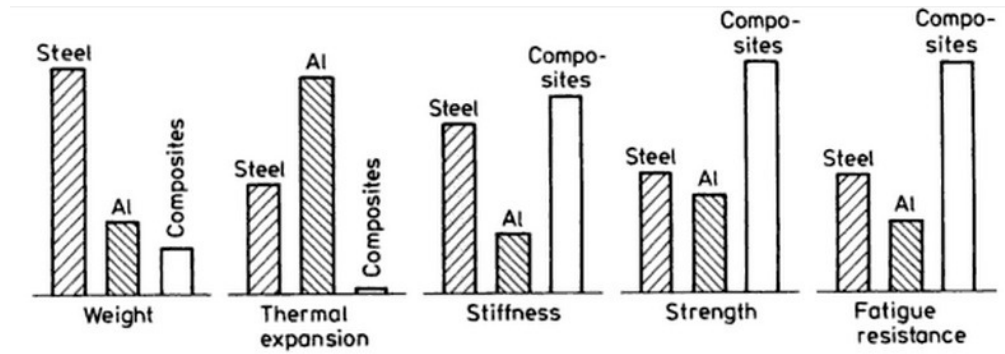


Figure 13. Comparison between conventional monolithic materials and composite materials (Deutsch, 1978).

In general, a typical composite material is a system of materials composing of two or more materials on a macroscopic scale. For example, concrete is made up of cement, sand, stones, and water. It is normally composed of reinforcement (fibers, particles, flakes, and/or fillers) embedded in a matrix (polymers, metals, or ceramics). The matrix holds the reinforcement to form the desired shape while the reinforcement improves the overall mechanical properties of the matrix.

1.6.1. Types of composite materials

Composite materials are usually classified by the type of reinforcement they use. This reinforcement is embedded into a matrix to strengthen the composite and hold it together. Reinforcements are not necessarily in the form of long fibers. There are other types of reinforcements such as particles, flakes, whiskers, discontinuous fibers, continuous fibers, and sheets. Since the great majority of the composite materials made by fiber reinforcement are stiffer and stronger than the composite materials made by the other common reinforcements, there is a great attraction to the fibrous reinforcements. The large source of natural fibrous materials are vegetables. For instance, flax, cotton, jute, sisal, hemp and ramie are cellulosic fibers which are used in the textile industry. Wood and straw are used in the paper industry. There are other types of natural fibers such as silk, wool and hair (Chawla, 1998).

The most common fiber reinforcement is glass fiber which is usually embedded in polymer matrices. Another example called Kevlar is an aramid fiber developed by Du Pont in 1965. It is much stronger, stiffer and even lighter than glass fiber and was first commercially used in the early 1970s as a replacement for steel in racing tires (Du Pont, 2007). Other types of high performance fibers are boron, carbon, silicon carbide, alumina and metallic fibers.

The matrix serves two paramount purposes; binding the reinforcement phases in place and deforming to distribute the stresses among the constituent reinforcement materials under an applied force. The demands on matrices are many. They may need to temperature variations, be conductors or resistors of electricity, have moisture sensitivity etc. This may offer weight advantages, ease of handling and other merits which may also become applicable depending on the purpose for which matrices are chosen. Solids that accommodate stress to incorporate other constituents provide strong bonds for the reinforcing phase are potential matrix materials. Ceramics, polymers and metals have found applications as matrix materials in the designing of structural composites, with commendable success. These materials remain elastic till failure occurs and show decreased failure strain, when loaded in tension and compression. Composites cannot be made from constituents with divergent linear expansion characteristics. The interface is the area of contact between the reinforcement and the matrix materials. In some cases, the region is a distinct added phase. Whenever there is interphase, there has to be two interphases between each side of the interphase and its adjoint constituent. Some composites provide interphases when surfaces dissimilar constituents interact with each other. Choice of fabrication method depends on matrix properties and the effect of matrix on properties of reinforcements. One of the prime considerations in the selection and fabrication of

composites is that the constituents should be chemically inert non-reactive. Figure 14 shows the common types of matrices.

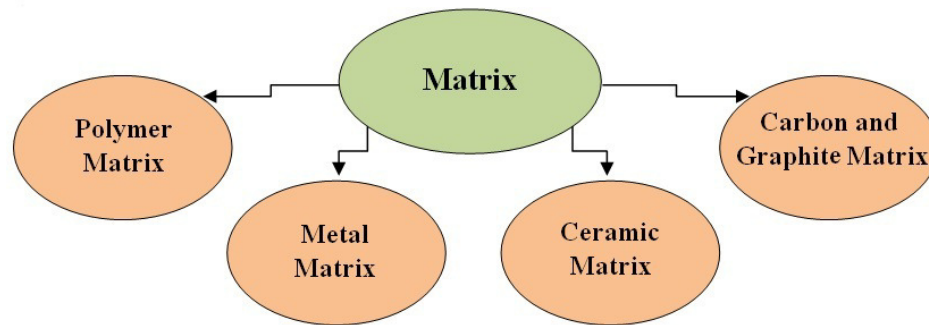


Figure 14. Schematic of different types of matrices.

The structure of the polymers is much more complex than metals or ceramics. They are cheap, readily processible and more resistant to chemicals than are metals. They also have lower strength, modulus and temperature use limits. There are two different types of polymers, based on their behavior, called thermosetting and thermoplastic polymers.

The metal matrix composite (MMC) systems afford high specific strength and modulus plus a service temperature capability much higher than that of polymer matrix composites (PMC). The excellent toughness and good environmental resistance of metallic matrices can result in quite superior MMC products. There are some important MMC systems such as Boron/aluminum, Carbon/aluminum, $\text{Al}_2\text{O}_3/\text{Al}$ and $\text{Al}_2\text{O}_3/\text{Mg}$, SiC/Al , and Eutectic or in situ composites.

The ceramic matrix composite (CMC) has basic differences with the other composites. In all nonceramic composites, the greater portion of the applied load is tolerated by fibers and this load depends on the ratio of fiber and matrix elastic moduli which can be very high while in CMCs it is low. The limited matrix ductility and high fabrication temperature in CMCs yield thermal mismatch between between

components which has a very important bearing on CMC performance (Chawla, 1998).

The carbon matrix composites (CAMCs), include carbon/carbon composites (CCCs), which consist of carbon matrices reinforced with carbon fibers. For decades, CCCs were the only significant type of CAMC. However, there are now other types of composites utilizing a carbon matrix. Notable among these is silicon carbide fiber-reinforced carbon, which is being used in military aircraft gas turbine engine components. The CAMCs have high strength at very high temperature, high stiffness, ablation resistance, high thermal conductivity and low density.

1.6.2. Surface of composite materials

The interface between matrix and reinforcement is rather rough instead of the ideal planar interface. It is important to discuss the intimate contact between matrix and reinforcement in terms of the wettability concept at the surface. For example in case of the PMCs, an intimate contact at the molecular level between the fiber and the matrix brings intermolecular forces into play with or without causing a chemical linkage between components. Under such a situation, the intermolecular force has impact on the adhesion force at the surface and affects the wettability property of the composite.

Baier et al. (1968) studied the mechanisms that assist or impede adhesion force in composite materials. They used wettability property as a key concept regarding this study. They found that the contact angle depends on the nature of the surfaces, whether or not absorbed gases or oxide films are present, and so on. Any impurities in or deliberate additions to the solid or liquid phase or a chemical reaction between the phases would affect the wettability. Good bonding implies that atomic or molecular bonds are formed uniformly all along the interface. However the strength

of bonding may vary from weak van der Waals to strong covalent bonds. An intimate contact at the atomic or molecular level aids in bonding. Wettability refers to the extent of intimate contact possible at the molecular level. As mentioned above, the term is used to describe the extent to which a liquid will wet a solid. A low contact angle indicates good wettability, while a high contact angle indicates poor wettability (Chawla, 1998).

Since the composites are made by combination of two or more materials, therefore their surface normally consists of various materials with different surface energy yields in different wettability properties. For such a composite material composed of n fractions, with the fractional area of f_1 to f_n and the contact angle of θ_1 to θ_n , respectively, we extend the Cassie equation (equation (1.6))

$$\cos \theta = f_1 \cos \theta_1 + f_2 \cos \theta_2 + \dots + f_n \cos \theta_n \quad (1.12)$$

CHAPTER TWO

2. METAL MATRIX COMPOSITES (MMCs)

2.1. Methods of MMC fabrication

In 1970s new fabrication methods using improved processing methods were introduced. The low cost of these processing methods was a key to their commercial success. Cornie et al. (1986) studied the new methods in processing of MMCs. They classified the fabrication methods of MMCs as follows:

- 1- Solid state fabrication techniques
- 2- Liquid state fabrication techniques
- 3- In situ fabrication techniques

In solid state fabrication method, boron fibers and aluminum foils are stacked in a resin based fugitive binder to make the desired fiber volume fraction. The matrix is heated and pressurized in vacuum to flow around the fibers, enclosing fibers in between. The temperature and time of heating are not very high in this process. Kreider and Prewo (1974) studied the fabrication details of boron/aluminum systems. Hot pressing under vacuum condition for stacked titanium and boron fibers sealed in stainless steel cans is also used for boron/aluminum systems (Smith and Froes, 1984).

For discontinuous fibers or whiskers, the powder metallurgy techniques are profitably used. In this method, a mixture of metal matrix and fibers is pressed and then sintered to attain the theoretical density of the matrix (Chawla, 1998).

A method called coextrusion or drawing is used in commercial production of superconducting composites. Other techniques of solid state fabrication are plasma spray, chemical and physical vapor deposition.

In liquid state fabrication method, liquid metal matrix infiltration fibers or fiber preforms are used. The infiltration process may be carried out under atmospheric or inert gas pressure or under vacuum condition. In case of long continuous fibers, the fibers should be thoroughly aligned before infiltration by matrix. However discontinuous fibers are stirred and mixed with the molten metal. Capillary action, pressure infiltration or vacuum infiltration may be applied to molten metal for penetration around the fibers. A specialized method in liquid state techniques is called squeeze casting. In this technique, high pressure is applied to the molten metal during the solidification process. This method is mostly used in the case of aluminum alloys which are difficult to cast by conventional methods like mold casting. The obtained matrix with this method is pore-free and fine-grained aluminum alloy. Insert of nickel containing cast iron or ceramic fiber reinforcement is used to provide wear resistance. Generally a porous fiber perform is placed into a die and then molten metal is injected to the preheated die on the bed of a hydraulic press. The next step is solidification of the matrix under pressure.

In situ fabrication technique controls the unidirectional solidification of a eutectic alloy results in a two phase microstructure with one of the phases, present in fiber form distributed in the matrix. For example for tantalum carbide (TaC), at low solidification rates, the TaC fibers are square in cross section, while at higher solidification rates, blades of TaC are formed. With increasing the solidification rates, the number of fibers per square centimeter is increased. A precast and homogenized rod of a eutectic alloy is melted under vacuum condition or in inert gas atmosphere and then is heated by induction. When reactive metals such as titanium are involved, the electron beam heating is also applied. The main advantages of eutectic superalloy

are improved rupture strength at high temperature, low creep rates, and thermal stability of the microstructure (Chawla, 1998; Walter, 1982).

2.2. Modeling of wetting

Since the 1990s, when new technologies emerged to produce microstructured surfaces, a huge amount of research work was done on design, fabrication, and characterization of superhydrophobic surfaces from various materials, ranging from polymers and ceramics to textiles, etc. A significant limitation on the practical application of the Lotus effect for self-cleaning is the sustainability of superhydrophobic microstructured coatings, which is often extremely vulnerable even to small wear rates and contamination (Verho et al., 2011).

It is much more difficult to produce a superhydrophobic metallic material than a polymer- or ceramic-based one, because metals tend to have higher surface energies (Kietzig et al., 2009; Tadmor et al., 2009; Bomashenko et al., 2006a; Bormashenko et al., 2006b). In the area of metallic superhydrophobic materials a number of advances have been made. Yet in the 1950s, Bikerman investigated wetting of stainless steel plates with different finishes with the contact angles around 90° and proposed that the surface roughness provides resistance for the sliding of water droplets. Since then, few studies of non-wetting metallic materials have been conducted. Qian and Shen (2005) studied the effect of the surface roughness induced by the chemical etching on metallic composites super-hydrophobicity. They used Al, Cu, and Zn specimens immersed into an etchant (a mixture of HCl, H₂O, and HF) at room temperature for time periods from 5 s to 15 s. Shirtcliffe and McHale (2005) studied the wettability of Cu-base superhydrophobic surfaces. They used Cu to form the base material and a coating to hydrophobize it. The removal or addition of material roughened the surface to control wetting by combining roughness with surface patterning. Sommers and

Jacobi (2006) achieved anisotropic wettability on an Al surface by controlling its surface micro-topography.

As mentioned before MMCs are composite materials which have a metallic matrix and a reinforcement of another metallic or non-metallic (ceramics, polymer, etc.) material (Rohatgi, 1993). MMCs with hydrophobic reinforcement can provide much broader opportunities than pure metals for design and fabrication of composite surfaces and readily supply the reinforcement hydrophobic fraction and surface roughness due to the reinforcement. However, superhydrophobic MMCs have not yet been explored in the literature. Furthermore, in a composite material the hydrophobic reinforcement is in the bulk of the material rather than at the surface and thus wear does not necessary leads do the deterioration of the hydrophobic coatings making these materials appropriate to the situations where traditional Lotus-effect coatings cannot be used. The use of composite materials with hydrophobic reinforcement in the bulk has already been suggested for concretes to prevent water penetration (Sobolev and Ferrada-Gutiérrez, 2005). In this section we investigate wetting of MMCs with the potential for various applications where self-cleaning sustainable surfaces are needed ranging from antifouling for water industry to magnetic tape-head interfaces (Mortazavi and Nosonovsky, 2011a; Mortazavi and Nosonovsky, 2011b).

If a composite material has a matrix and reinforcement with the volume fractions of f_m and f_r (so that $f_m + f_r = 1$) forming a rough surface the contact angle is then given by

$$\cos \theta = R_{f_m}(1 - f_r) \cos \theta_m + R_{f_r} f_r \cos \theta_r \quad (2.1)$$

where θ_m and θ_r are the contact angles for the matrix and reinforcement materials, and R_{f_m} and R_{f_r} are corresponding roughness factors. Note that for spherical reinforcement particles the roughness factor is equal to the ratio of half of the sphere's area $2\pi R^2$ to

the cross-sectional area πR^2 or $R_{fr}=2$. Solving for the reinforcement fraction yields the volume of the reinforcement fraction providing the desired contact angle θ

$$f_r = \frac{\cos \theta - R_{fm} \cos \theta_m}{R_{fr} \cos \theta_r - R_{fm} \cos \theta_m} \quad (2.2)$$

Further assuming $R_{fr}=2$, $R_{fm}=1$ (no roughness expect from the reinforcement particles), and $\theta=180^\circ$ (the superhydrophobic limit) yields

$$f_r = \frac{-1 - \cos \theta_m}{2 \cos \theta_r - \cos \theta_m} \quad (2.3)$$

which has a solution ($f_r < 1$) if $\theta_r > 120^\circ$. Thus it is difficult to produce a composite interface by only using the reinforcement roughness.

If water forms partial contact with the solid (composite or Cassie-Baxter) interface with the fractional solid liquid contact areas f_{SLm} and f_{SLr} (so that $f_{SLm} + f_{SAm} = 1$ and $f_{SLr} + f_{SAr} = 1$), the contact angle is given by

$$\cos \theta = R_{fm} (1 - f_r) f_{SLm} \cos \theta_m + R_{fr} f_r f_{SLr} \cos \theta_r - 1 + f_r f_{SLr} + (1 - f_r) f_{SLm} \quad (2.4)$$

Solving for the reinforcement fraction yields the volume of the reinforcement fraction providing the desired contact angle θ

$$f_r = \frac{\cos \theta - R_{fm} f_{SLm} \cos \theta_m + 1 - f_{SLm}}{R_{fr} f_{SLr} \cos \theta_r - R_{fm} f_{SLm} \cos \theta_m + f_{SLr} - f_{SLm}} \quad (2.5)$$

Making the assumptions of $R_{fr}=2$, $R_{fm}=1$, $f_{SLr}=1$, and $\theta=180^\circ$ yields

$$f_r = \frac{-f_{SLm} - f_{SLm} \cos \theta_m}{2 \cos \theta_r - f_{SLm} \cos \theta_m + 1 - f_{SLm}} \quad (2.6)$$

Let us apply equations (2.1) to (2.6) to the metallic (aluminum or copper) matrix with amorphous graphite reinforcement. For that end, we need to substitute material properties of these materials. We measured the water contact angle with graphite, aluminum and copper, which were used to produce MMC samples at the UWM Center for Composite materials, using the ramé-hart Model 250 standard

goniometer/tensiometer. We found the values of the contact angle equal to 140° , and 47.2° , and 47.7° , respectively. The results for metal matrices are close to those available in the literature (Wang et al., 2005). To measure the water contact angle of amorphous graphite, we compressed it at first to obtain a smooth surface. The main reason for high water contact angle of graphite is that the surface still remains rough even after compressing. Since we need the water contact angle of smooth graphite, we used the result of Fowkes and Harkins (1940). They measured the contact angle of water on smooth graphite using the tilting plate method and found a value of 86° . A similar result (84°) is reported by Morcos (1972). Figure 15 shows the variation of the contact angle of water droplet on surface of metal matrix composite reinforced by graphite particles versus reinforcement volume fraction ($\theta_m=47^\circ$, $\theta_r=86^\circ$), as obtained from equation (2.5) for various values of f_{SLm} . As it is seen in this figure, for $f_{SLm}>0.4$, the contact angle increases with increasing the reinforcement volume fraction, whilst for $f_{SLm}\leq 0.4$, it decreases with increasing the reinforcement volume fraction. Figure 16 shows the variation of f_{SLm} versus the reinforcement volume fraction, f_r , as obtained from equation (2.6) for cases where θ is equal to 150° and 180° . For this case, it is assumed that the matrix is made of aluminum whereas the reinforcement is made of a material with the water contact angle of 140° . As observed from this figure, the reinforcement volume fraction, f_r , is proportional to f_{SLm} . The area between two lines of $\theta = 150^\circ$ and $\theta = 180^\circ$ is called superhydrophobicity area.

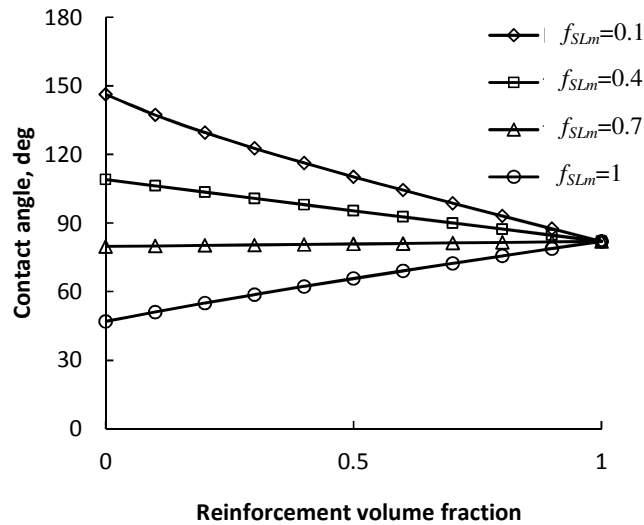


Figure 15. The water contact angle as a function of graphite reinforcement volume fraction for different values of f_{SLm} .

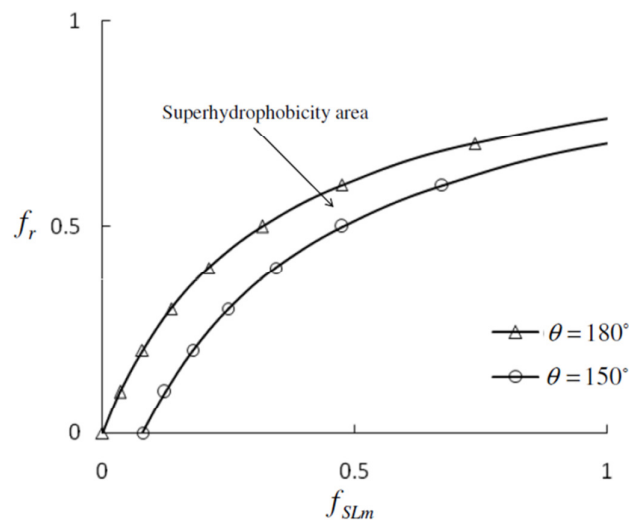


Figure 16. The variation of the reinforcement volume fraction, f_r , versus f_{SLm} .

To decouple the effect of reinforcement and matrix roughness we investigated experimentally wetting of composite materials with initially smooth surface and with the matrix roughness by etching, as described in the next section.

2.3.Experimental

In order to verify experimentally the models presented in the preceding section, we prepared eight samples of MMCs, four with a relatively smooth surfaces

and four roughened by etching, and measured their roughness and contact angles. In fact by using etching, we tried to simulate the corrosive and erosive wear on the samples which are probable especially due to environmental conditions.

2.3.1. Sample preparation

The four samples of Al- and Cu- based alloys and their graphite composites were sectioned to 2.0 cm × 1.5 cm × 0.2 cm pieces. The diameter of graphite particles used to make MMCs is estimated to be between 10 and 15 micrometers. We used Al and Cu because they are standard material which has been used as a matrix in literatures due to their high conductivity and ductility for making MMCs. Furthermore, Al- and Cu- based samples are easy to work with and inexpensive as well. Table 1 presents the chemical composition of the samples.

Table 1. Chemical composition of the samples.

Sample material	composition
Copper base alloy	Cu (79.0- 82.0%), Sn (2.5- 3.5%), Pb (6.3-7.7%), Zn (7.0-10%), P (0.02%), Al (0.05%) , Si (0.005%)
Copper-graphite composite	Cu (81%), Ni (5%), Fe (4%), Al (9%), Mn (1%), 60 % Vol. of graphite.
Al base alloy	Al (88%), Si (12%)
Al- graphite composite	Al (35%), Si (5%), 60% vol. of graphite

The samples were grinded and polished to create a smooth surface before the etching process. The grinding involved successive steps with 400, 600 and 1200 grit SiC paper. Polishing was done with a soft cloth impregnated with 1 micron alumina. The Scanning electron microscope (SEM) images of the polished samples are as shown in Figure 17.

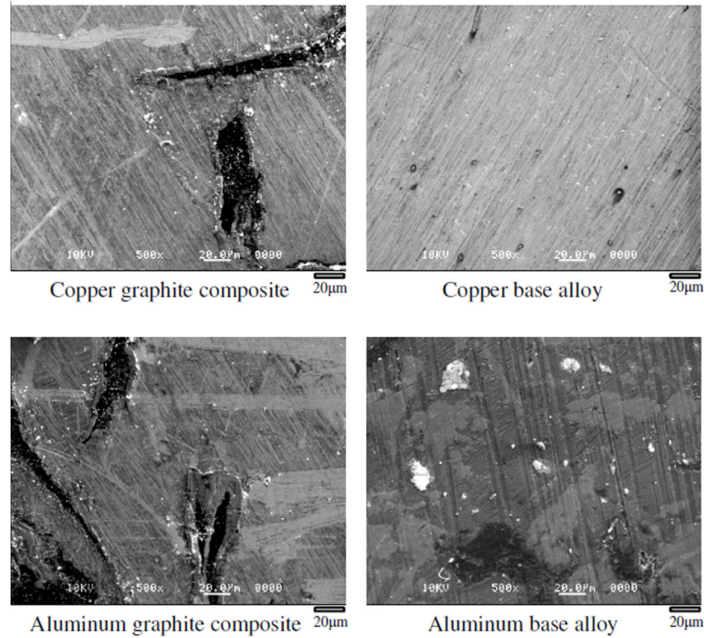


Figure 17. SEM images of polished samples.

After that four samples were etched. The reagents used in the selective dislocation etching are as follows (Qian and Shen, 2005). For the aluminum base alloy and the aluminum-graphite composite, the etchant consisted of 40 ml of 37 wt% HCl, 12.5 ml of H₂O and 2.0 ml of 48 wt% of HF. The etching time was set for 20 seconds, for a two cycle test. On the other hand, the etchants used for the copper-based alloy and the copper-graphite composite was 0.1 molar concentration of 37 wt% HCl. The etching time was 20 hours for both sample types. Since the Al- based samples are softer than Cu- based samples, these time periods for etching, make roughness of the same order of magnitude for all samples. All samples were washed, cleaned and dried before conducting experiments.

2.3.2. Sample characterization

The surface roughness of the samples was measured before etching process using a surface profilometer (Mitutoyo SurfTest. 402). The roughness of the samples was measured again after the etching. The roughness parameter measured in the

above cases is the average roughness value, R_a , defined as the arithmetic average of the absolute values of the roughness profile ordinates (Taha et al., 2010).

2.3.3. Contact angle measurement

The contact angles for all samples were measured. These measurements were done using the model 250 ramé-hart Goniometer. The measured contact angles showed that none of the surfaces were hydrophobic before etching, though surfaces of the composites had a higher contact angle with water (Table 2). This can be attributed to the graphite particles which has an effect on the surface roughness of the composites when compared to the base alloys. Figure 18 shows the contact angle profiles of these samples before etching.

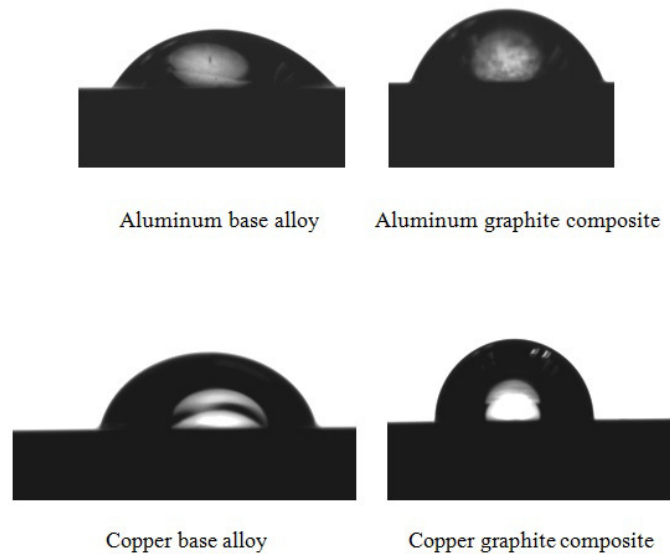


Figure 18. Images of water droplet on non-etched samples.

It is observed that only copper etched samples became hydrophobic, i.e., have the contact angle larger than 90° . The contact angle profiles for Al- and Cu- samples that were etched for 20 seconds and 20 hrs, respectively are as shown in Figure 19.

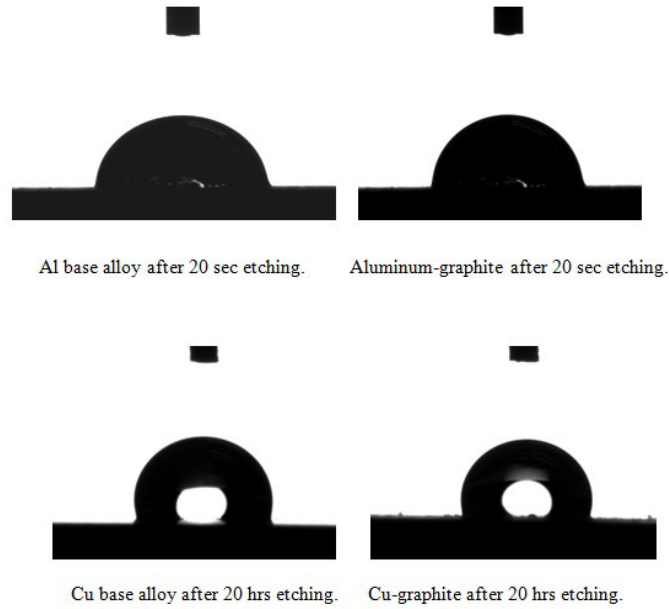


Figure 19. Images of water droplet on etched samples.

Table 2. Measured and calculated surface roughness and contact angles.

Sample	Measured			Calculated	
	Etching time	R_a (μm)	CA°	CA° (W, $f_{SLm}=1$)	CA° (CB, $f_{SLm}=0$)
Al base alloy	0	<0.2	47.2	47.2	—
Cu base alloy	0	<0.2	47.7	47.7	—
Al base alloy	20 s	16	82.5	0	73
Cu base alloy	20 h	8	99.4	29	97
Al-graphite composite	0	0.2	59.1	69	92
Cu-graphite composite	0	0.2	86.7	69	92
Al-graphite composite	20 s	14	86.5	56	81
Cu-graphite composite	20 h	8	87.3	64	88

2.4. Superhydrophobicity discussion

To compare the experimental results with the model and determine whether the homogeneous or composite interface is formed, the contact angle was calculated for the Wenzel (equation (2.1)) and Cassie-Baxter wetting regimes (equation (2.4)). The exact topographies of the matrix and reinforcement are not known, since the

surfaces are random to some extent. However, one can assume that nonetched samples have a relatively smooth matrix ($R_{fm} = 1$) and the surfaces roughness is caused by spherical reinforcement particles ($R_{fr} = 2$), as it is used in modeling the composite materials (Wang et al., 2005; Kestursayta et al., 2001; Rohatgi et al., 1991; Taha et al., 2010). For etched samples, the matrix roughness is significant in comparison with the reinforcement roughness, although the exact values of R_{fm} cannot be calculated from the measured R_a . However, the Wenzel roughness factor can be estimated as

$$R_{fm} = \sqrt{1 + (R_a/L)^2} \quad (2.7)$$

where L is a typical length of an asperity (Figure 20). Equation (2.7) is derived by calculating the length of a 2D surface built of asperities of length L . The value of R_a is a typical height of the asperities, and thus, the typical length is given by $(R_a^2 + L^2)^{1/2}$, which immediately yields the roughness factor value given by equation (2.7). For the Cassie-Baxter model, we assumed $f_{SLm} = 0$ (no matrix in contact with water) and $f_{SLr} = 1$ (entire reinforcement area is covered by water). Estimating the typical value of asperity length based on the SEM images and profilometer measurements $L = 10 \mu\text{m}$, the estimated roughness factors and the contact angles were further calculated (Table 2).

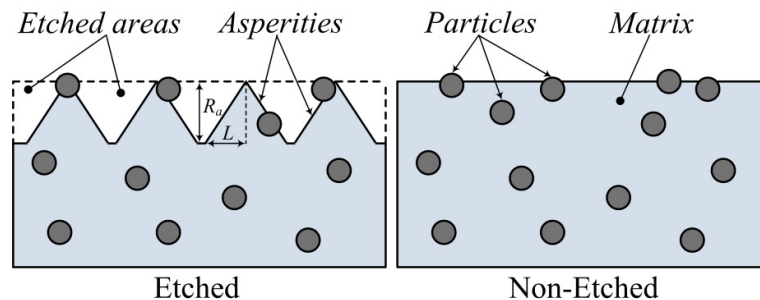


Figure 20. The schematic of surface before and after etching for a matrix reinforced with particles.

We investigated nonetched and etched samples of the base alloys and graphite-reinforced composites. The purpose was to decouple the effects of etching (roughness) and graphite reinforcement on wetting behavior of the MMCs. We observe from Table 2 that the Cassie-Baxter model predicts more accurate results for the etched samples than the Wenzel model with the exception of nonetched Al composite (59.1°), where the Wenzel model predicts better value of the contact angle (69°) than the Cassie-Baxter model (92°). It is noted that the calculated values are dependent on many estimated parameters, such as the values of the roughness factor as function of measured R_a , the values of the fractional areas of contact $f_{SLm} = 0$, and f_{SLr} . The significant difference between the Wenzel and Cassie-Baxter models is in the trends, which they predict, rather than in the particular values of the contact angle. The Wenzel model predicts that a hydrophilic material becomes more hydrophilic (i.e., has the contact angle decreases), whereas the Cassie-Baxter model predicts that an opposite trend can occur. The experimental data show that, for all samples, the contact angle increased with increasing roughness.

Therefore, the choice of the Cassie-Baxter model is justified by the experimental observation of the increasing contact angle. The results showed that both roughness and reinforcement are essential for obtaining a hydrophobic surface. For the roughened (etched) Al-graphite composite sample, the contact angle (86.5°) is larger than that for the smooth (nonetched) base alloy (47.2°), whereas the values for the roughened base alloy and smooth composite are 82.5° and 59.1°, correspondingly. This suggests that the effect of roughness is more significant than the effect of the reinforcement. For the Cu-graphite composite, both roughness and reinforcement have a significant effect on the contact angle (99.4° and 86.7°, as opposed to 47.7° for smooth base alloy) with the value observed for the reinforced

roughened sample of only 87.3° (i.e., even lower than that for the roughened base alloy). The difference in the behavior of the Al- and Cu-based composites can be partially attributed to the fact that much higher roughness ($R_a = 14 \mu\text{m}$ and $R_a = 16 \mu\text{m}$) was achieved on the Al samples even after short 20 s etching, that on the Cu samples ($R_a = 8 \mu\text{m}$ for both the base alloy and composite) after 20 h etching. Not surprisingly, the effect of roughness was much more pronounced on the Al samples.

The data suggest that MMCs can be used to synthesize materials with desired wetting properties by modifying the bulk properties (introducing the reinforcement) as opposed to the more traditional method of modifying surface properties (roughness). Materials with superhydrophobicity induced by their bulk properties are expected to be much more wear-resistant in comparison with the materials with the superhydrophobicity induced by the surface properties.

2.5. Effect of wear on superhydrophobicity

Effect of wear on a composite material is twofold. First, the matrix roughness factor, R_{fm} , can be changed due to material removal and evolve to a certain “equilibrium value” (Mortazavi and Nosonovsky, 2011a). This can affect the solid-liquid fractional area, f_{SLm} . Second, the reinforcement particles can be removed as matrix surface layers are removed due to the deterioration. However, new particles come in contact so it is expected that the values of R_{fr} and f_{SLr} do not change significantly. Table 3 presents the effect of wear on the contact angle of Al and Cu based alloys.

Table 3. Effect of wear on contact angle.

Sample	Force(N)	Velocity (RPM)	Wear (mm ³)	CA(non-worn), Ra=2μm	CA(worn), Ra=2μm
Al base alloy	40	261	0.8	68°	75°
Cu base alloy	60	200	0.6	86°	92°

2.6. Oleophobic metal matrix composites

When a surface repels oils or organic liquids, it is called oleophobic, which implies that the CA with oil is greater than 90°. Although the term oleophobicity usually applies to a three-phase solid-oil-air interface, it is also relevant to a three-phase solid-oil-water interface (referred to as underwater oleophobicity).

Most oleophobic surfaces are prepared by employing a surface microstructure, for example, a periodic array of pillars ranging in size from several micrometers to dozens of micrometers. Hierarchical structures, with nanoroughness imposed on the microstructure, are used as well. However, microstructured oleophobic surfaces have a huge limitation in their application. They are extremely vulnerable to even moderate rates of wear and deterioration in aggressive underwater and other environments. To design more durable oleophobic surfaces, we suggested earlier using metal matrix composites (MMCs) introducing hydrophobic reinforcement into the bulk of the material, rather than at its surface (Nosonovsky et al., 2011). Such a method provides the micropatterned surface roughness and heterogeneity needed for oleophobicity. When wear, corrosion, or erosion cause a surface layer to become deteriorated or removed, due to the presence of oleophobic reinforcements making roughness at the surface, the surface still remains oleophobic. A different trend in the development of sustainable oleophobic surfaces involves combining self-healing, self-lubricating, and self-cleaning abilities (Nosonovsky, 2011). These three are features of novel materials

with an embedded capacity for self-organization. We will investigate oleophobic surfaces and their applications in more details in chapter 4.

2.7. Contact angle hysteresis on metal matrix composites

Beside the CA, another important parameter regarding the wettability property of a surface is CA hysteresis. Furthermore, there is no one single value of the contact angle, but it can have a range of values $\theta_{rec} \leq \theta \leq \theta_{adv}$, where θ_{rec} and θ_{adv} denote the receding and advancing contact angles, respectively. The contact angle can be measured also on a tilted surface (Figure 21), although it is recognized that the values measured in this way do not always provide true values of the advancing and receding angles (Krasovitski and Marmur, 2005).

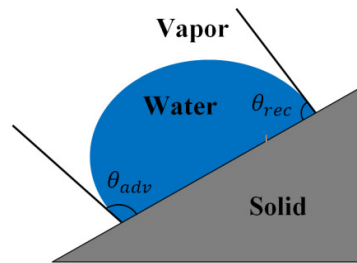


Figure 21. Advancing and receding contact angles for a droplet on a tilted solid surface.

The difference between the advancing and receding CA is called CA hysteresis. Originally, CA hysteresis was associated with surface contaminants. Lord Rayleigh (1891) noted that for contaminated glass surfaces the CA can vary significantly, since “if after the drop is deposited, some of the liquid is drawn off, the angle may be diminished almost to zero.” This phenomenon was described in a letter from a German scientist Agness Pockels, who had no formal education and made observation on dishes in a kitchen sink. She observed that water droplets behaved

differently on clean and contaminated glass surfaces. She wrote a letter to Rayleigh who published it in the journal *Nature* (Pockels, 1914):

“The surface tension of a strongly contaminated water surface is variable; that is, it varies with the size of the surface. The minimum of the separating weight attained by diminishing the surface is to the maximum, according to my balance, in the ratio of 52: 100. If the surface is further extended, after the maximum tension is attained, the separating weight remains *constant*, as with oil, spirits of wine, and other normal liquids. It begins, however, to diminish again, directly the partition is pushed back to the point of the scale at which the increase of tension ceased. The water surface can thus exist in two sharply contrasted conditions; the *normal* condition, in which the displacement of the partition makes no impression on the tension, and the *anomalous* condition, in which every increase or decrease alters the tension” (Rayleigh, 1891).

This phenomenon was later investigated by Pockels (1914), Ablett (1923), and Adam and Jessop (1925) who wrote: “In the extreme cases, the angle when the liquid is advancing over the solid may be 60° greater than when it is receding. It is not necessary that there should be actual motion, for a force on the liquid tending to move it has the same effect. The phenomenon is obvious on inspection of a drop of water on slightly dirty glass plate; it appears to have been first described in detail by Pockels. The cause of this dragging effect (often called “hysteresis” of the angle of contact) seems to us to lie, not in any absorption of the liquid by the solid, but in a simple friction of the liquid on the surface” (Adam and Jessop, 1925).

Adam and Jessop (1925) related CA hysteresis to the “friction force” per unit length of the triple line, F , acting upon the droplet in its motion as

$$\gamma_{LV}(\cos \theta_{adv} - \cos \theta_{rec}) = F$$

(2.8) Using similar models, Good (1952) and Shepard and Bartell (1953) investigated later the effect of surface roughness on CA hysteresis, which is similar to the effect of surface contamination or chemical heterogeneity.

When a water droplet spreads along a solid surface with low velocity (so that the effect of viscosity is negligible), CA hysteresis serves a measure of energy dissipation due to the wetting/dewetting cycle. The similarity of CA hysteresis with the so-called adhesion hysteresis (the difference between the energy spent for the separation of two surfaces and gained by bringing them together) and with dry friction was discussed in the literature (Nosonovsky, 2007a).

In the recent studies of superhydrophobicity it has been emphasized that a superhydrophobic surface should not only have a high CA above 150°, but in addition, it should possess small CA hysteresis (Carré and Mittal, 2009). Despite this, reports have appeared recently in the literature that a material can be superhydrophobic and simultaneously strongly adhesive to water (Jin et al., 2005). This phenomenon is known as the “petal effect” since it is typical for certain rose petals which are characterized by a high CA and large CA hysteresis (Nosonovsky and Bhushan, 2008a) . The discovery of the petal effect caused a discussion in the literature as to whether superhydrophobicity is adequately characterized only by a high CA and whether a surface can have a high CA but at the same time strong water adhesion. The phenomenon of the large CA hysteresis and high water adhesion to rose petals (and similar surfaces), as opposed to small CA hysteresis and low adhesion to Lotus leaf, was observed by several research groups (Bormashenko et al., 2009; Chang et al., 2009). Bormashenko et al. (2009) reported a transition between wetting regimes, e.g., the penetration of liquid into the micro/nanostructures.

Li and Amirfazli (2007) argued that since “superhydrophobicity” means a strong fear of water or lacking affinity to water, “the claim that a superhydrophobic surface also has a high adhesive force to water is logically contradictory.” However, the experimental demonstration of the rose petal effect made it clear that the CA as a sole parameter is not sufficient to characterize the adhesion of a liquid to a solid, because such adhesion may be different depending on the condition (such as the normal or shear mode of loading). Gao and McCarthy (2008) suggested several illustrative experiments showing that even Teflon (polytetrafluoroethylene), which is usually considered very hydrophobic, under certain conditions can behave in a hydrophilic manner, i.e., it can have affinity to water. They argued that the concepts of “shear and tensile hydrophobicity” should be used, which makes wetting (“solid-liquid friction”) similar to the friction force, as has been pointed out in the literature earlier (Nosonovsky, 2007a).

Wang and Jiang (2007) suggested five superhydrophobic states (Wenzel’s state, Cassie’s state, so-called “Lotus” and “Gecko” states, and a transitional state between Wenzel’s and Cassie’s states). It may be useful also to see the transition between the Wenzel, Cassie, and dry states as a phase transition and to add the ability of a surface to bounce off water droplet to the definition of superhydrophobicity. In addition, there is an argument on how various definitions of the CA hysteresis are related to each other (Krasovitski and Marmur, 2005; Bormashenko et al., 2009; Chang et al., 2009; Bormashenko et al., 2007a; Xia and Jiang, 2008).

According to early Wenzel (1936) and Cassie & Baxter (1944) models, there are two regimes of wetting of a rough surface by water: a homogeneous regime with a two-phase solid-water interface and a non-homogeneous or composite regime with a three-phase solid-water-air interface (air pockets are trapped between the solid surface

and water). Both models predict that surface roughness affects the water contact angle (CA) and can easily bring it to extreme values close to 180° (superhydrophobicity) or close to 0° (superhydrophilicity). The studies of wetting of microstructured surfaces have concentrated on the investigation of these two regimes and the factors which affect the transition between the regimes (Bormashenko et al., 2007a).

Recent experimental findings and theoretical analyses made it clear that the early Wenzel and Cassie-Baxter models do not explain the complexity of interactions during wetting of a rough surface which can follow several different scenarios (Jin et al., 2005; Wang and Jiang, 2007; Feng et al., 2008; Xia and Jiang, 2008; Gao and McCarthy, 2008; McHale, 2009; Bhushan and Nosonovsky, 2010). Wang and Jiang (2007) suggested five superhydrophobic states (Wenzel's state, Cassie's state, so-called "Lotus" and "Gecko" states, and a transitional state between Wenzel's and Cassie's states). Bhushan and Nosonovsky (2010) pointed out that for a hierarchical surface (with nanoroughness superimposed on microroughness), there can exist nine modes of wetting depending on whether water penetrates in micro and nanopores. As a result, there are several modes of wetting of a rough surface, and, therefore, wetting cannot be characterized by a single number such as the CA (Figure 22). Bormashenko (2012) argued that for materials with positive disjoining pressure, nano-cavities will be filled first and thus the states in the upper row of Figure 22 are unlikely.

Furthermore, when oleophobicity is investigated, the standard Wenzel (solid-liquid) and Cassie-Baxter (solid-liquid-air) wetting states can be extended for general three-phase (solid-water-air, solid-oil-air, and solid-oil-water) and four-phase (solid-oil-water-air) interfaces (Hejazi and Nosonovsky, 2012). In the present paper we discuss CA hysteresis in such complex systems.

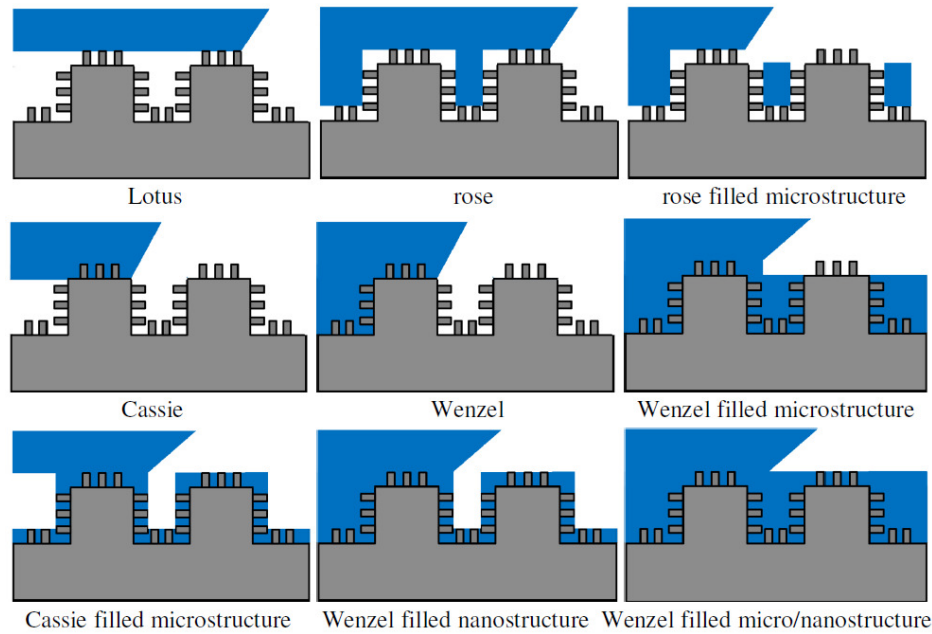


Figure 22. Schematic of nine wetting regimes for a rough surface characterized by no penetration, partial penetration, and complete penetration of water into microroughness, nanoroughness and both micro and nanoroughness (Bhushan and Nosonovsky, 2010).

2.7.1. Origins of contact angle hysteresis

Several theories explaining CA hysteresis due to surface roughness and chemical heterogeneity have been proposed. The simplest model attributes hysteresis to pinning of the triple line by sharp asperities at the surface. Two surfaces come together at a sharp edge (Figure 23a), so the value of the CA is not unique at the edge, being in the range of values from the minimum value (corresponding to the slope on the left of the edge) to the maximum value (corresponding to the slope on the right of the edge). When liquid front advances, the triple line will be pinned at the edge until the CA reaches its maximum value. Similarly, when liquid recedes, the triple line is pinned until the CA reaches its minimum value. Therefore, varying surface slope results in CA hysteresis.

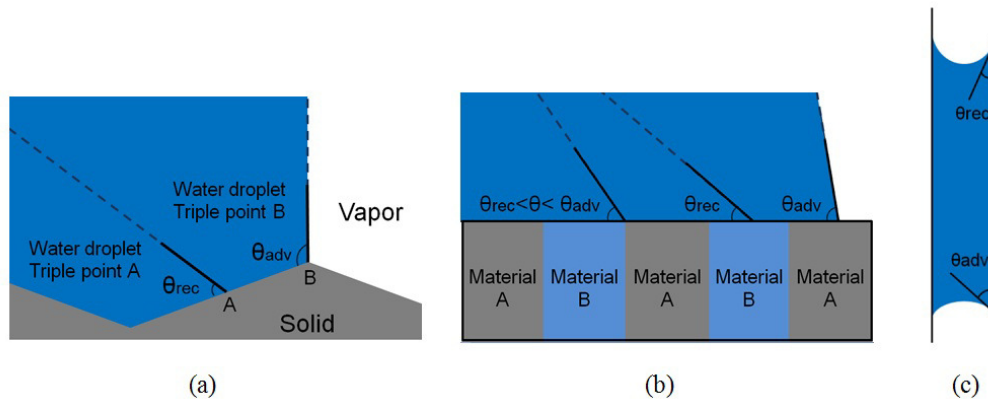


Figure 23. Schematic of advancing and receding contact angles (a) due to surface slope and (b) heterogeneity (c) water column suspended in a capillary due to CA hysteresis.

In a similar manner, chemical heterogeneity or contamination leads to CA hysteresis. If a surface is composed of spots with different surface energies, water will cover the spots with lower energy first and leave them last effectively resulting in CA hysteresis (Figure 23b).

The energy required to separate liquid and solid is greater than the energy gained by bringing them together. This occurs due to molecular reorientation and rearrangement. This difference constitutes the adhesion hysteresis, ΔW . Assuming a smooth surface, the adhesion hysteresis for a smooth surface, ΔW_0 is given by

$$\Delta W_0 = (\cos \theta_{adv} - \cos \theta_{rec}) \gamma_{LV} \quad (2.9)$$

In other words, the CA hysteresis is equal to dissipated energy during the motion of a droplet. This dissipation can occur either in the bulk of the liquid, at the solid-liquid interface or at the triple line. The bulk dissipation (3D) is mostly due to the viscosity and it can be eliminated in the quasi-static limit of low velocity, however, the interfacial (2D) and triple line (1D) dissipation cannot be eliminated completely and both contribute to CA hysteresis. Therefore, CA hysteresis involves a

term proportional to the contact area and a term proportional to the length of the triple line.

CA hysteresis is responsible for holding a water column suspended in a vertical capillary of radius R (Figure 23c), so that the weight of the column $\rho g \pi R^2 H$ is balanced by the “friction” force given by equation (2.8) yielding (de Gennes et al., 2004)

$$\frac{2\gamma_{LV}}{R} (\cos \theta_{adv} - \cos \theta_{rec}) = \rho g H \quad (2.10)$$

Extrand (1998) estimated the pressure difference, ΔP , across the water-air interface, on the basis of the Laplace equation for the pressure drop, as

$$\Delta P = \frac{2\gamma_{LV} \sin \theta}{r} \quad (2.11)$$

where r is the contact radius. By further relating the pressure to energy hysteresis ΔG , he obtained

$$\Delta G = - \left(\frac{RT}{A} \right) \ln \left(\frac{\sin \theta_{rec}}{\sin \theta_{adv}} \right) \quad (2.12)$$

where R is the ideal gas constant, T is the absolute temperature and A is the molar surface area of the solid which can be obtained by

$$A = \left(\frac{M}{\rho} \right)^{2/3} N_A^{1/3} \quad (2.13)$$

Where M is the molecular weight, ρ is the density and N_A is Avogadro's number. The expression was modified in (Bormashenko et al., 2008).

For a droplet on an inclined surface with a tilt angle of α , one can relate equation (2.11) to the hydrostatic pressure difference at the advancing and receding edges, $\Delta P = \rho g H$, where $H = 2r \sin \alpha$, yielding

$$\gamma_{LV} (\sin \theta_{adv} - \sin \theta_{rec}) = r^2 \rho g \sin \alpha \quad (2.14)$$

Further assuming that the $(\theta_{adv} - \theta_{rec})$ is small and using the trigonometric identity $\sin x - \sin y = 2 \cos \frac{x+y}{2} \sin \frac{x-y}{2}$ and $\theta = (\theta_{adv} - \theta_{rec})/2$ yields

$$\gamma_{LV} \cos\theta(\theta_{adv} - \theta_{rec}) = r^2 \rho g \sin\alpha \quad (2.15)$$

Equation (2.15) relates the tilt angle with CA hysteresis. Furthermore, combining equation (2.14) with equation (1.1) we obtain the relationship between the excess pressure and change in the contact angle as:

$$\Delta\theta = \frac{\Delta Pr}{\gamma_{SV} - \gamma_{SL}} \quad (2.16)$$

Note that equations (2.8) and (2.14) seem to be in contradiction with each other. While equation (2.8) reflects the balance of shear (“friction”) forces at the surface, equation (2.14) deals with the normal forces, since $\gamma_{LV} \sin\theta$ is the normal component of the liquid-vapor tension, which is balanced by the Laplace and hydrostatic excess pressures in the droplet and thus the difference in this component at the two edges of the droplet is proportional to the hydrostatic pressure difference.

2.7.2. Modeling wetting/dewetting in multiphase systems

Underwater oleophobicity is of interest for various applications in water industry (piping systems, water meters and heaters) and marine devices (micro/nanochannels, ships, ...) where antifouling is important. Self-cleaning properties of oleophobic materials can reduce the undesirable growth of microorganisms and contaminants referred to as biofouling (Nosonovsky and Bhushan, 2009a; Nosonovsky and Bhushan, 2009b).

For a rough surface, there could be a more complex interface than two or three phase interface which are predicted by the basic Wenzel and Cassie models. When there are both water and air trapped between oil droplet and a solid surface immersed in water, a multi-phase interface can form (Hejazi and Nosonovsky, 2012; Nosonovsky et al., 2011). Also the multi-phase interface of solid-oil-water-air can form when there is a porous material filled with a liquid lubricant, which is a method

to design durable self-lubricating, self-healing, and self-cleaning surfaces (Wong et al., 2011; Nosonovsky, 2011).

2.7.2.1. CA in multiphase systems

When an oil droplet is placed on a rough solid surface immersed in water, so that the oil fills in the crevices of the surface, the CA of the oil droplet in water (two-phase system), $\theta_{OW,2}$, is given by

$$\cos \theta_{OW,2} = \frac{\gamma_{OA} \cos \theta_{SO} - \gamma_{WA} \cos \theta_{SW}}{\gamma_{OW}} R_f \quad (2.17)$$

where, γ_{SO} , γ_{SW} and γ_{OW} are free energies for solid-oil, solid-water and oil-water interfaces and R_f is the roughness factor of the surface (Hejazi and Nosonovsky, 2012).

$\cos \theta_{SO}$ and $\cos \theta_{SW}$ can be obtained by

$$\cos \theta_{SO} = \frac{\gamma_{SA} - \gamma_{SO}}{\gamma_{OA}} \quad (2.18)$$

$$\cos \theta_{SW} = \frac{\gamma_{SA} - \gamma_{SW}}{\gamma_{WA}} \quad (2.19)$$

If an oil droplet is placed on a rough solid surface under water so that water is trapped inside crevices between oil and the solid surface, the three-phase solid-oil-water interface can form, which is usually referred to as the Cassie-Baxter state. In this case, the CA of oil droplet under water (three-phase system), $\theta_{OW,3}$, is given by

$$\cos \theta_{OW,3} = \cos \theta_{OW,2} f_{SO} + 1 - f_{SO} \quad (2.20)$$

where f_{SO} is the fractional solid-oil contact area.

In a particular case, when an oil droplet is deposited on a rough solid surface immersed in water, the water and air bubbles are trapped inside crevices between solid surface and oil droplet which causes a more complex four-phase solid-oil-water-air interface which is also called a multiphase system. In this case, the CA of oil droplet under water (four-phase system), $\theta_{OW,4}$, is given by

$$\cos \theta_{OW,4} = \cos \theta_{OW,2} f_{SO} + f_{SO} + 2f_{OW} - 1 \quad (2.21)$$

where f_{OW} is the fractional oil-water contact area.

2.7.2.2. CA hysteresis in multiphase systems

In the preceding section, we explained the CA of two-, three- and four-phase systems. To measure the CA hysteresis for each system, we need to consider advancing and receding CA of each system separately.

As discussed in the preceding section, the difference between the two values of advancing CA, θ_{adv0} , and receding CA, θ_{rec0} , is related to the difference in interfacial energies during loading and unloading such that

$$\cos \theta_{adv0} - \cos \theta_{rec0} = \frac{\Delta W_0}{\gamma_{OW}} \quad (2.22)$$

For a micropatterned surface built of flat-top square pillars, when there is a two-phase underwater system, the CA hysteresis is given by

$$\cos \theta_{adv} - \cos \theta_{rec} = \frac{\Delta W_0}{\gamma_{OW}} + cS_p^2 = \cos \theta_{adv0} - \cos \theta_{rec0} + cS_p^2 \quad (2.23)$$

where c is a constant which depends on the density of pillars on the surface and $S_p = W/P$ is the spacing factor (Nosonovsky and Bhushan, 2008a). W and P are the width and pitch of the pillars, respectively (Figure 24).

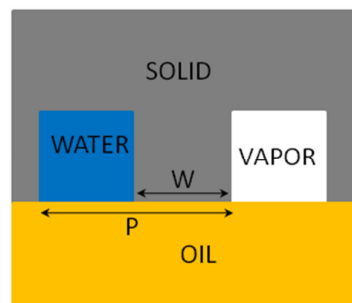


Figure 24. Schematic of a four-phase interface showing both water and vapor trapped at the interface between the solid and oil.

For the case when there are water bubbles trapped inside crevices (three-phase system), the fraction of the solid-oil area should be introduced in adhesion hysteresis so that $\Delta W = f_{SO}\Delta W_0$. The CA hysteresis then is given by

$$\cos \theta_{adv} - \cos \theta_{rec} = \frac{f_{SO}\Delta W_0}{\gamma_{OW}} + cS_p^2 = f_{SO} (\cos \theta_{adv0} - \cos \theta_{rec0}) + cS_p^2 \quad (2.24)$$

For a more complex interface consisting of four phases of solid, oil, water and the air, the interfacial energy of oil-air should be taken into account so that the CA hysteresis then is given by

$$\begin{aligned} \cos \theta_{adv} - \cos \theta_{rec} &= f_{SO}\Delta W_0 \left(\frac{1}{\gamma_{OW}} + \frac{1}{\gamma_{OA}} \right) + cS_p^2 = \\ &f_{SO} (\cos \theta_{adv0} - \cos \theta_{rec0}) \frac{\gamma_{OW} + \gamma_{OA}}{\gamma_{OA}} + cS_p^2 \end{aligned} \quad (2.25)$$

Figure 25 shows how the CA hysteresis changes versus spacing factor for different values of solid-oil fraction. It is observed that with increasing the spacing factor, S_p^2 , CA hysteresis increases for two-, three- and four-phase interfaces. It is seen in Figure 25d that CA hysteresis for four-phase interface is greater than that for three- and two-phase interfaces.

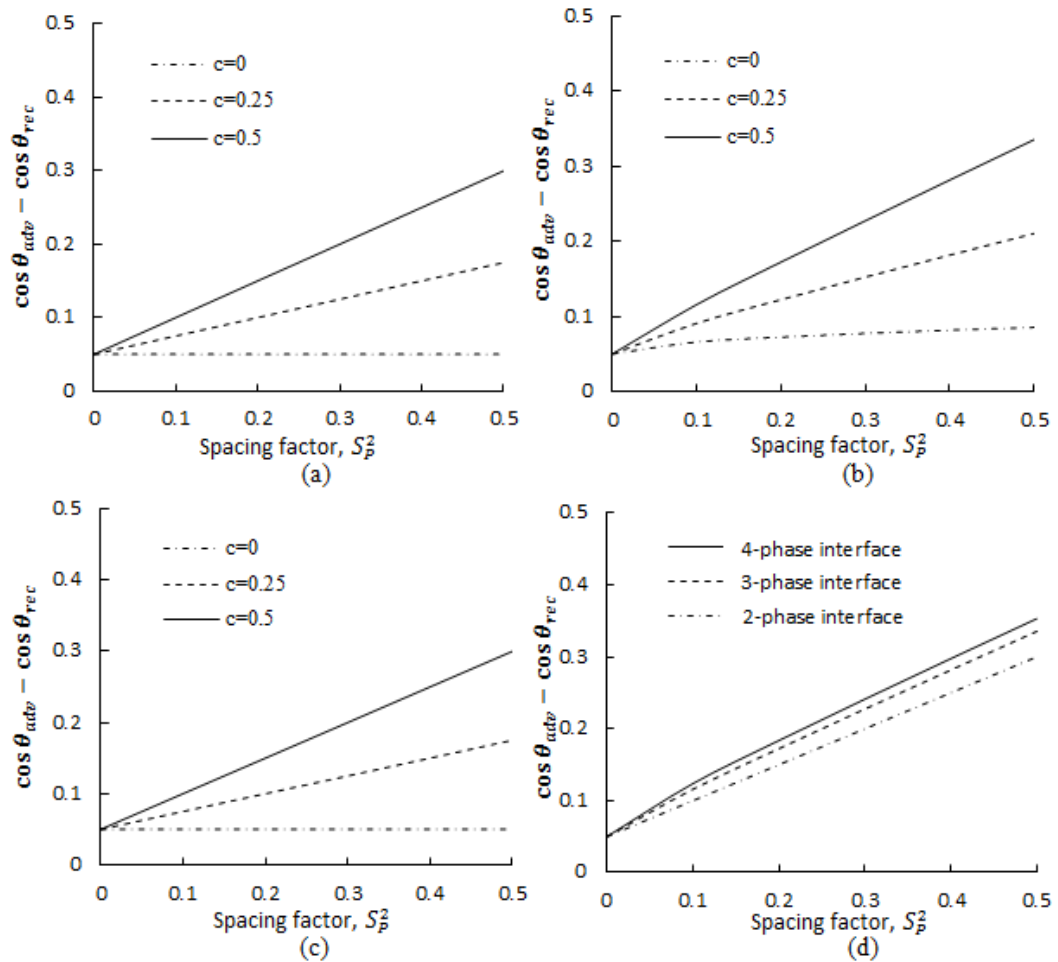


Figure 25. CA hysteresis for different values of the constant c . (a) Two-phase interface, (b) Three-phase interface, (c) Four-phase interface, (d) Comparison of the CA hysteresis of two-, three- and four-phase interfaces.

2.7.3. Experimental observation

In order to separate the effect of the triple line from the contact area effect on the CA hysteresis, we compared hysteresis for water and vegetable oil droplets and air bubbles on the same surface. We prepared three samples of gray iron with different surface roughnesses. The samples were washed with deionized water and then were ground and polished through successive grinding steps with 600, 1200 and 2400 grit silicon carbide papers and finally polished with a soft cloth impregnated with 1 μm

silica particles. Then we measured the arithmetic mean value of surface roughness, R_a , of the three samples by a profilometer (Mitutoyo SurfTest, 40) which were found to be 0.3 μm , 0.2 μm and 0.1 μm , respectively. To remove the polishing debris, the samples were placed in acetone for 10 minutes. Finally, the samples with different surface roughnesses were dried in air. The procedure is described by Nosonovsky et al. (2011).

Table 4. Advancing and receding contact angles and hysteresis.

		Air-Water droplet				Underwater-Air bubble			Underwater-Oil droplet		
Sample 1 ($R_a=0.1 \mu\text{m}$)	Tilt angle °	0	9	22	90	0	9	22	0	25	90
	Back CA °	60	57	53	42	98.1	101	88	42.3	33	28
	Front CA °	60	61	63	64	98.1	111	114	42.3	38	40
	CA difference °	0	4	10	22	0	10	26	0	5	12
Sample 1 ($R_a=0.2 \mu\text{m}$)	Tilt angle °	0	9	22	90	0	9	24	0	25	90
	Back CA °	63	62	56	45	98.8	105	95	42.6	33	29
	Front CA °	63	66	68	69	98.8	118	123	42.6	42	50
	CA difference °	0	4	12	24	0	13	28	0	9	21
Sample 1 ($R_a=0.3 \mu\text{m}$)	Tilt angle °	0	9	22	90	0	9	27	0	25	90
	Back CA °	68	62	56	44	101.5	107	103	44.4	41	35
	Front CA °	68	66	69	70	101.5	121	133	44.4	52	57
	CA difference °	0	4	13	26	0	14	30	0	11	22

We studied CA hysteresis for the three cases: first solid-water-air interface with water droplet placed on the solid surface in the air (Figure 26), second solid-water-air with air bubble placed on the solid surface immersed in water (Figure 27), and third solid-oil-water with oil droplet placed on the solid surface immersed in water (Figure 28). For all experiments, the droplets and air bubbles of 5-6 μL volume were deposited on the solid surface. The advancing and receding CAs for samples were measured by a standard ramé-hart goniometer/tensiometer, model 250, for different tilt angles. The results are presented in Table 4.

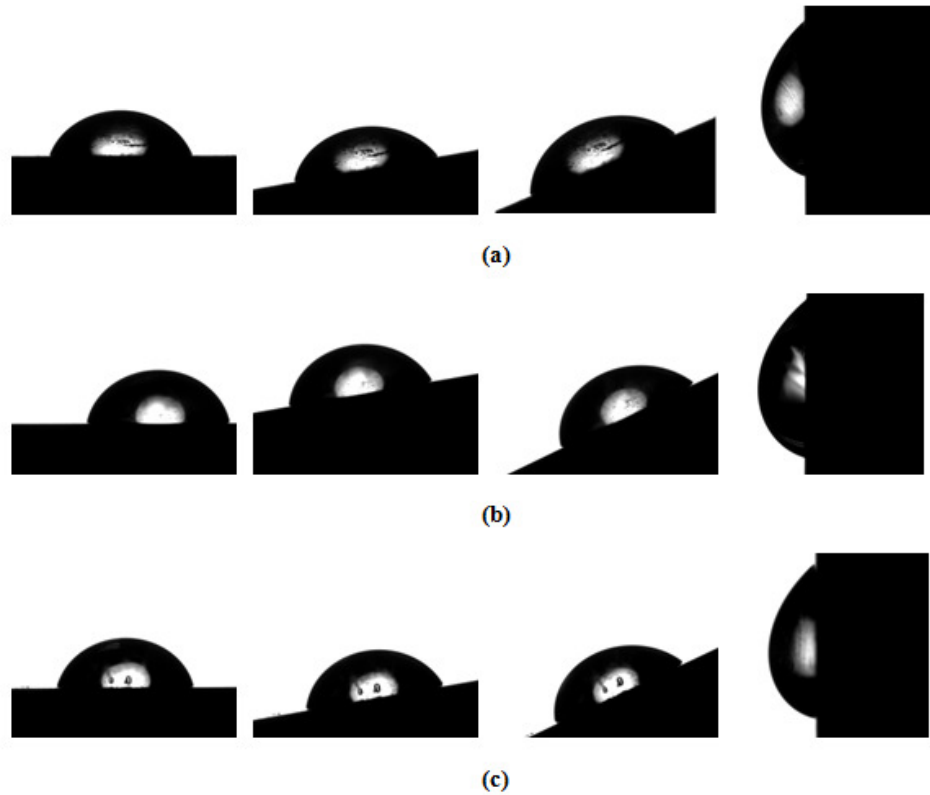


Figure 26. Advancing and receding CAs of water droplet on gray iron in air for the three samples with roughness. The angle between the surface and horizontal line is 0, 9, 22 and 90 degrees from left to right, respectively. (a) $R_a=0.1 \mu\text{m}$ (b) $R_a=0.2 \mu\text{m}$ (c) $R_a=0$.

According to Table 4 and Figure 26, for solid-water-air interface, a higher CA hysteresis is obtained when water droplet is deposited on the solid surface with a higher roughness factor. It is observed that for tilt angle equal to 9° , there is no change in CA difference for the samples with different surface roughnesses. For the tilt angle equal to 22° , CA difference depends on the surface roughness very slightly. For the tilt angle of 90° , the droplet remained attached to the solid due to the strong adhesion, so the measured hysteresis values (22° , 24° , and 26°) in this state were apparently lower than the maximum values which the surface could withstand.

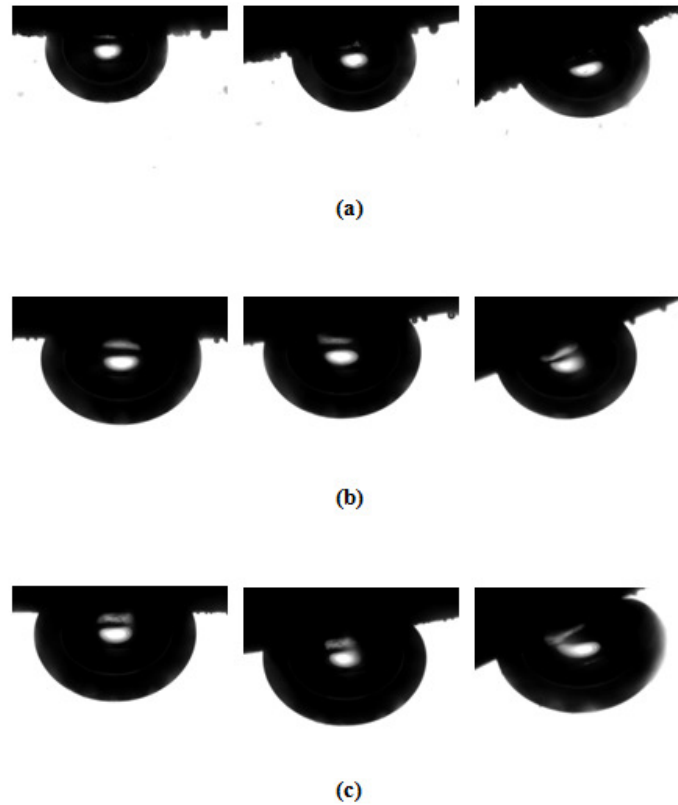


Figure 27. Advancing and receding CAs of air bubble on gray iron submerged in water for the three samples. (a) $R_a=0.1\mu\text{m}$. The angle between the surface and horizontal line is 0, 9, and 22 degrees from left to right, respectively. (b) $R_a=0.2\mu\text{m}$. The angle between the surface and horizontal line is 0, 9, and 27 degrees from left to right, respectively.

Results show that when samples are immersed in water, CA hysteresis depends on surface roughness for different tilt angles. For solid-water-air interface with air bubble placed on the solid surface, it is observed that CA hysteresis is greater for rougher surface. Also for larger tilt angle, CA hysteresis is greater.

Note that the measured hysteresis for the air bubbles was greater than that for water droplets, although the same solid-water-air interface was studied. Despite this, for the maximum tilt angles (sample 1: 22° , sample 2: 24° , sample 3: 27°) the bubble detached from the solid, whereas the water droplet remained attached to the solid even at the tilt angle of 90° (Table 4).

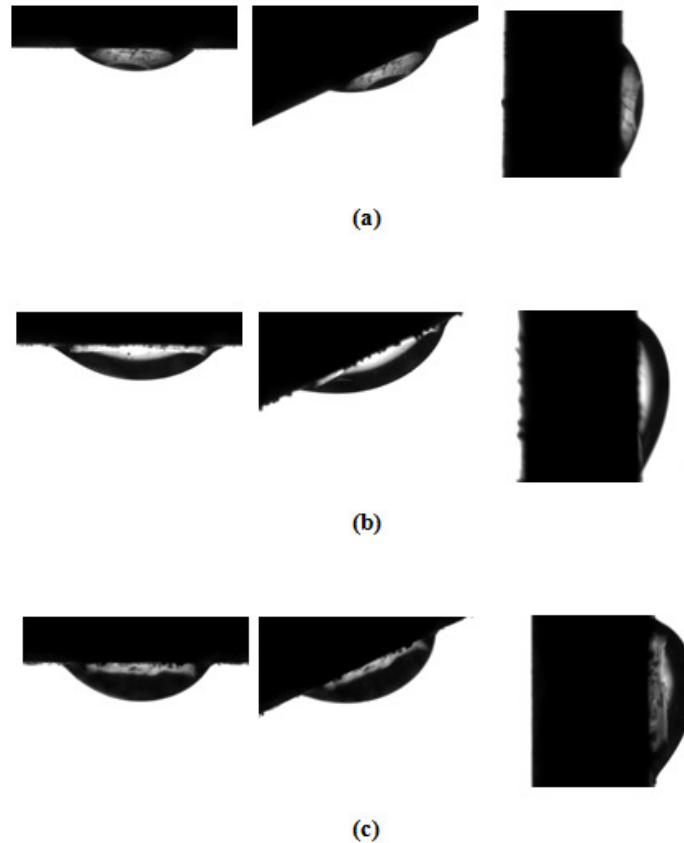


Figure 28. Advancing and receding CAs of oil droplet on gray iron submerged in water for three samples. The angle between the surface and horizontal line is 0, 25, and 90 degrees from left to right, respectively. (a) $R_a=0.1 \mu\text{m}$ (b) $R_a=0.2 \mu\text{m}$ (c) $R_a=0.3 \mu\text{m}$.

We attribute this to the fact that droplet-solid adhesion was stronger since the solid-water interface (2D contact area) component was present in addition to the triple line (1D) component, while air bubble did not have contact area adhesion. At the tilt angle of 90° , the measured values of CA hysteresis did not reach the maximum with the surface is capable to support. The static CA was also different (60° , 63° , and 68° for droplets vs. 98° , 99° , and 101° for bubbles, although the latter values were expected to be equal to 180° minus the former value). The reason for this effect requires further investigation.

2.7.4. Contact angle hysteresis discussion

According to CA hysteresis values obtained for solid-oil-water interface with oil droplet placed on the solid surface, the dependency of CA hysteresis on surface roughness is more considerable. It is observed that with using the sample with $R_a=0.1$, CA hysteresis is equal to 12° whereas with using the sample with $R_a=0.2$, CA hysteresis changes to 21° (Table 4).

Note that solid-water and solid-oil adhesion is quite different in its physical nature. Oil is a non-polar liquid and as Bormashenko (2010) showed recently, the main contributor to the surface tension is the London dispersion force. However, for water the situation is different since it has polar molecules capable of forming hydrogen bonds. For water in contact with air or with a non-polar solid or liquid, the Gibbs free surface energy $\Delta G = \Delta H - T\Delta S$ is a consequence of missing hydrogen bonds (yielding excess enthalpy ΔH) and the entropic “hydrophobic effect” (excess entropy ΔS times temperature T) due to the reorientation of the network of hydrogen bonds,. The entropic effect is several times stronger than the enthalpic one leading to the anomalously high surface tension of water $\gamma_{LV}=72$ mN/m (Israelachvili, 2011). The study of water droplets in air vs. air bubbles in water and vs. oil bubbles in water allowed us to separate these effects (Table 5). For a water droplet on a solid surface in air, missing hydrogen bonds and the reorientation of the network of hydrogen bonds contribute to the surface tension. The interactions at the solid-water interface are due to the London dispersion forces. For an air bubble the latter component is weak or absent, unlike in the case of an oil bubble.

Table 5. Forces contributing to the droplet/bubble adhesion to solid.

Interface	Forces near the triple line (1D)	Forces at the interface with solid (2D)	Adhesion to solid / hysteresis
Solid-water-air (droplet)	Hydrophobic (entropic) and missing H-bonds (enthalpic)	Hydrophobic (entropic) and missing H-bonds (enthalpic), dispersion force	Strongest
Solid-air-water (bubble)		No interaction	Weak
Solid-oil-water	Hydrophobic (entropic), missing H-bonds, and dispersion (enthalpic)	Dispersion forces (enthalpic)	Strong

2.8. Beyond Wenzel and Cassie-Baxter: second order effects

The Wenzel and Cassie-Baxter models are generally used in order to explicate the wetting properties of rough solid surfaces. According to the Wenzel model, liquid fills all roughness cavities and the wetting regime is homogeneous, whereas according to the Cassie-Baxter model, air pockets are trapped in cavities which leads to heterogeneous wetting regime. The Wenzel model states that roughening an intrinsically hydrophobic surface (i.e. contact angle $>90^\circ$) may result in superhydrophobicity with water contact angle (CA) exceeding 150° . The Cassie-Baxter model states that a combination of the trapped air pockets on the surface and surface roughening may lead to superhydrophobicity. Although these two models are widely used, wetting of rough surfaces is much more complex involving interactions at various scale levels, and the two classical models do not always give an accurate prediction of wetting properties of surfaces.

There are various effects such as contamination and heterogeneity, hierarchical roughness, grains, thin films, the disjoining pressure and so on, which occur at the mesoscale. The mesoscale is usually referred to distances on the scale of 10-100

nanometer. However in relative terms, it is defined as something in between the nanoscale and the microscale.

In order to determine the wetting regime in the three-phase system of solid, liquid and vapor, one has to consider the role of disjoining pressure and the formation of liquid thin film (mesoscale layer of the liquid) on the surface of the substrate. It was firstly discussed by Derjaguin (1940) that a liquid thin film, concave liquid meniscus and the bulk liquid may coexist in equilibrium condition (Figure 29a).

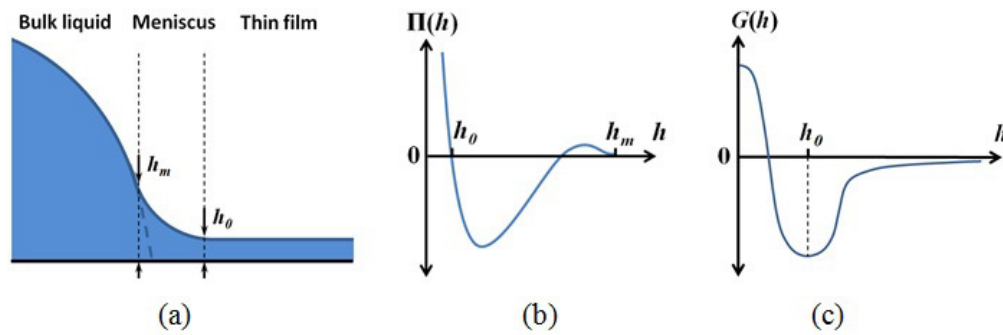


Figure 29. (a) Thin film in equilibrium with the bulk liquid of the droplet (b) Disjoining pressure versus the film thickness, h , (c) Energy profile of the liquid film

Derjaguin et al. (1987) defined the disjoining pressure of a liquid thin film as

$$\Pi(h) = -\frac{dG}{dh} \quad (2.26)$$

where $G(h)$ is the Gibbs free energy per unit area of the film and h is the thickness of the film. When the film is thick, $h > 100nm$, the energy of the system corresponds to the summation of solid-liquid (γ_{SL}) and liquid-vapor (γ_{LV}) interfacial energies. However, when $h \rightarrow 0$, the energy of the system only corresponds to the energy of the bare solid (γ_S). Considering these two cases, the energy per unit area can be obtained by (de Gennes et al. 2003)

$$\frac{Energy}{m^2} = \gamma_{SL} + \gamma_{LV} + G(h) \quad (2.27)$$

where $G(\infty) = 0$ and $G(0) = \gamma_S - \gamma_{SL} - \gamma_{LV}$.

The main parameter which characterizes the wetting of solid surface by liquid is the contact angle (CA). Derjaguin et al. (1987) derived the relation between the CA of a liquid droplet placed on a smooth solid surface, θ_0 , and the disjoining pressure as

$$\gamma_{LV} \cos \theta_0 = \gamma_{LV} + \Pi(h_0)h_0 + \int_{h_0}^{\infty} \Pi(h)dh \quad (2.28)$$

where h_0 is the thickness of the liquid film in equilibrium with the liquid meniscus (Figure 29) and $\Pi(h_0)$ is the disjoining pressure in the wetting film. Since the value of disjoining pressure may be positive or negative, the last two terms in the right hand side of equation (2.28) play key roles in determining the wetting regime. The negative or positive sign of the summation of these two terms corresponds to partial wetting or complete wetting regime, respectively (Boinovich and Emelyanenko, 2011). When there is no liquid film ($h=0$), the energy of the system is equal to the surface energy of the bare solid (γ_S). According to equation (2.26), the value of disjoining pressure terms in equation (2.28) should be equal to $G(0)$. Substituting the value of $G(0)$ from equation (2.27) into equation (2.28) yields the Young equation.

$$\cos \theta_0 = \frac{\gamma_S - \gamma_{SL}}{\gamma_{LV}} \quad (2.29)$$

Assuming h_0 as the film thickness in which the disjoining pressure goes to zero (Figure 29b), equation (2.28) can be simplified as

$$\cos \theta_0 = 1 + \frac{1}{\gamma_{LV}} \int_{h_0}^{\infty} \Pi(h)dh \quad (2.30)$$

From equation (2.30), It is realized that in order to attain the partial wetting on a smooth surface ($\theta_0 > 0$), the value of h should be between h_0 and h_m , otherwise the wetting is complete ($\theta_0 = 0$).

In practice, the surfaces are not perfectly smooth but involve the microsize protrusions which are covered by nanosize bumps or asperities (Figure 30). This multiscale structures cause the hierarchical roughness. The hierarchical roughness can

modify the wettability of the surfaces and result in superhydrophobicity. The Lotus leaf is the most popular superhydrophobic plant comprising the hierarchical roughness. There are microscale bumps called papillae on Lotus leaves which are covered by the nanoscale bumps with the scale of less than 100 nm. Here we present a model to theoretically study the wettability of the hierarchical roughened surfaces with the purpose to mimic a multiscale structure resembling the Lotus leaves. The effect of disjoining pressure on CA is also considered. In this model, the first order of roughness is considered to be a 2-dimensional structure with the microscale square pillars of height l_1 separated by distance l_1 (Figure 30a). It is assumed that the pillars are covered by the second order square pillars of the height l_2 and spacing l_2 (Figure 30b). Introducing $n=1,2,3, \dots$ as the order of roughness and k as the constant scale ratio, we have

$$\frac{l_1}{l_2} = \frac{l_2}{l_3} = \frac{l_3}{l_4} = \dots = \frac{l_{n-1}}{l_n} = k \quad (2.31)$$

where l_3 , l_4 , ..., and l_n are the pillar heights of the third, fourth, ..., and n th order of roughness (Figure 30c,d). The pillars with the order of roughness greater than 1 ($n > 1$) possess the nanoscale size and affect the surface wettability in a different way from the micro- and macroscale pillars. This is what we attribute it as the second order effect. To better understand how surface wettability is affected by the second-order effects, a theoretical model is presented in the following section.

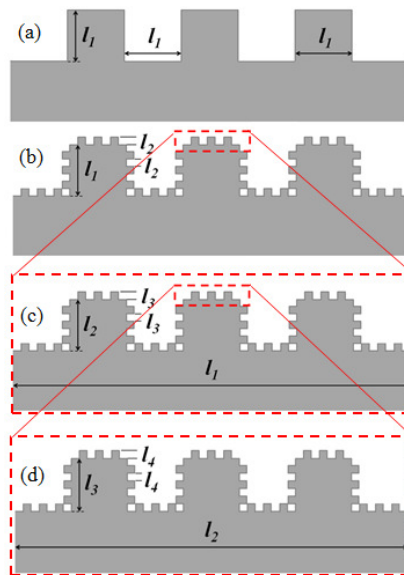


Figure 30. Multiscale roughness.

2.8.1. Modeling of wetting for a surface with hierarchical roughness

In this section we present a model to investigate the wettability of the rough surfaces with multiscale structures considering the effect of disjoining pressure and the liquid thin film at the interface. Let us consider a liquid droplet is deposited on the above hierarchical roughened surface. The droplet is in equilibrium with the liquid thin film with the thickness of h . Assuming $h_0 = l_1$, when $h > l_1$ liquid fills all the cavities between the pillars and the established wetting regime is Wenzel (Figure 31a). Therefore the liquid CA is given by

$$\cos \theta = R_f \cos \theta_0 \quad (2.32)$$

where the roughness factor $R_f \geq 1$ is the ratio of the real substrate area A_{SL} to the flat projected area A_F and $\cos \theta_0$ is obtained by equation (2.31). The roughness factor for the square pillars with the constant scale ratio k and with the structure shown in Figure 30 is given by

$$R_f = 2 \left(\frac{4N+1}{k} \right)^{n-1} \quad (2.33)$$

where N is the number of smaller scale pillars on every side of the larger scale pillar. Since for the first order of roughness, $n=1$, the value of R_f is equal to 2 and therefore $\cos \theta = 2 \cos \theta_0$ (Figure 31a). Assuming $l_1 = 2 \mu m$ and $N=3$, the values of $l_2, l_3, l_4, \dots, l_n$ can be obtained as $l_2 \approx 286 \text{ nm}$, $l_3 \approx 40 \text{ nm}$, $l_4 \approx 6 \text{ nm}$ and so on. For the first order of roughness, it is assumed that $h_m = 14 \mu m$. Therefore according to equation (2.30) and Figure 29b, the equation of disjoining pressure can be approximated as

$$\Pi(h) = (16.8 - 11h + 1.4h^2 - 0.05h^3) \quad (2.34)$$

where $2\mu m < h < 14\mu m$.

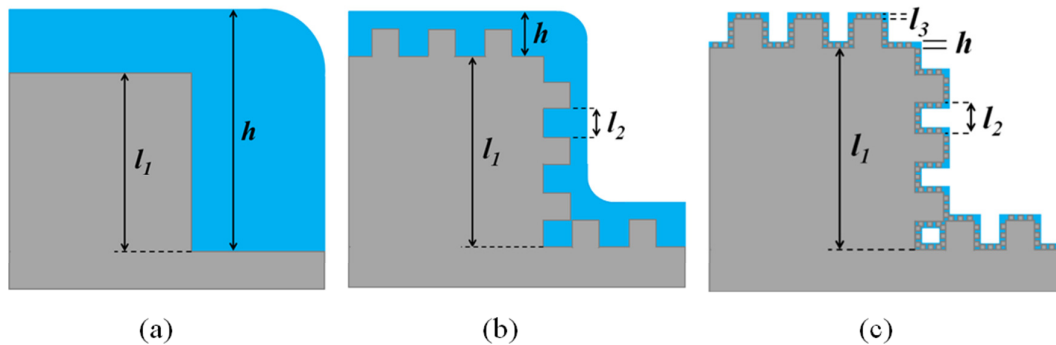


Figure 31. Wetting regimes.

For the pillars with the second order of roughness ($n=2$), assuming $h_0 = l_2$, when $l_2 < h < l_1$, liquid penetrates between the pillars and fill the smaller scale cavities with the height of l_2 . The established wetting regime for the pillars in this scale is Wenzel. However the wetting regime for the pillars with the first order of roughness is Cassie-Baxter due to the air pockets trapped in the larger scale cavities with the height of l_1 (Figure 31b). Therefore the CA is given by

$$\cos \theta = f_{SL} R_f \cos \theta_0 - (1 - f_{SL}) \quad (2.35)$$

where f_{SL} is the fraction of solid surface upon which the liquid sits. The value of f_{SL} for the pillars with the scales smaller than the first scale ($n>1$) can be approximated as

$$f_{SL} = \frac{1}{2} \left(\frac{N}{k} \right)^{n-2} \left(1 + \frac{2h}{l_{n-1}} \right) \quad (2.36)$$

Substituting equations (2.33) and (2.35) into equation (2.34) gives the liquid contact angle as

$$\cos \theta = \left(\frac{N}{k} \right)^{n-2} \left(1 + \frac{2h}{l_{n-1}} \right) \left(\frac{4N+1}{k} \right)^{n-1} \cos \theta_0 - \left(1 - \frac{1}{2} \left(\frac{N}{k} \right)^{n-2} \left(1 + \frac{2h}{l_{n-1}} \right) \right) \quad (2.37)$$

For the surface structure shown in Figure 30, $k=7$ and $N=3$. Substituting equation (2.30) into equation (2.33), and considering the effect of pillars with the second order of roughness ($n=2$), the liquid CA is given by

$$\cos \theta = \left(1 + \frac{2h}{l_1} \right) \left[\frac{13}{7} \left(1 + \frac{1}{\gamma_{LV}} \int_{h_0}^{\infty} \Pi(h) dh \right) + \frac{1}{2} \right] - 1 \quad (2.38)$$

According to equation (2.30) and considering $h_0 = l_2 = 286 \text{ nm}$ and $h_m = 2 \mu\text{m}$, the equation of disjoining pressure can be approximated as

$$\Pi(h) = 0.18 - 0.83h + 0.74h^2 - 0.185h^3 \quad (2.39)$$

where $286 \text{ nm} < h < 2 \mu\text{m}$.

For the pillars with the third order of roughness ($n=3$), when $l_3 = h_0 < h < l_2$, liquid penetrates between the pillars and fills the smaller scale cavities with the height of l_3 . The established wetting regime for the pillars in this scale is Wenzel. However the wetting regime for the pillars with the second order of roughness is Cassie-Baxter due to the air pockets trapped in the larger scale cavities with the height of l_2 (Figure 31c). Substituting equation (2.30) into equation (2.37), and considering the effect of pillars with the third order of roughness ($n=3$), the liquid CA is given by

$$\cos \theta = \left(\frac{3}{7} \right) \left(1 + \frac{2h}{l_2} \right) \left[\left(\frac{13}{7} \right)^2 \left(1 + \frac{1}{\gamma_{LV}} \int_{h_0}^{\infty} \Pi(h) dh \right) + \frac{1}{2} \right] - 1 \quad (2.40)$$

According to equation (2.30) and considering $h_0 = l_3 = 40 \text{ nm}$ and $h_m = 286 \text{ nm}$, the equation of disjoining pressure can be approximated as

$$\Pi(h) = 1.33 - 40.7h + 252.5h^2 - 442.5h^3 \quad (2.41)$$

where $40 \text{ nm} < h < 286 \text{ nm}$.

To approximate the CA of the liquid droplet considering the effect of pillars with the 4th, 5th, ..., and n th order of roughness, the value of n corresponding to that desired order should be substituted in equation (2.37). Figure 32 shows the liquid CA obtained from equations (2.32), (2.37) and (2.39) versus the liquid film thickness for first, second and third order of roughness.

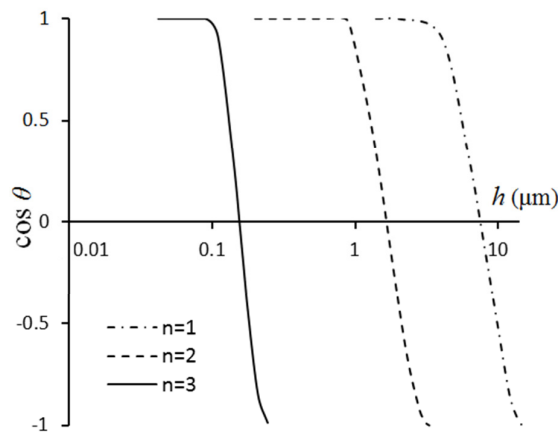


Figure 32. CA versus liquid film thickness, h .

As it is observed in Figure 32, the liquid CA increases differently on the pillars with the different order of roughness with increasing the liquid film thickness, h . The gaps between the CA curves indicate that for the specific values of liquid film thickness only those pillars with the order of roughness in the range of film thickness affect the surface wettability. Comparing the curves for the pillars with 1st, 2nd, and 3rd order of roughness shows the CA curve for the smallest scale pillars (3rd order of roughness) has steeper slope indicating their corresponding CA increases more quickly with increasing the film thickness, h . For the smaller scale of the pillars, the higher fraction of the surface is occupied by the air pockets which results in surface energy reduction and therefore CA increase. In addition, for the liquid film thickness greater than h_0 the disjoining pressure possess the negative sign. According to

equation (2.26), the negative disjoining pressure implies the net energy of the interface and therefore the CA are increasing. In the next section, wettability of the multiscale roughened surfaces is experimentally studied to investigate the distinct behavior of the substrates with different scales of roughness.

2.8.2. Experimental observation

To verify the models presented in the preceding section, and observe the influence of second-order effects on wettability, experiments are conducted for aluminum 6061 and stainless steel 304 samples roughened by etching and mechanical abrasion. Mechanical abrasion was used to create microscale roughness whereas chemical etching was applied to create nanoscale roughness because etchant can penetrate to the solid surface and make nanoscale pores which results in the nanoscale structures at the top of the microscale pillars. These two metals were used because while aluminum is lightweight, inexpensive, and easy to work, stainless steel is corrosion resistant, easy to clean, and has higher strength. First, samples were created and then the average roughness and liquid CA of them were measured.

2.8.2.1. Sample preparation

Aluminum and stainless steel samples were prepared by sectioning the 2 mm thick metal plates to the small square pieces of 2 cm × 2 cm size. Samples were then mounted using a phenolic mounting machine.

In order to achieve the desired surface roughness, sand papers with the grit size of 120, 240, 400, 600, 800, 1200 were applied. The grit size is a reference to the number of abrasive particles per inch of sandpaper. First, all samples were mechanically abraded using the sand papers from the roughest (Grit 120) to the softest (grit 1200) one at a time to get the glassy and smooth surfaces. Second, to obtain the

micro- and nanoscale orders of surface roughness magnitude, every 2 aluminum and stainless steel samples were roughened by one of the 6 grit size sand papers for 30 seconds employing the polishing machine. After that, the samples were polished with a soft cloth impregnated with 1 μm alumina. The scanning electron microscope (SEM) images of the polished samples ground with the sand papers with the grit sizes of 240 are shown in Figure 33.

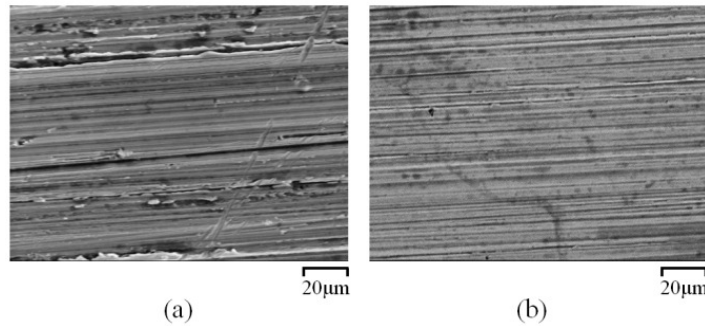


Figure 33. SEM image of the samples polished with the sand paper grit size 600 (a) aluminum (b) stainless steel.

To simulate the surface roughness induced by corrosive wear, acid etchants were produced. 5 ml of 96% concentrated sulfuric acid (H_2SO_4), 13 ml of 37% concentrated hydrochloric acid (HCl) and 7 ml of 70% concentrated nitric acid (HNO_3) were mixed to etch the aluminum samples. The solution was then diluted with 20 ml of water. For stainless steel samples etching, the previous solution with additional 5 ml of 96% concentrated sulfuric acid was prepared. The samples were scrubbed with a chlorine cleanser imbrued on a soft cloth. After that samples were rinsed with water and then dried in air.

The samples were placed in beakers embracing the specified acid solutions. 6 aluminum samples were preserved in the solution for 30, 60, 90, 120, 150 and 180 seconds, respectively. Stainless steel samples were kept in the solution for 1, 2.5, 4, 5.5, 7 and 8.5 minutes in order to achieve the approximately similar magnitude of roughness as aluminum samples. After that, samples were brought out of the

solutions, washed with water and dried in air. The SEM images of the aluminum and stainless steel samples etched for 60 seconds are shown in Figure 34.

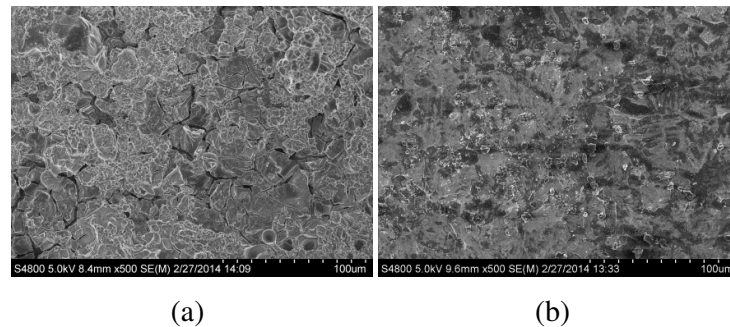


Figure 34. SEM image of etched samples (a) aluminum (b) stainless steel

2.8.2.2. Sample characterization

The surface roughness of the samples was measured before and after the etching and grinding processes using a surface roughness tester (Phase II+ SRG-4500). For each sample, the surface roughness was calculated by averaging the directional roughness measured on two perpendicular directions on the surface. The roughness parameter measured in the above cases is the average roughness value, R_a , defined as the arithmetic average of the absolute values of the roughness profile ordinates (Taha et al., 2010). The average roughness of aluminum and stainless steel samples was 1.1 and 0.14 μm before processing, respectively.

Water CAs were measured before and after etching and grinding. These measurements were done using the model 250 ramé-hart standard goniometer/tensiometer. 3 water droplets with 7 μl volume were located on different places of each sample surface and the final CA was calculated by averaging these three values. CAs of aluminum and stainless steel samples before processing was 69° and 67°, respectively. Figure 35 shows the contact angle profiles of aluminum and stainless steel samples before and after etching and grinding.

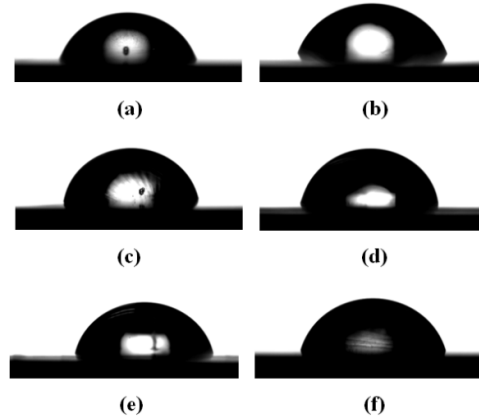


Figure 35. Water CA profile of (a) aluminum and (b) stainless steel samples before processing (c) aluminum and (d) stainless steel after grinding (grit size 400) (e) aluminum and (f) stainless steel after etching (120 seconds).

Figure 36 shows the water CAs of aluminum and stainless steel samples before and after etching and grinding. It is observed that the samples with the same magnitude of R_a but with the different methods of roughening have distinct contact angles. This reveals that besides the roughness and chemical heterogeneity of the surface, there are various other effects that influence the wetting properties of a surface. Here, we attribute this distinction to the second scale or hierarchical roughness of the surface.

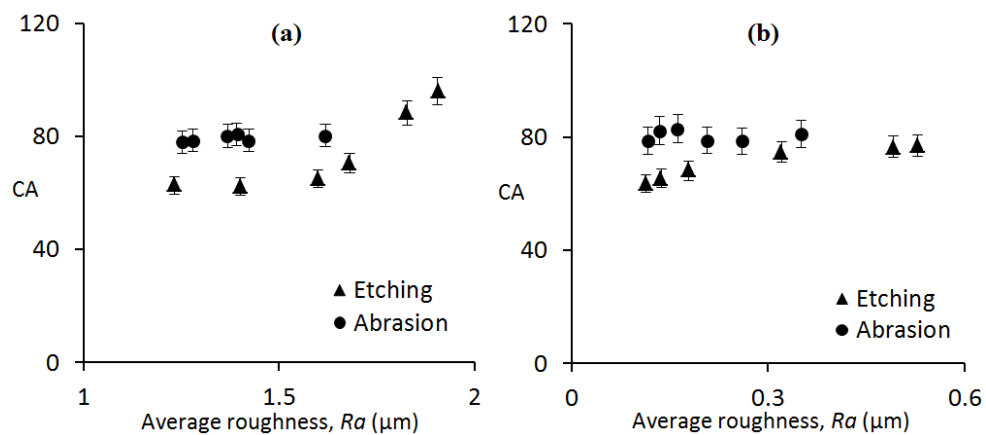


Figure 36. CA versus average roughness, R_a , (a) Aluminum samples (b) Stainless Steel samples.

2.8.3. Discussion

As it was explained before, the roughness value illustrated in Figure 36 is the average roughness measure by the surface roughness tester with the microscale range accuracy. However, according to Figure 37b, there are numerous nanoscale asperities at the top of the microscale ones which may affect the wetting properties. This nanoscale roughness plays the same role as the nanobumps do at the top of the microbumps in lotus leaf. The nanobumps are desirable because they prevent water from filling the cavities between the asperities by pinning the nanodroplets (Bhushan et al., 2009). Furthermore, nanoscale surface roughness underneath the water droplet increases the liquid-air fractional area, resulting in reduction in interfacial energy, adhesive force, and contact angle hysteresis. A combination of microscale and nanoscale roughness can help in resisting the air cavities between the asperities from filling with water, even in the case of a hydrophilic material. In particular, the mechanism of wetting transition from Cassie-Baxter to Wenzel regime is scale dependent. To effectively prevent this scale-dependent transition, and achieve the stable superhydrophobicity, it is expected that a hierarchical roughness is optimum (Nosonovsky and Bhushan, 2008).

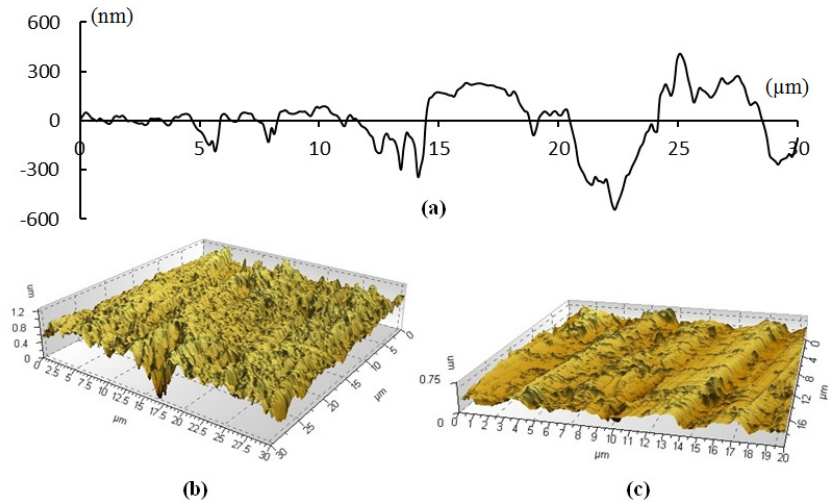


Figure 37. (a) 1D Roughness profile (b) 3D roughness profile of etched aluminum (c) 3D roughness profile of abraded aluminum.

To compare the experimental results with the model and determine the wetting property of the surface, the value of roughness factor, R_f , should be calculated. The roughness factor in equation (2.32), is defined as the ratio of the real surface area to the flat projected area. Figure 37a illustrates the roughness profile measured in one direction. On the basis of this figure, the roughness factor can be approximated by calculating the length of the profile, squaring the length value and dividing the result by flat projected area. As it is seen in Figure 37, the atomic force microscopy (AFM) is adjusted to draw the roughness profile for a $30\mu\text{m} \times 30\mu\text{m}$ and $20\mu\text{m} \times 20\mu\text{m}$ area. Therefore the flat projected areas are $900\mu\text{m}^2$ and $400\mu\text{m}^2$. It is noted that the R_f value calculated through the above-mentioned method is the real R_f . However, we need to find the R_f corresponding to only those asperities that significantly affect the wetting regimes.

Depending on the size and pattern of asperities, the liquid phase varies to different shapes such as droplet, channel, or thin film to minimize its energy. A thin liquid film with the thickness of the fraction of a nanometer to less than a micrometer can form at the surface. The surface energy of the film can be

determined by calculating the change in total energy when the surface area of the film varies by a small amount. Thus, the surface energy of the film is given by (De Gennes et al., 2004)

$$\gamma_h = \gamma_{SL} + \gamma_{LV} + G(h) + \Pi(h)h \quad (2.42)$$

The liquid film is stable when the curvature sketched in Figure 29c is positive ($\ddot{G}(h) > 0$), indicating the coexistence of a droplet with a liquid film of thickness h_0 . Should there be inadequate liquid supply to continuously retain the liquid film ($h < h_0$), the droplet will spread to supply the required liquid to cover the entire surface. Surface micro/nanostructure can change the impact of liquid film on wetting properties in an important way. For the nanoscale structures, the macroscopic laws are not valid anymore and the effects of intermolecular forces, capillary action, and disjoining pressure should be applied (Dietrich et al. 2005; Bonn et al., 2009). Micro/nanoscale asperities of the rough surface minimize the free energy of the interface by reducing the solid-liquid contact area which leads to an increased contact angle.

However, considering the role of disjoining pressure and the formation of liquid thin film on the substrate, indeed, a large number of nanoscale asperities covered by the liquid film do not directly affect the energy of the interface because they are already in Wenzel regime. However, those asperities with the height greater than the film thickness still have the potential to trap the air pockets resulting in the Cassie-Baxter regime. Therefore, only a small portion of nanoscale asperities in R_f affect the wetting regimes which are called the effective asperities. The roughness factor corresponding to the effective asperities is called effective roughness, R_{eff} . In order to verify the distinct values of contact angles for etched and abraded samples shown in Figure 36, one need to measure the exact

value of the R_{eff} for the samples. Since the surface is random to some extent, the exact surface topography is not known. Therefore, calculating the exact value of R_{eff} may be an incredibly difficult ploy. This makes the investigation of the wetting property of a rough surface a much more complex process, which cannot be simply predicted by the two classical models of Wenzel and Cassie-Baxter.

2.9. Conclusion

The standard method of creating a superhydrophobic surface implies roughening the surface and placing some low-energy (hydrophobic) material on it. Instead, we suggested here to place low-energy reinforcement into the matrix of the composite material. We presented a model for the overall contact angle of such a composite material and for the reinforcement volume fraction needed to make the material superhydrophobic. We also conducted an experiment with low-energy graphite-reinforced Al- and Cu-based composites and showed that the contact angle can be determined from the model with certain reasonable assumptions about the roughness factors and solid-liquid fractional contact areas. In order to decouple the effects of reinforcement and roughness, the experiments were conducted for initially smooth and etched matrix and composite materials. Our experiments did not show the superhydrophobicity, and the distinct difference between the wetting properties in composite materials and base alloys was found only in Cu-based samples. Furthermore, for these samples, we observed a decrease of the contact angle (hydrophilicity). However, Cu-based MMC data indicated that they are in the Cassie-Baxter wetting regime, which is required for superhydrophobicity. Therefore, we conclude that decoupling of the effects of roughness and composition is promising and shows that Cu-based MMCs have the potential to be used in the future to synthesize sustainable (wear-resistant) superhydrophobic surfaces.

CA hysteresis, measured as a difference between the advancing and receding CAs, is an important parameter characterizing wetting of a solid surface by a liquid. CA hysteresis exists not only in two-phase solid-water and three-phase solid-water-air systems, but also in solid-oil and solid-oil-water and solid-oil-water-air systems. The value of hysteresis depends on the interactions in the solid-liquid contact area and at the triple line. We studied CA hysteresis in two types of solid-water-air systems: with water droplets in air and air bubbles in water against the same metal samples. Although the solid-water-air triple line is the same in these two systems, the adhesion of water droplets was much stronger, which points to the role of the 2D interface. The hysteresis with the oil droplet was weaker than with air bubbles and water droplets, which indicates that weaker dispersion forces were involved in that system.

We also showed the wetting property of a rough surface is much complex and cannot be explicated only by two classical models of Wenzel and Cassie-Baxter. There are various other effects occurring at the mesoscale which influence the wetting properties of the surface.

CHAPTER THREE

3. CONCRETE

Concretes have various applications including architectural structures, walls, pavements, foundations, roads, bridges, dams, reservoirs, pools and even pipes and boats. Concretes are composite materials composed of paste and aggregates in their simplest form. The paste itself is a composition of a cement, commonly Portland cement, and water which coats the surface of fine and coarse aggregates. The aggregate is usually a coarse gravel or crushed rock such as limestone mixed with a fine aggregate such as sand. Through mixing dry composites with water, a chemical reaction called hydration will be occurred yields the paste hardens and gains strength to form a stone-like material called concrete.

Since the tensile strength of concretes is much lower than its compressive strength, therefore for making the structures, concrete is usually reinforced with materials which are strong in tension such as steel. A concrete mixture that does not have enough paste to fill all the voids between the aggregates will be difficult to place and will produce honeycombed surfaces and porous concrete. A mixture with an excess of cement paste will be easy to place and will produce a smooth surface; however, the resulting concrete is likely to shrink more and be uneconomical.

Concrete can be damaged by many processes. One of the most common reasons of concrete failure is freezing the water trapped inside the pores of concrete. To reduce damages caused by foregoing reason, it is important to design a proper concrete mixture having desired workability, high durability and strength and least possible porosity and voids at the same time.

Preparing water-repellent materials is an alternative way to make concretes which are more durable against damages caused by water. Using hydrophobic microparticles inside the bulk of the material is one way to produce sustainable water-repellent concretes. A reduction in size of particles to nanoscale can change the surface energy, surface chemistry and surface morphology of the materials yields in improving the basic properties and reactivity of the concrete's constituents.

In this chapter, wetting properties of concretes will be investigated and models will be proposed to predict contact angle of water droplet on concrete composites. In order to design novel superhydrophobic concretes, experiments will be conducted on different types of concretes and contact angle data will be collected for these samples.

3.1. Wetting of concrete

Fabrication of hydrophobic concrete is a very important task for many applications. Concrete, a mixture of portland cement as binder, and water as well as aggregates as fillers, is a porous material with pores ranging in size from nanometers to *millimeters*. There are various pore types within the cement hydration products, including entrapped and entrained air voids up to a few millimeters in diameter, capillary pores in a range of a few micrometers in diameter and nanoscale gel pores. In most applications concrete surface is subjected to external erosion, abrasion and environmental exposure to aggressive liquids, such as water, mineral solutions, oil, solvents, etc. When dry concrete comes into contact with a liquid such as water, most of the water is absorbed by the pores due to the capillary forces. The capillary forces are dependent on the surface tension of the liquid (typically water), its contact angle (CA) with the pore walls, and the radius of the pores (Stefanidou et al., 2013). The durability of concrete depends on its overall absorption and permeability, which are the two main parameters of interest. It is therefore crucial to synthesize water-

repellent concrete in order to increase its durability, and, in particular, to produce the ultradurable concrete (Sobolev et al., 2008).

The CA is the principal parameter which characterizes the wetting properties of the surface. When the CA is greater than 90° , it indicates the hydrophobicity, while the CA less than 90° shows the hydrophilicity, which is the tendency of a surface to become wet or to absorb water, as shown in Figure 38. Common concrete is hydrophilic. The superhydrophobicity corresponds to CA between 150° and 180° . The surfaces that are not quite superhydrophobic, but exhibit high CA between 120° and 150° , which is above typical values for hydrophobic materials, are called sometimes “overhydrophobic.” The water CA with a solid surface can be measured by goniometer or tensiometer. The CA of a water droplet on a smooth solid surface, θ_0 , can be calculated by using the Young equation

$$\cos \theta_0 = \frac{\gamma_{SA} - \gamma_{SW}}{\gamma_{WA}} \quad (3.1)$$

where γ_{SW} , γ_{SA} , and γ_{WA} are the solid-water, solid-air, and water-air interfacial energies, respectively.

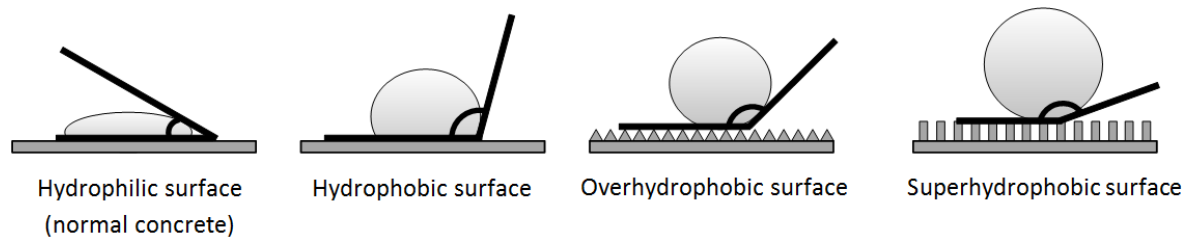


Figure 38. The hydrophilic ($0^\circ \leq \theta < 90^\circ$), hydrophobic ($90^\circ \leq \theta$), “over-hydrophobic” ($120^\circ \leq \theta < 150^\circ$) and superhydrophobic ($150^\circ \leq \theta \leq 180^\circ$) surfaces, where θ is the CA (Flores et al., 2013).

However, in practice, the surfaces are not quite smooth and usually possess micro- and nano-roughness. Two analytical models explaining the roughness effect on wetting properties of the surfaces were proposed by Wenzel (1936) and Cassie-Baxter

(1944). According to the Wenzel model, wetting is homogeneous because water fills all pores and cavities at the surface (Figure 39a). This model states that roughening a hydrophobic solid surface enhances its hydrophobicity by increasing the surface area:

$$\cos \theta = R_f \cos \theta_0 \quad (3.2)$$

where R_f is the roughness factor (the ratio of the real substrate area to its projected area) and θ is the CA on the rough surface. However, according to the Cassie-Baxter model, air can be trapped in cavities and the wetting is heterogeneous (Figure 39b). In other words, in Cassie-Baxter state, a composite interface of solid-water-air can be formed which increases the water repellency of the surface due to partial contact area of water droplet with air. The CA is given by:

$$\cos \theta = R_f f_{SW} \cos \theta_0 - (1 - f_{SW}) \quad (3.3)$$

where f_{SW} is the solid-water fractional area.

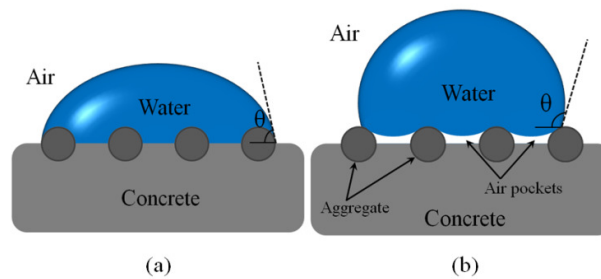


Figure 39. Schematics of water droplets on the rough surfaces: (a) Wenzel (b) Cassie-Baxter (Flores et al., 2013).

Superhydrophobic hierarchical surfaces with smaller size roughness patterns imposed over larger roughness patterns have generated interest due to their potential in industrial applications (mainly for self-cleaning). These surfaces mimic the Lotus leaf surface, which is notorious for its superhydrophobicity and self-cleaning properties, the so-called Lotus effect. Mimicking living nature for engineering applications is called “biomimetics,” and here we apply a biomimetic approach to synthesize hydrophobic concrete (Sobolev et al., 2005, 2007; Poole, 2007;

Nosonovsky, 2007b, 2011; Nosonovsky and Bhushan, 2009b; Nosonovsky et al., 2011; Hejazi et al., 2013).

To realize the superhydrophobicity on porous materials (i.e. ceramics, concrete, etc.) it was proposed to use the admixture based the hydrogen containing siloxane (e.g., polymethyl-hydrogen siloxane oil, PMHS) combined with small quantities of submicro- or nano-sized particles (Sobolev et al., 2007). A modified PEHSO/PMHS admixture releases hydrogen and forms small (10 μm - 100 μm), uniform air bubbles which are evenly distributed through the concrete volume (Figure 40). The distribution of the air bubbles through hardened concrete can be precisely tailored by preparing the water-based PEHSO emulsion with certain droplet size. Submicro- or nano-sized particles provide the micro/nanoroughness, which plays an important role in forming superhydrophobic surfaces through the hardened concrete and so improves the durability potential of concrete. The application of such emulsions for hydrophobization of concrete surfaces is a very effective solution to control the durability (Sobolev et al., 2013, and Muzensky, 2013). In the present paper we present a model and a systematic experimental study of various concretes prepared by the suggested methods.

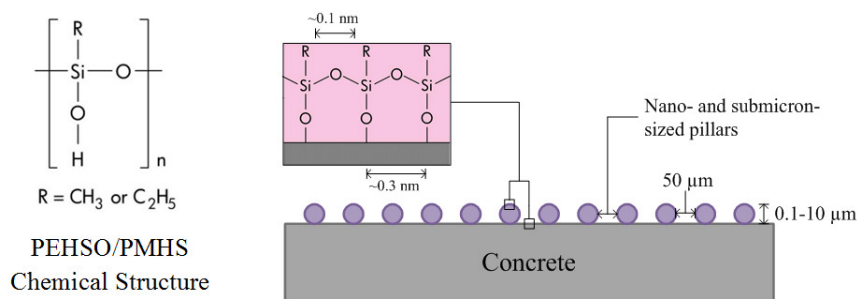


Figure 40. Schematics of the proposed hydrophobic concrete concept (Flores et al., 2013).

3.2. Modeling of superhydrophobic concrete

In this section, we develop a model which relates the CA of concrete with its composition and roughness. Suppose there is a concrete surface composed of the cementitious matrix and exposed fine aggregates (sand) with the fractional areas of f_c and f_a (so that $f_c + f_a = 1$), respectively. Assume the presence of sand at the interface causes roughness so that R_{f_c} and R_{f_a} are roughness factors of the cementitious matrix and sand. The water CA is then given by the Cassie equation as

$$\cos \theta = R_{f_a} f_a \cos \theta_a + R_{f_c} f_c \cos \theta_c \quad (3.4)$$

where θ_a and θ_c are the CAs for the coated inclusions and the cementitious matrix. If water forms partial contact with the solid (Cassie-Baxter) interface the CA is given by

$$\cos \theta = R_{f_a} f_a f_{AW} \cos \theta_a + R_{f_c} (1 - f_a) f_{CW} \cos \theta_c + f_a f_{AW} + (1 - f_a) f_{CW} - 1 \quad (3.5)$$

where f_{CW} and f_{AW} are the fractional contact areas of the cementitious matrix-water and aggregate-water, respectively.

Suppose the surface composed of the cementitious matrix and exposed aggregate inclusions (sand) is coated with the hydrophobic layer. In this case, the surface energies of the matrix and reinforcement have no impact on the CA because both are coated with the layer of hydrophobic material. To optimize the aggregate fraction required to reach the desired CA ($\theta = 180^\circ$), the following assumptions can be made: $\theta_a = \theta_c = 110^\circ$, $f_{AW} = 1$, $R_{f_a} = 2$ and $R_{f_c} = 1$ and, solving the equation for the aggregates fraction, yields:

$$f_a = \frac{-0.43 f_{CW}}{-0.15 - 0.43 f_{CW}} \quad (3.6)$$

Figure 41a shows the superhydrophobic area confined between the two lines corresponding to $\theta = 150^\circ$ and $\theta = 180^\circ$ obtained from equation (3.6). For any point in this area, the required aggregate fractional area, f_a , and the cementitious matrix-

water fractional area, f_{CW} , to achieve hydrophobic and superhydrophobicity can be calculated. Figure 41b illustrates the CA versus aggregate fractional area for various values of the fractional cementitious matrix-water contact area obtained from equation (3.5). The figure shows that the CA increases with increasing the aggregate fractional area as attributed to the Cassie-Baxter state.

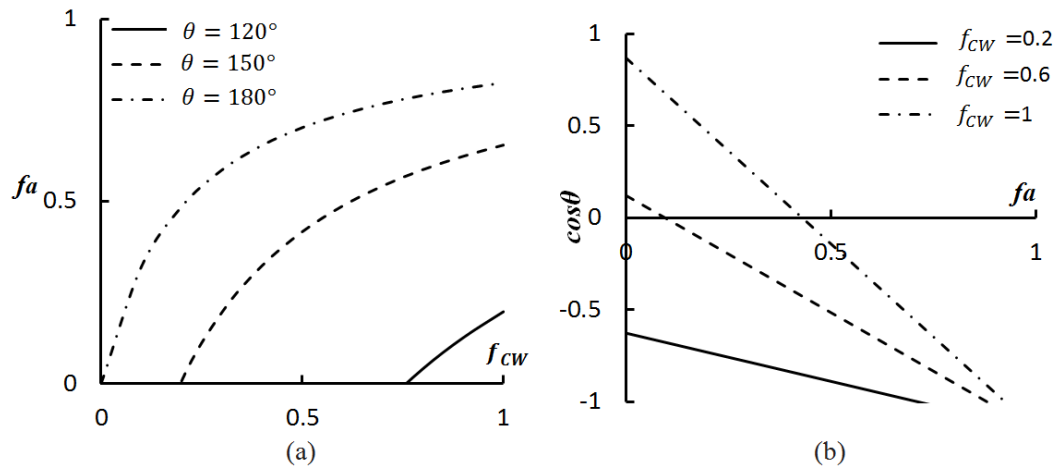


Figure 41. (a) Aggregate fractional area, f_a versus the cementitious matrix fractional area, f_{CW} (b) CA versus aggregate fractional area, f_a for various values of fractional the cementitious matrix -water contact area, f_{CW} (Flores et al., 2013).

Suppose the distribution of the aggregates at the surface has the pattern shown in Figure 42a. Assuming the uniform diameter, D , for the aggregates and the equal distance, L , between every two adjacent aggregates, f_a can be calculated as

$$f_a = \frac{\pi H}{L^2} (D - H) \quad (3.7)$$

where H is the projection height of the aggregates out of the surface.

The aggregate roughness factor, R_{fa} can be then calculated as

$$R_{fa} \approx 1 + \frac{\pi H}{L^2} (D - H) \quad (3.8)$$

Assuming $f_{AW} = \frac{2}{3} f_a$ and $f_{CW} = \frac{1}{2} f_c = \frac{1}{2} (1 - f_a)$, and then substituting equations (3.7) and (3.8) into equation (3.5) yields

$$\cos \theta = \left(\frac{2\pi^2 H^2 L^2 (D-H)^2 + 2\pi^3 H^3 (D-H)^3}{3L^6} \right) \cos \theta_a - \frac{(L^2 - \pi H D + \pi H^2)^2}{2L^4} R_{fc} \cos \theta_c + \frac{7\pi^2 H^2 (D-H)^2 - 6\pi H L^2 (D-H)}{6L^4} - \frac{1}{2} \quad (3.9)$$

Figure 42b and c show that there is an optimal distance between the aggregates where the CA has its highest value. It is also observed that for the distances greater than the optimal distance with increasing the projection height of the aggregates, H , the CA increases. However, for the distances smaller than the optimal distance when H increases, the CA decreases. The increase in CA with increasing the concrete roughness factor, R_{fc} is considerable.

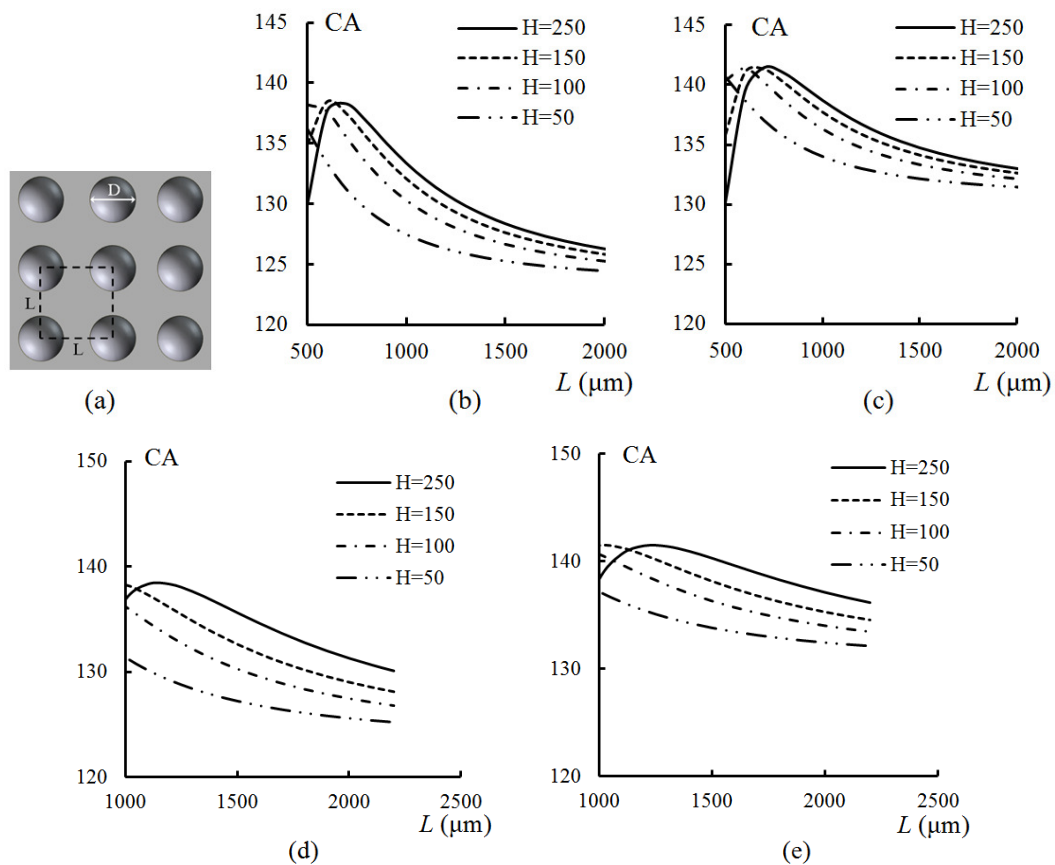


Figure 42. (a) Schematics of the aggregate patterns at the interface. (b, c, d, e) CA versus distance between the aggregates, L , for $\theta_a = \theta_c \approx 95^\circ$ and (b) $D=500 \mu\text{m}$, $R_{fc}=1$ (c) $D=500 \mu\text{m}$, $R_{fc}=3$ (d) $D=1000 \mu\text{m}$, $R_{fc}=1$ (e) $D=1000 \mu\text{m}$, $R_{fc}=3$ (Flores et al., 2013).

Comparing Figure 42b, c and Figure 42d, e reveals that the aggregate size affects the CA for only the shorter distances between the aggregates ($L \leq 1.5D$), while for the longer distances ($L > 1.5D$), the aggregate size does not have significant influence on the CA. Accordingly, the model facilitates design of the concrete samples in terms of aggregates contribution to achieve the higher CA as described in the following sections. Materials preparation and experimental procedure are explained in the appendix.

To understand the effect of droplet size in the emulsion on the irregularities of hydrophobic surface coating, the maximum and minimum diameters of droplet size and intact or collapsed bubbles were determined. Emulsion droplets and intact or collapsed bubbles were considered of spherical shape. The effect of the droplet size of the emulsion on surface irregularities is demonstrated in Figure 43. As a general trend, the bigger the droplet size is, the bigger the diameter of the bubble. Collapsed surface structure (Mk1-Simple) requires a small increment on the droplet size in order to increase the irregularities on the surface. From this analysis, to produce small “moon craters” a higher speed during the emulsion production is required,. Bigger intact bubbles (Mk3-Core) can be realized when the emulsion droplet size is large ($>30 \mu\text{m}$). However, intact bubble structure is difficult to realize since the larger droplets result in unstable emulsions. Here, the addition of particles increase the stability of emulsions and reinforce the bubbles.

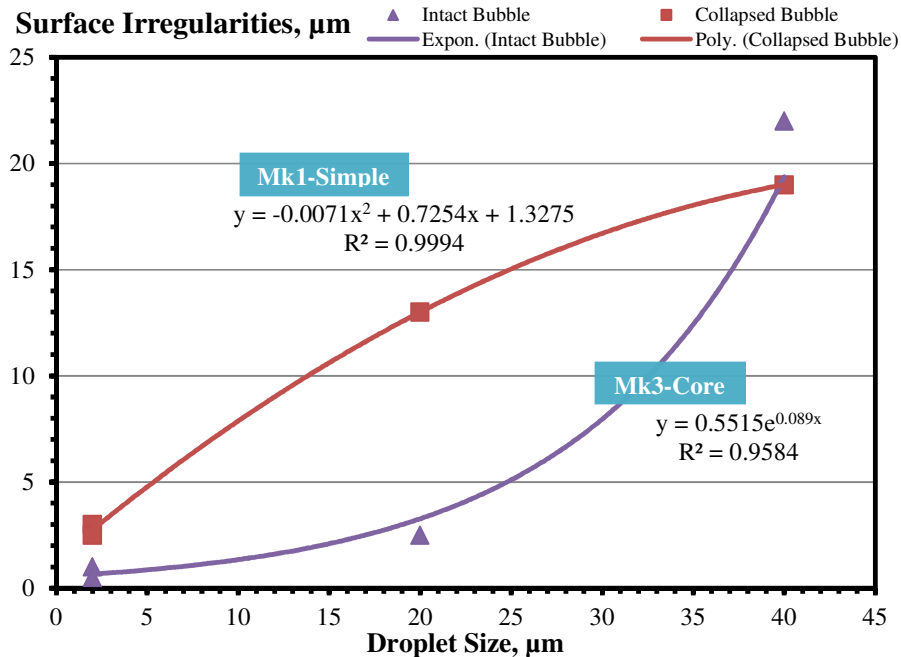


Figure 43. The effect of the droplet size of the emulsion on the irregularity of the coatings (Flores et al., 2013).

3.2.1. Contact angle measurement

The wetting properties of the tiles were examined by measuring the water CA using the Ramé-Hart Goniometer model 250. At least three, $5\mu\text{l}$ water droplets were placed at different points on each sample. The values of water CAs are shown in Figure 44. It was found that the CAs of all coated specimens increased by more than 120% vs. the reference material. The application of a second coating did not improve the performance of Mk1 and Mk3. Apparently, the hydrophobic first coat of Mk1 and Mk3 did not allow for the settlement of the second coat. A remarkable performance of self-assembled Mk2 was observed, not only on single-coated specimens (with CA of 3 times better vs. the reference), but also for double-coated specimens (CA of 4 times the reference). Metakaolin particles, located at the boundaries of the droplets, acted as support for the second coating, providing the surface a micro-roughness and

increasing the hydrophobicity. The images of water droplets on different hydrophobic coatings are shown in Figure 44.

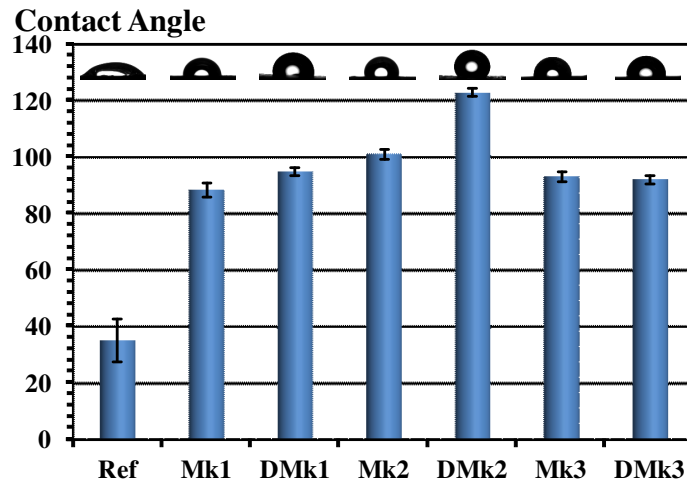


Figure 44. The contact angle of specimens with single (Mk)- and double (DMk)-coatings (Flores et al., 2013).

3.2.2. Contribution of hierarchical roughness

To calculate the water CA on the surface of the concrete with dual scale or hierarchical roughness, induced by micron-sized bubbles or MK particles, the smaller scale roughness needs to be considered in proposed models. Introducing the R_{fs} as the second order roughness induced by cellular structure or particles on the surface (Figure 45), CA can be calculated as

$$\cos \theta = \frac{2\pi^2 H^2}{3L^4} (D - H)^2 (R_{fa} + R_{fs}) \cos \theta_a + \frac{(L^2 - \pi H(D - H))^2}{2L^4} (R_{fc} + \frac{L}{D} R_{fs}) \cos \theta_c + \frac{7\pi^2 H^2 (D - H)^2 - 6\pi H L^2 (D - H)}{6L^4} - \frac{1}{2} \quad (3.10)$$

According to Figure 42a, the value of R_{fs} for the aggregates with $D=500 \mu\text{m}$ can be assumed as

$$R_{fs} = \frac{n\pi d^2}{L^2} \quad (3.11)$$

where n is the number of bubbles in $D=500 \mu\text{m}$ (Figure 45) and d is the diameter of the bubbles or particles (protrusions) on the surface.

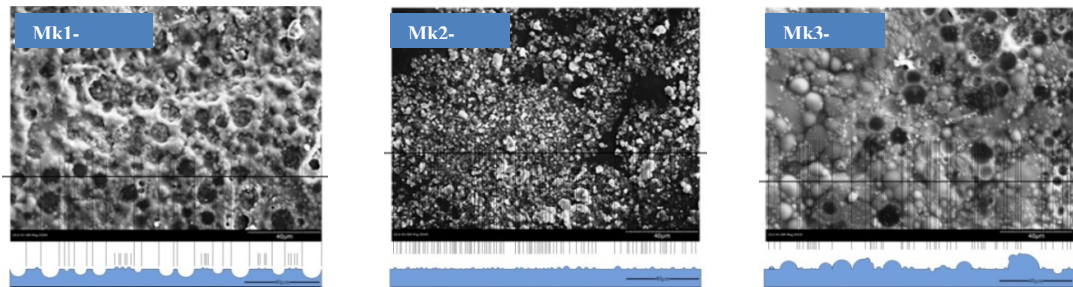


Figure 45. The profile of surfaces of mortar specimens: (a) Collapsed cellular structure, (b) particle coating, (c) bubbles on the surface (Flores et al., 2013).

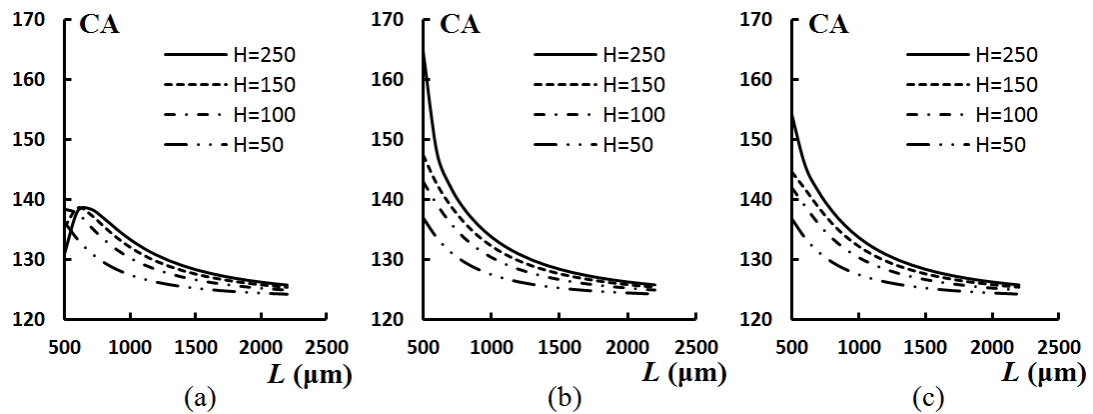


Figure 46. CA versus distance of the aggregates, L , for $D=500 \mu\text{m}$, $R_{fc}=1$ and $\theta_a = \theta_c \approx 95^\circ$ (a) $n=30$ and $d=2 \mu\text{m}$ (Mk1) (b) $n=100$ and $d=5 \mu\text{m}$ (Mk2) (c) $n=20$ and $d=10 \mu\text{m}$ (Mk3) (Flores et al., 2013).

Figure 46 shows the water CA versus L for the aggregates with $D=500 \mu\text{m}$. According to Figure 45, it is assumed that $n=30$ and $d=2 \mu\text{m}$ for collapsed cellular structure sample (Mk1), $n=100$ and $d=5 \mu\text{m}$ for particulate self-assembled coating (Mk2) and $n=20$ and $d=10 \mu\text{m}$ for bubble coated sample (Mk3). It is observed that the CAs of Mk2 coated samples are higher than those of Mk1 and Mk3 samples. It occurs due to the higher number of micron-sized particles present at the surface of Mk2 coated samples comparing to cellular and bubble coatings. It is also observed that with increasing the projection height of the aggregates, H , the CA increases.

3.3. Conclusion

The technology of hydrophobic emulsions and their application on portland cement mortar tiles were investigated. A theoretical model was developed and a relationship between the droplet size and the size of irregularities on the surface of coating were established to optimize the design of the emulsions. The models for coated and non-coated concrete that can be generalized for other types of materials were developed. An optimal distance between the aggregates where the CA has the highest value was predicted based on proposal models. The effect of dual scale roughness of concrete surface on CA was theoretically investigated. The introduction of hierarchical roughness and chemical modification of the surface can be beneficial for the design of bioinspired superhydrophobic concretes.

The proposed emulsion types were successfully realized by using different mixing procedures. Wetting of mortar tile surfaces by water was investigated experimentally. Samples coated with the MK2 solution showed the highest water-repellency due to its microroughness and hydrophobization.

In summary, we reported a method to produce over-hydrophobic water-repellent concrete with water CAs approaching the superhydrophobicity values. Water-repellent concrete can have numerous applications in construction and civil engineering due to its enhanced durability.

CHAPTER FOUR

4. Oleophobicity

4.1. Oleophobic/philic surfaces and types of oleophobicity

When a surface repels oils or organic liquids, it is called oleophobic, which implies that the CA with oil is greater than 90° . Surfaces that are both hydrophobic and oleophobic are called

omniphobic. Although the term oleophobicity usually applies to a three phase solid-oil-air interface, it is also relevant to a three-phase solid-oil-water interface (referred to as underwater oleophobicity). The oleophobic surfaces are of interest in many applications where self-cleaning is desirable, such as windows, kitchen appliances, windshields, and optical applications including lens, sunglasses, LCDs, and plasma displays. Underwater oleophobicity is desirable for such applications, as submarines and ship hulls, water industry components (such as pipes, water meters, and heaters), medical catheters and similar devices (Genzer and Efimenko, 2006; Nosonovsky and Bhushan, 2009a). In these applications, organic contaminants along with microorganisms (bacteria and algae) can accumulate, resulting in undesirable biofouling. The use of self-cleaning oleophobic surfaces can reduce biofouling (Nosonovsky and Bhushan, 2008h).

Since most organic liquids are nonpolar, and, therefore, their surface tension is lower than that of water consisting of polar H_2O molecules, it is much more difficult to make a surface with organic liquids repelling capability by applying low surface energy coatings. The three-phase solid-oil-air interface is usually unstable with air pockets pushed away by oil. However, properly designed surface roughness can stabilize the three-phase

interface (Nosonovsky and Bhushan, 2007c). Tuteja et al. (2007) showed that re-entrant surface curvature, in conjunction with chemical composition and roughened texture, can be used to design surfaces that display extreme resistance to wetting from a number of liquids with low surface tension, including alkanes such as decane and octane. Liu et al. (2009) suggested that oleophilic surfaces in the air can turn into oleophobic surfaces when immersed in water, forming a stable three-phase (solid-water-oil interface). Most hydrophobic/oleophobic surfaces are prepared by employing a surface microstructure, for example, a periodic array of pillars ranging in size from several micrometers to dozens of micrometers. Hierarchical structures, with nanoroughness imposed on the microstructure, are used as well. However, microstructured hydrophobic/oleophobic surfaces have a huge limitation in their application. They are extremely vulnerable to even moderate rates of wear and deterioration in aggressive underwater and other environments. To design more durable hydrophobic and oleophobic surfaces, we suggested earlier using metal matrix composites (MMCs) introducing hydrophobic reinforcement into the bulk of the material, rather than at its surface (Nosonovsky et al., 2011). Such a method provides the micropatterned surface roughness and heterogeneity needed for oleophobicity. When wear, corrosion, or erosion cause a surface layer to become deteriorated or removed, due to the presence of oleophobic reinforcements making roughness at the surface, the surface still remains oleophobic. A different trend in the development of sustainable superhydrophobic/oleophobic surfaces involves combining self-healing, self-lubricating, and self-cleaning abilities (Nosonovsky, 2011). These three are features of novel materials with an embedded capacity for self-organization.

The thermodynamic theory of self-organization was developed decades ago by Nobel Prize winner Prigogine (Nicolis and Prigogine, 1977). However, only now has it become clear that this theory can be applied to novel materials. Friction and wear, which are usually viewed as causes of energy dissipation and material deterioration, can, under certain circumstances, lead to increased orderliness at the interface. When a mechanism providing such an ability is embedded into the material, self-lubrication, self-healing, or self-cleaning can occur (Nosonovsky and Rohatgi, 2011; Mortazavi and Nosonovsky, 2011). As mentioned before two standard models explaining superhydrophobicity are the Wenzel model (Wenzel, 1936) of the two-phase solid-water interface (Figure 47a) and the Cassie-Baxter model (Cassie and Baxter, 1944) of the three-phase solid-water-air interface (Figure 47b). The wetting of rough surfaces can be more complex than what these two basic models predict. In particular, multiphase interfaces involving solid, oil, water, air, lubricant, etc. are promising for new applications including self-lubricating, self-healing, and antifouling materials (Figure 47c shows an oil droplet in water in contact with a rough surface; since oil is lighter than water, it approaches the surface from the bottom). Thus, Wong et al. (2011) used a porous sponge-like material infused with a lubricating liquid, which they called slippery liquid infused porous surfaces (SLIPS). As a result, a composite solid-lubricant-liquid interface is formed, where liquid can be either water or oil, and lubricant plays the same function as air in the Lotus effect solid-water-air interface (Figure 47d).

A properly selected lubricant should be immiscible with both polar and nonpolar liquids. One class of such liquids is the fluorocarbons or perfluorinated liquids, consisting of F and C atoms. Using such liquids demonstrated very promising omniphobic properties.

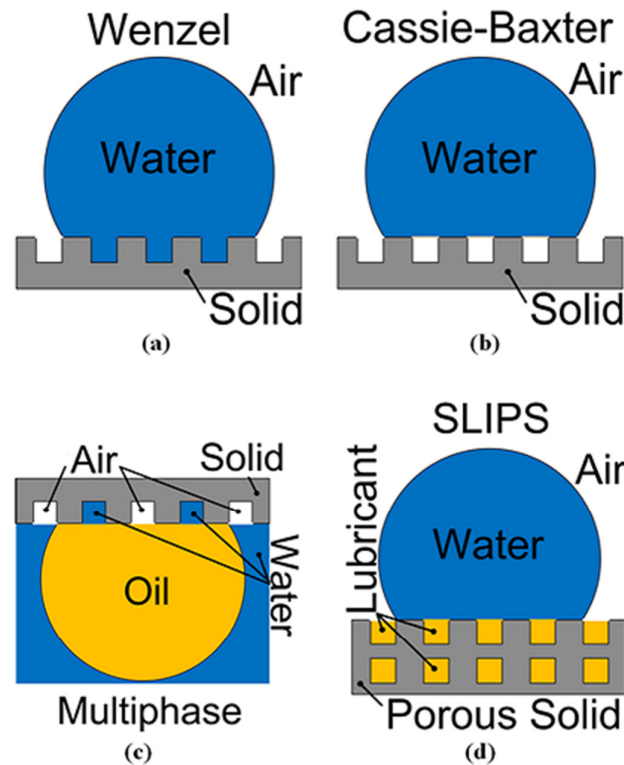


Figure 47. Water droplet on a microstructured surface forming (a) Wenzel (two-phase solid-water) (b) Cassie-Baxter (three-phase solid-water-air) (d) oil droplet (immersed in water) on four-phase solid-oil-water-air interface (d) slippery lubricant-infused porous.

Many researchers have studied the so-called Cassie-Wenzel transition from the three-phase solid-liquid-air to the two-phase solid-liquid interface (Nosonovsky and Bhushan, 2008d; Bormashenko et al., 2007; Wang et al., 2005). However, there has been no significant effort so far to investigate the wetting transition of three-phase or four-phase interfaces of solid-oil-water or solid-oil-water-air for an underwater system. In this section we model two-, three-, and four-phase interface of underwater oleophobic surfaces and discuss the wetting transition and interfacial energy for a four-phase interface system. In the following section, a model for the CA for multiphase systems is presented. After that, a phase field model formulation is suggested to describe these wetting transitions. These models can be used to study

wetting transitions in underwater oleophobic systems, which were investigated experimentally and are discussed in consequent sections.

4.1.1. Modeling of underwater oleophobicity

In this section, we describe our modeling of wetting properties of the multiphase interfaces. Depending on the physical properties of a particular system, including surface roughness and interfacial energies, two-, three-, or four-phase interface can form.

4.1.1.1. Two-phase interface of solid oil (Wenzel regime)

If an oil droplet is placed on a solid surface immersed in water, the CA of an oil droplet in water, θ_{OW} , is given by Young's equation (Figure 48)

$$\cos \theta_{OW} = \frac{\gamma_{SW} - \gamma_{SO}}{\gamma_{OW}} \quad (4.1)$$

Similarly, the CAs of oil and water with the solid surface in the air are given by

$$\cos \theta_{SW} = \frac{\gamma_{SA} - \gamma_{SW}}{\gamma_{WA}} \quad (4.2)$$

$$\cos \theta_{SO} = \frac{\gamma_{SA} - \gamma_{SO}}{\gamma_{OA}} \quad (4.3)$$

where, γ_{SO} , γ_{SA} , γ_{SW} , γ_{OA} , γ_{WA} and γ_{OW} are free energies for solid-oil, solid-air, solid-water, oil-air, water-air, and oil-water interfaces (Jung and Bhushan, 2009b).

Substituting γ_{SW} , γ_{SO} from equations (4.2) and (4.3) into equation (4.1) yields

$$\cos \theta_{OW} = \frac{\gamma_{OA} \cos \theta_{SO} - \gamma_{WA} \cos \theta_{SW}}{\gamma_{OW}} \quad (4.4)$$

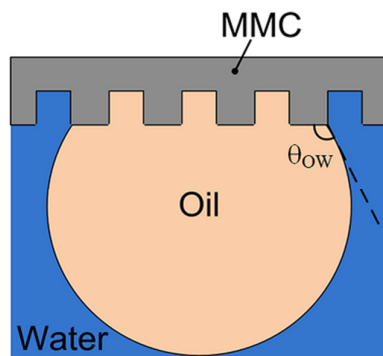


Figure 48. Wetting of a microstructured surface in the homogeneous (Wenzel, solid-oil) regime.

Note that there are no limitations on the values of the interfacial energies, however, certain conclusions about their relationships can be made. At ambient conditions, $\gamma_{WA} = 0.072 \text{ Jm}^{-2}$. Surface tensions of organic liquids are much lower, usually in the range $0.01 < \gamma_{OA} < 0.03 \text{ Jm}^{-2}$. Typical values of water CA for most solids are $\theta_w < 90^\circ$ and therefore, from equation (4.2), $\gamma_{SA} > \gamma_{SW}$ (hydrophobic materials, such as wax or Teflon are an exception with $\gamma_{SA} < \gamma_{SW}$) and $\gamma_{SA} - \gamma_{SW} < \gamma_{WA}$. Similarly, from equation (4.3), $\gamma_{SA} > \gamma_{SO}$ and $\gamma_{SA} - \gamma_{SO} < \gamma_{OA}$. Oils tend to form a film (or a pancake-like bubble) on water surface, so another approximate equality can be added, $\gamma_{WA} - \gamma_{OW} \approx \gamma_{OA}$.

The interfacial energies can be treated as “surface tension” forces. Usually, only the balance of horizontal components of the surface tension forces acting upon the three-phase line is taken into account, whereas it is assumed that the vertical component is balanced by the reaction force of the solid surface. The balance leads to the Young equation (equations (4.1)-(4.3)) (Figure 49a). In a more general case, the surface tensions can be treated as vectors of forces acting upon the triple line. Note that when a liquid droplet is placed on a solid surface, the difference in chemical potentials leads to molecular reorientation in the solid surface (including its partial dissolution or deformation), so that a “bed” is formed under the droplet, giving rise to

a vertical component of the solid-liquid tension in the state of thermodynamic equilibrium. However, for most solid surfaces, this molecular reorientation is insignificant and thermodynamic equilibrium is not achieved, so the vertical component is balanced by the reaction force R . So, we will distinguish between the true surface tensions of the γ_{SOt} and γ_{SWt} , and their projections on the nondeformable solid surface.

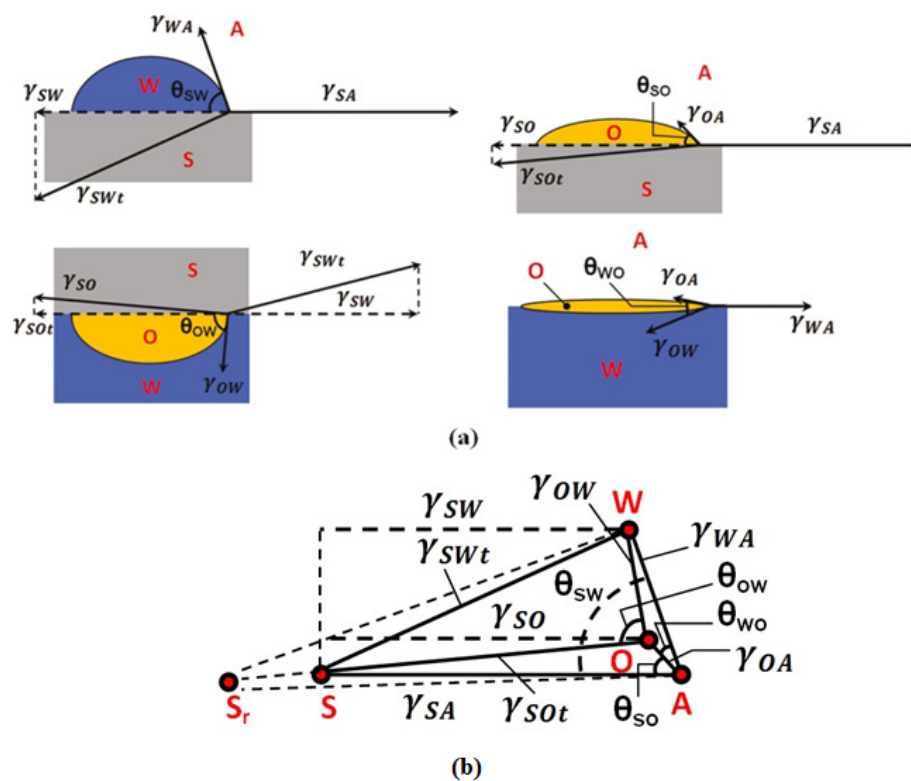


Figure 49. Schematics showing CAs and interfacial energies (a) in four different systems (solid-water-air, solid-oil-air, solid-oil-water, and oil-water-air) (b) together form a tetrahedron.

For surface tensions treated as vectors, equations (4.1)-(4.3) have an interesting geometrical interpretation. Each of the four equations constitutes a triangle whereas all four form a tetrahedron, as shown in Figure 49b; the angles between the vectors are the CAs.

For a rough surface, the CA, θ , is given by the Wenzel equation (Wenzel, 1936)

$$\cos \theta = R_f \cos \theta_0 \quad (4.5)$$

where θ_0 is the contact angle of droplet with the smooth surface and $R_f \geq 1$ is the roughness factor defined as a ratio of the surface area to its flat projection. Geometrically this can be interpreted as an effective increase of the components γ_{SO_t} , γ_{SW_t} , and γ_{SA_t} proportionally to R_f , which corresponds to the point S_r in Figure 49b. Combining equations (4.4) and (4.5), the equation for the CA of an oil droplet underwater is given by

$$\cos \theta_{OW} = \frac{\gamma_{OA} \cos \theta_{SO} - \gamma_{WA} \cos \theta_{SW}}{\gamma_{OW}} R_f \quad (4.6)$$

We observe from equations (4.4)-(4.6) that hydrophobicity and underwater oleophobicity are two closely related phenomena. As a consequence, a superhydrophobic surface can become oleophobic when immersed in water, under certain circumstances, which are summarized in on the basis of (Jung and Bhushan, 2009).

Table 6. Oleophobic and oleophilic interfaces.

Interface	Hydrophobic $\gamma_{SA} < \gamma_{SW}$		Hydrophilic $\gamma_{SA} > \gamma_{SW}$		
solid-water-air	Hydrophobic $\gamma_{SA} < \gamma_{SW}$		Hydrophilic $\gamma_{SA} > \gamma_{SW}$		
solid-oil-air	Oleophilic if $\gamma_{SA} > \gamma_{SO}$	Oleophobic if $\gamma_{SA} < \gamma_{SO}$	Oleophilic if $\gamma_{SA} > \gamma_{SO}$	Oleophobic if $\gamma_{SA} < \gamma_{SO}$	
solid-oil-water	oleophilic	Oleophilic if $\gamma_{OA} \cos \theta_{SO} < \gamma_{WA} \cos \theta_{SW}$	Oleophobic if $\gamma_{OA} \cos \theta_{SO} > \gamma_{WA} \cos \theta_{SW}$	Oleophilic if $\gamma_{OA} \cos \theta_{SO} > \gamma_{WA} \cos \theta_{SW}$	Oleophobic if $\gamma_{OA} \cos \theta_{SO} < \gamma_{WA} \cos \theta_{SW}$

4.1.1.2. Three-phase interface of solid-oil-water (Cassie-Baxter regime)

When air pockets are trapped at the interface between the solid surface and water, corresponding composite three-phase interface can form, which is usually referred to as the Cassie-Baxter state. In a similar manner, if an oil droplet is placed on a solid surface under water so that water bubbles are trapped between oil and the solid surface, the three-phase solid-oil-water interface can form (Figure 50).

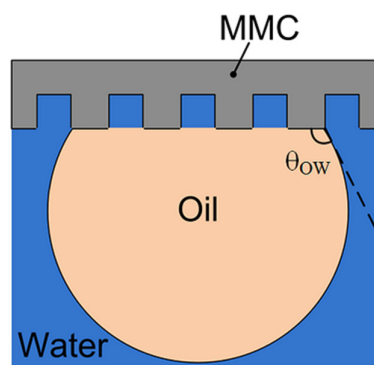


Figure 50. Wetting of a microstructured surface in the composite (Cassie-Baxter, solid-oil-water) regime.

According to the Cassie equation, the contact angle of a liquid droplet with a surface composed of two fractions, one with a fractional area f_1 and the CA, θ_1 , and the other with $f_2=1-f_1$ and θ_2 , respectively was given by Cassie (1944)

$$\cos \theta = f_1 \cos \theta_1 + f_2 \cos \theta_2 \quad (4.7)$$

When water droplet comes in contact with the composite interface, fraction 1 is the solid ($\theta_1 = \theta_w$) and fraction 2 is air ($\theta_2 = 180^\circ$), the Cassie-Baxter (1944) equation is obtained

$$\cos \theta = R_f f_{SW} \cos \theta_s + 1 - f_{SW} \quad (4.8)$$

where f_{SW} is the fractional solid-water contact area. It is assumed that the solid surface is rough, so the solid-water contact area is modified in equation (4.8) by

multiplying by the roughness factor R_f . In a similar manner, for the three-phase solid-oil-water interface the CA is given by

$$\cos \theta_o = R_f f_{SO} \cos \theta_{SO} + f_{OW} \cos \theta_{WO} \quad (4.9)$$

where $0 < f_{SO} < 1$ and $f_{OW} = 1 - f_{SO}$ are the fractional solid-oil and water-oil contact areas, and θ_{SO} and θ_{WO} are the CAs of solid-oil and water-oil interface, respectively. Since the value of $\cos \theta_{WO} = 1$, using equation (4.6) and equation (4.9), the contact angle in term of surface tensions is given by

$$\cos \theta_o = \cos \theta_{ow} f_{SO} + 1 - f_{SO} \quad (4.10)$$

where $\cos \theta_{ow}$ is given by equation (4.6).

Note that the same surface can be wetted either in the Wenzel or in the Cassie-Baxter regime, and the transition, usually from the higher energy Cassie-Baxter to the lower energy Wenzel state can be induced by external factors, such as vibration or pressure. This is due to the energy barriers which separate the wetting states, although the nature of this barrier is subject to argument in the literature. It has been argued recently that molecular reorientation at the triple line is primarily responsible for these energy barriers (Tadmor et al., 2008; Tadmor et al., 2009).

Figure 51 shows the wetting regimes as a function of $\cos \theta_{ow} / R_f$ and f_{SO} in accordance with the equation (4.10) for $R_f = 5$. The solid lines correspond to $\theta_3 = 90^\circ$ and $\theta_3 = 150^\circ$, so that the oleophobic area is confined between these two lines and is marked by grey color in Figure 51. For different values of R_f , the position of these solid lines will be slightly different. From this figure, it is found that for a constant value of $\cos \theta_{ow} / R_f$, when the fraction of solid-oil interface, f_{SO} , increases due to oil penetration between the asperities, initially oleophilic surface can become oleophobic and, with further increasing f_{SO} , the surface can become oleophilic again.

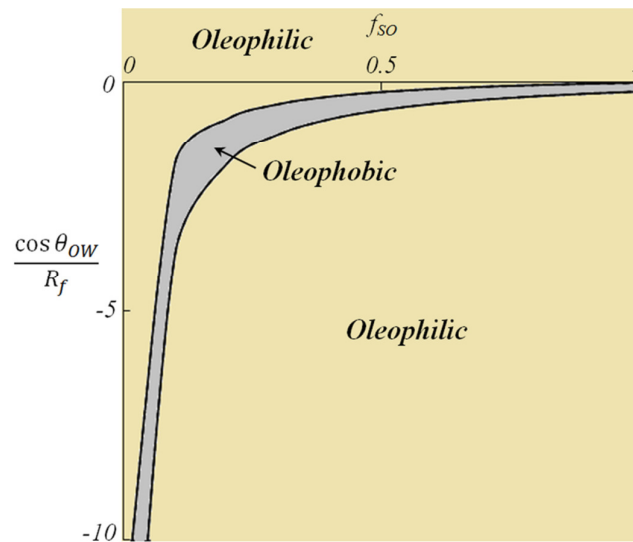


Figure 51. Oleophobic and oleophilic regimes for the three-phase rough solid-oil-water interface for $R_f = 5$.

4.1.1.3. Four-phase interface of solid-oil-water-air

When an oil droplet comes in contact with a rough solid surface in water environment, air bubbles (Ling et al., 2010; Ling et al., 2011) can be present on the surface inside crevices between oil droplet and the solid surface which cause a more complex four-phase solid-oil-water-air interface (Figure 47c). The CA can still be determined from the Cassie equation as

$$\cos \theta_4 = f_{SO} \cos \theta_{OW} + f_{OA} \cos \theta_{OA} + f_{OW} \cos \theta_{WO} \quad (4.11)$$

where $\cos \theta_{WO}=1$ and $\cos \theta_{OA}=-1$ (oil does not wet air) and the sum of fractional areas is $f_{SO} + f_{OA} + f_{OW} = 1$, the CA is given by

$$\cos \theta_4 = \cos \theta_{OW} f_{SO} + f_{SO} + 2f_{OW} - 1 \quad (4.12)$$

The same result can be obtained directly, rather than from the Cassie equation (equation 4.11), by writing

$$\gamma_{OW} \cos \theta_4 = (\gamma_{SW} - \gamma_{SO})R_f f_{SO} + (\gamma_{OA} - \gamma_{WA})f_{OA} + \gamma_{OW} f_{OW} \quad (4.13)$$

and noting that approximately $\gamma_{WA} - \gamma_{OA} = \gamma_{OW}$ (as oil tends to form a thin film on the water surface).

Note that in the case when air is absent ($f_{OA}=0$), equation (4.13) yields equation (4.9). In the case when water is absent at the interface ($f_{OW}=0$), one finds $f_{OA}=1-f_{SO}$ and equation (4.13) yields

$$\cos \theta_4 = \cos \theta_{OW} f_{SO} + f_{SO} - 1 \quad (4.14)$$

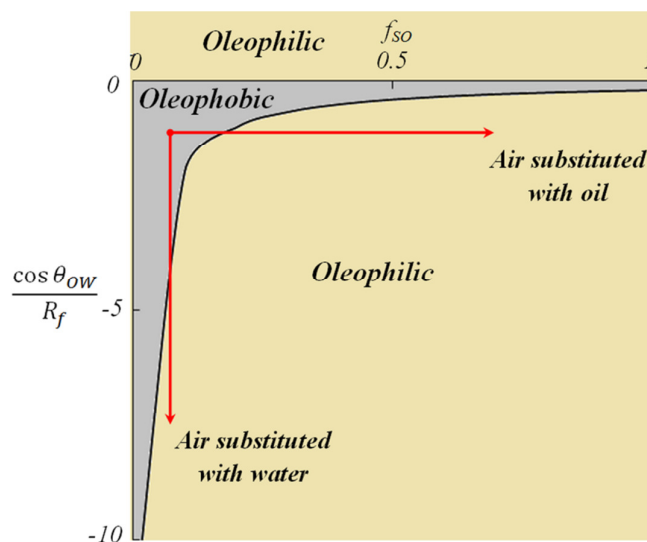


Figure 52. Oleophobic and oleophilic regimes for the four-phase rough solid-oil-water interface for $R_f = 5$.

Figure 52 shows the wetting regimes as a function of $\cos \theta_{OW} / R_f$ and f_{SO} in accordance with the equation (4.12) for $R_f=5$. The solid lines correspond to $\theta_4=90^\circ$ and $\theta_4=150^\circ$, so that the oleophobic area is confined between these two lines and is marked by grey color. Here we assumed that the oil-air and oil-water contact areas under the droplet are the same ($f_{OA}=f_{OW}$). It is observed that for a constant value of $\cos \theta_{OW} / R_f$, when the fraction of solid-oil interface, f_{SO} , increases due to penetrating oil, which substitutes for air in the pockets between the asperities, an initially oleophobic surface can become oleophilic with increasing values of f_{SO} . The same behavior is observed when air is substituted by water, as indicated by arrows in Figure 52.

4.1.1.4. Arbitrary number of phases

For an arbitrary number N of phases, equation (4.11) is generalized as

$$\cos \theta_o = \sum_{n=1}^N \cos \theta_n f_n \quad (4.15)$$

while the sum of the fractional areas is equal to unity

$$\sum_{n=1}^N f_n = 1 \quad (4.16)$$

Since one phase is solid-oil involving roughness and one phase is water, equation (4.12) for the angle of the multi-phase interface is now given by

$$\cos \theta_M = \cos \theta_{ow} f_{so} + f_{ow} + \sum_{n=3}^N \cos \theta_n f_n \quad (4.17)$$

where $\cos \theta_{ow}$ is calculated from equation (4.6) and summation is calculated from $n=3$ for all phases except water and oil.

4.2. Wetting transitions

In the preceding sections, we found that a rough surface can be wetted by different fluids, such as water, oil, and air, which are called wetting states. Transitions between these states are called wetting transitions. In this section we discuss the wetting transitions due to their relevance and importance for the wetting and oleophobicity.

4.2.1. Wetting transitions as a phase transition

Wetting transitions can be treated as phase transitions at the 2D interface using a phase field model (Vedantam and Panchagnula, 2007). For that end, two order-parameters, $\eta(x,y)$ and $\psi(x,y)$, can be introduced in order to characterize the state at a given point of the surface, so that $\eta = 1, \psi = 0$ for water, $\eta = 0, \psi = 0$ for oil, and $\eta = 0, \psi = 1$ for air at a point of the interface. Other values $0 < \eta < 1, 0 < \psi < 1$ correspond to

partial penetration of oil and water into cavities a given point of the solid surface. The energy density depends on the phase state at the point and on its gradient, and can be approximated as

$$\sigma(x, y) = f(\eta, \psi) + \lambda |\nabla f(\eta, \psi)| \quad (4.18)$$

where λ is the phenomenological gradient coefficient. The phenomenological function $f(\eta, \psi)$ can be built in a somewhat arbitrary manner; however, its minima should coincide with the equilibrium states of the system; furthermore, the value should correspond to the interfacial energy of this state, for example, $f(0,0)=\gamma_{SO}$, $f(1,0)=\gamma_{SW}$, and $f(0,1)=\gamma_{SA}$. For example, it can be defined as

$$f(\eta, \psi) = a_1(2\eta^4 - 3\eta^3 + \frac{1}{2}\eta^2 + a_2)(2\psi^4 - 3\psi^3 + \frac{1}{2}\psi^2 + a_3) \quad (4.19)$$

provided $a_1 a_2 a_3 = \gamma_{SO}$, $a_1(a_2 - 1/2)a_3 = \gamma_{SW}$, and $a_1 a_2(a_3 - 1/2) = \gamma_{SA}$ or $a_1 = \gamma_{SO} (1 - \gamma_{SO}/\gamma_{SW})(1 - \gamma_{SO}/\gamma_{SA})$, $a_2 = \gamma_{SO} / (\gamma_{SO} - \gamma_{SW})$, and $a_3 = \gamma_{SO} / (\gamma_{SO} - \gamma_{SA})$. The energy profile is shown in Figure 53 and it is observed that the energy minima correspond to the stable solid-air, solid-water, and solid-oil interfaces.

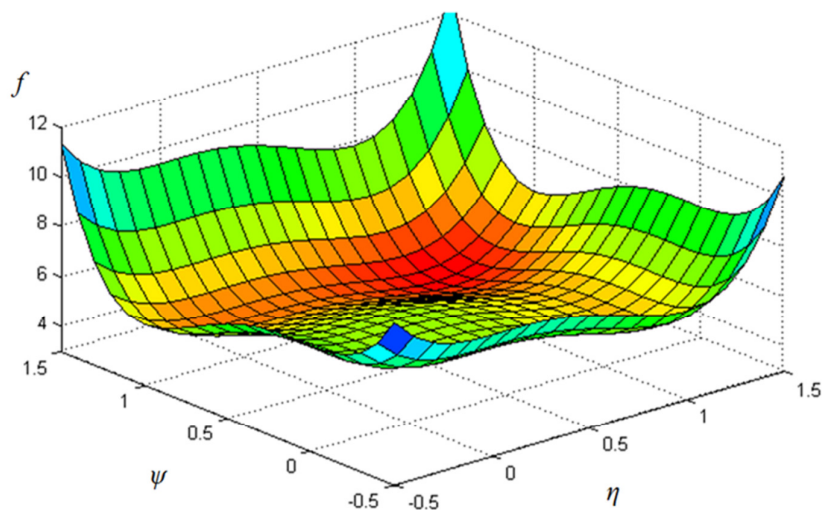


Figure 53. Interfacial energy as a function of order parameters.

The total energy per surface area A is calculated as

$$E = \int_A [f(\eta, \psi) + \lambda |\nabla f(\eta, \psi)|] dA \quad (4.20)$$

For example, in a 2D system (η and ψ depend only on x), if the phase state changes over the interval $x=0$ to $x=l$ from, say $\eta(0)=0$ to $\eta(l)=1$ and $\psi =0$, the energy per unit length is given by

$$\sigma = \int_0^l \left[f(\eta, 0) + \lambda \frac{\partial f}{\partial x} \right] dx = \int_0^l f(\eta, 0) dx + \lambda [f(1,0) - f(0,0)] = \lambda(\gamma_{sw} - \gamma_{so}) \quad (4.21)$$

or in the limit of small l

$$\sigma = \lambda(\gamma_{sw} - \gamma_{so}) = \lambda\Delta\gamma \quad (4.22)$$

The energy given by equation (4.22) constitutes an energy barrier per unit length between two phases. A number of important consequences can be made from the fact that such a barrier can exist.

First, suppose there is a circular spot of new phase with a lower energy γ_{so} with the radius of R surrounded by the area of larger energy γ_{sw} . The total energy associated with the spot of the new phase is $\pi R^2\Delta\gamma - \lambda\Delta\gamma 2\pi R$. Thus, it is energetically profitable for the spot to grow only when its radius is larger than the critical radius $R=2\lambda$, which corresponds to the energy barrier of $\Delta E = \pi\lambda^2\Delta\gamma$. This is the barrier preventing the wetting transition.

Second, the gradient term in equation (4.18) can be related to line tension of the Boruvka and Newman equation, as it was shown by Vedantam and Panchagula (2007). It represents the gradient energy which indicates the presence of energy barriers at the interfaces of different regions. Therefore formation of the interface between wetted and non-wetted regions is not energetically profitable.

Third, the CA hysteresis can be described by kinetic coefficient. The kinetic equation for order-parameter $\eta(x, y)$ according to Ginzburg-Landau functional is in the form

$$\beta\dot{\eta} = -\frac{dE}{d\eta} = \lambda\nabla^2\eta - \frac{\partial f}{\partial \eta} \quad (4.23)$$

where $\beta > 0$ is the kinetic coefficient. In general case, the value of β is dependent to η , $\dot{\eta}$, $\nabla\eta$, x , t . However in a simple case, when we assume the $\beta = \text{const}$ for an axisymmetric droplet which rolls on a surface, the following relation may be obtained (Jung and Bhushan, 2009)

$$\cos \theta_a - \cos \theta_r = 2\alpha\beta V \quad (4.24)$$

where θ_a and θ_r are advancing and receding CA, respectively, V is velocity of the rolling droplet and $\alpha = \int_0^\infty (\partial\eta / \partial r)^2 dr$.

Fourth, for a droplet on a surface with the footprint of radius R , the triple line tension which is related to gradient term in phase field method can be naturally calculated and yields the Boruvka and Neumann (Boruvka and Neumann, 1977) equation

$$\cos \theta = \frac{\gamma_{SA} - \gamma_{SW}}{\gamma_{WA}} - \frac{\tau}{R\gamma_{WA}} \quad (4.25)$$

where $\tau = \alpha\lambda$ is the contact line tension. The gradient term in equation (4.20) corresponds to the transition between the wetted and non-wetted regions and is proportional to the excess energy of formation of the interface between the phases. Thus we see that transitions between wetting states can be treated as phase transitions. In the consequent sections we will discuss experiments intended to find evidence that these wetting states can exist in multi-phase systems.

4.2.2. Experimental study

In order to verify the models described in the preceding sections, experiments with metallic composite materials were performed and wetting of four samples of aluminum base alloy and its graphite composite was studied experimentally. The Al-graphite composite samples were produced using the low-pressure infiltration of a bed of graphite particles with molten aluminum which solidified to form the composite

(Rohatgi et al., 1991). This included pressure infiltration of a bed of graphite particles with molten aluminum which solidified to form the composite. The aluminum samples were washed and cleaned with deionized water and then were grinded and polished through successive grinding steps with 400, 600 and 1200 grit silicon carbide paper and finally polished with a soft cloth impregnated with 1 micron silica. To remove the polishing debris, the samples were soaked in acetone for 10 min. Finally, the polished samples with different surface roughness were dried in air (Nosonovsky et al., 2011).

The microstructure of the samples was evaluated with the scanning electron microscope (SEM), SM-300. To modify surface roughness of the samples they were etched (Qian and Shen, 2005) with 40 ml of 37% HCL, 12.5 ml of H₂O and 2.0 ml of 48 wt% HF. The etching time was 10 and 20 seconds, respectively. The etched samples were all washed in water for 35 minutes to remove any etchant product formed and then dried in air prior to characterization.

Table 7. Contact angle of oil on submerged surface.

Sample	Measured contact angle		
	$R_a=0.2\mu m$	$R_a=0.7\mu m$	$R_a=0.8\mu m$
Al base alloy	43.1°	129.0°	140.7°
Al-graphite	24.9°	139.1°	141.3°

The surface roughness of the samples was measured before and after etching with a surface profilometer (Mitutoyo surtest. 402). The measured value by profilometer which we assume as roughness characteristic of the surface is the arithmetic mean value of surface roughness and is shown by R_a . The static CA of the oil droplets on the surfaces under water was measured by a standard ramé-hart

goniometer/tensiometer, model 250. The results are presented in Table 7. Distilled water and vegetable oil were used as the evaluation media.

A wetting regime transition, similar to the Cassie-Wenzel transition of the solid-water-air interface can occur at the solid-oil-water interface. The evidence of this is presented in Figure 54 showing a solid-oil-water system with the same aluminum alloy and its graphite composite of different surface roughness, as a solid, vegetable oil and water system. Aluminum alloy and aluminum graphite samples with $R_a = 0.2 \mu\text{m}$, showed lower CAs of $\theta_{OW}=43.1^\circ$ and $\theta_{OW}=24.9^\circ$, respectively whereas etched samples with higher roughness $R_a = 0.8 \mu\text{m}$ showed higher CAs of $\theta_{OW}=140.78^\circ$ and $\theta_{OW}=141.30^\circ$.

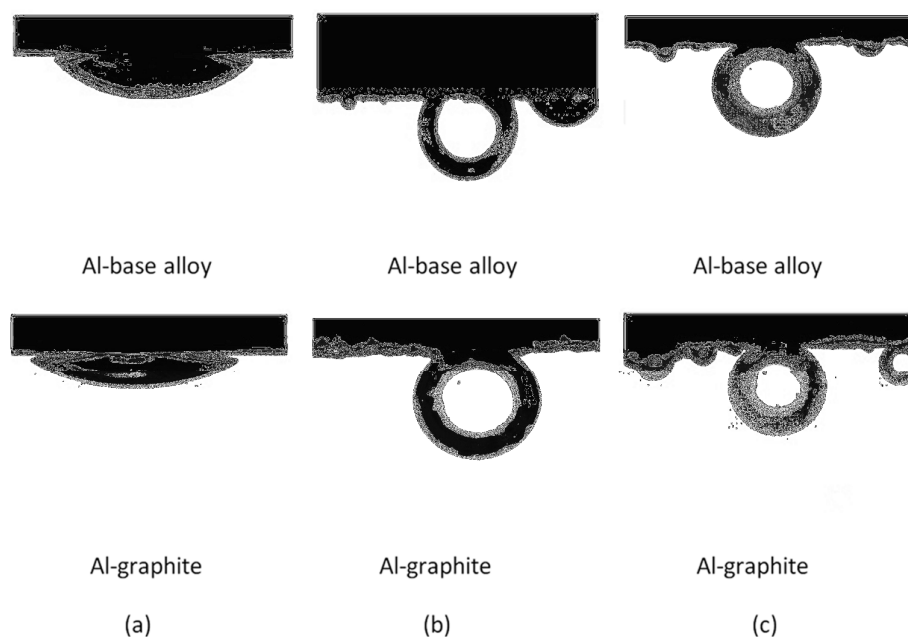


Figure 54. Experimental observation of the Wenzel and Cassie-Baxter wetting regimes in a solid-oil-water system for two materials (Al base alloy and Al-graphite composite) with different roughness (a) non-etched samples (b) samples etched for 10 seconds (c) samples etched for 20 seconds.

We attribute such change in the CA to the wetting transition from Wenzel to Cassie-Baxter state because the Wenzel state (homogeneous solid-oil interface) is expected for low-roughness samples, whereas the Cassie-Baxter state (composite

solid-oil-water interface) is expected for high-roughness samples. In the Cassie-Baxter state, air pockets (bubbles) can be trapped at the interface. However, air can dissolve in water with time and disappear, leaving space for oil and water which can fill the gaps between the asperities so that a wetting transition can happen (Figure 55).

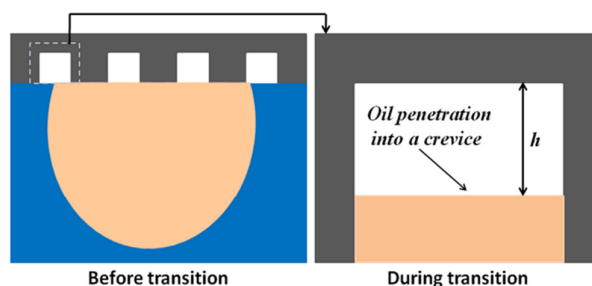


Figure 55. Cassie-Wenzel transition showing the oil-air interface parallel to the pillar base penetrating into the crevices between the pillars.

For rougher surface, oil penetration into the crevices is more difficult due to water entrapped in the crevices, so the Cassie-Baxter regime is more likely.

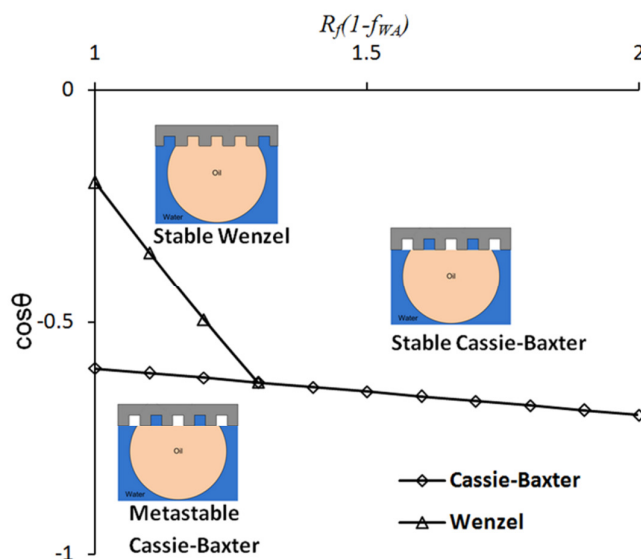


Figure 56. Contact angles in the Wenzel, stable and metastable Cassie-Baxter regimes as a function of surface roughness.

Figure 56 shows the CA versus roughness in the Cassie-Baxter and Wenzel wetting regimes. Higher CA normally corresponds to higher energy of the interface, so the crossing point of the dependencies corresponds to the configuration where the

net energies of these two regimes are equal (Lafuma and Quéré, 2003). The wetting transition can occur at that point. Furthermore, a metastable Cassie-Baxter state can exist for smaller values of the roughness factor. This is because an energy barrier separates these two states and an energy input is needed for the transition to the lower energy Wenzel state to occur. The surface roughness and geometry influence the energy barriers between the states.

4.2.3. Mechanisms of wetting transitions

In the preceding sections, we found that Wenzel and Cassie-Baxter states can coexist in the solid-water-oil system and that the wetting transition can be interpreted as a phase transition. In this section, we will discuss the physical mechanism of this transition and how the surface topography affects the transition.

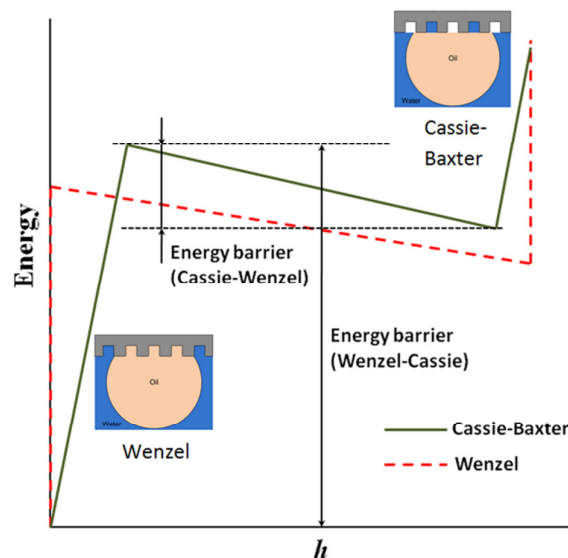


Figure 57. A typical net free energy dependency on the position of the interface, h .

Nosonovsky and Bhushan (2007) suggested that wetting transition is a multiscale process in the sense that interactions at three different length scale levels are involved: the CA is a macroscale parameter, the roughness pattern is microscopic,

whereas the effects which affect the stability of a wetting state are at the submicron level.

As a model example of a rough surface, it is convenient to consider a regular profile built of rectangular pillars with the height H , width W , and the pitch (periodicity) P . To investigate the advancement of the oil-air (or oil-water) interface into the crevices between the pillars we assume that the interface is horizontal and it is located at the distance of h from the pillar base. Figure 57 shows a typical dependency of the free energy versus the position of the interface, h as a dashed line. It might be concluded that the Wenzel state corresponds to higher net energy. However, at the moment when the interface reaches the pillar base ($h=0$) an abrupt energy drop occurs, so the real energy profile is better described by the solid line in Figure 57 (Nosonovsky and Bhushan, 2008a). It is observed that the energy barrier for the transition from the Cassie-Baxter to Wenzel regime is much smaller than that of the opposite transition, which makes the former transition virtually irreversible.

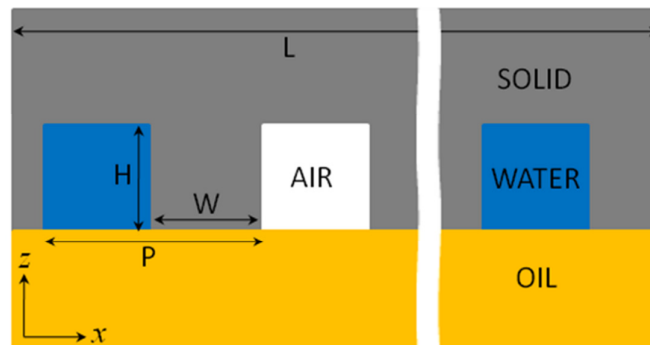


Figure 58. Schematic of a four-phase interface.

The characterization of the wetting state by the order-parameters, $\eta(x,y)$ and $\psi(x,y)$, can be related to different phase interface fractions of f_{SO} , f_{OW} and f_{OA} , using following relation can be achieved

$$f_{SO} = 1 - (\psi + \eta)(1 - W^2/P^2) \quad (4.26)$$

$$f_{OW} = \eta[1 - (\psi + \eta)W^2/P^2] \quad (4.27)$$

$$f_{oA} = \psi[1 - (\psi + \eta)W^2/P^2] \quad (4.28)$$

where these three equations are valid while $\psi + \eta \leq 1$. It is noted; however, that the order-parameters characterize wetting state at a point whereas the fractional areas characterize the areas of the interface.

To investigate the effect of surface pattern on wetting transition, it is convenient to introduce the spacing factor, $S_p=W/P$ (Nosonovsky and Bhushan, 2008a). As shown in Figure 58, for the solid-oil-water three-phase interface, f_{ow} and R_f are equal to $1-W^2/P^2$ and $1+4HW/P^2$, respectively. Assuming $H=2W$ and $R_f=1$ for Cassie-Baxter state, the Wenzel and Cassie-Baxter equations, equations (4.5) and (4.8) yield

$$\cos \theta_{ow} = (1 + 8S_p^2) \cos \theta_0 \quad (4.29)$$

$$\cos \theta_{ow} = S_p^2 (\cos \theta_0 + 1) - 1 \quad (4.30)$$

where θ_0 is the CA with a smooth surface and θ_{ow} is the CA with the patterned surface.

Figure 59 shows theoretical values of the CA for the Wenzel and Cassie-Baxter states versus the spacing factor, S_p^2 for the values of θ_0 corresponding the smooth Al-base alloy and Al-graphite composite as obtained from equations (4.29) and (4.30). It is observed that for an initially hydrophilic material, the Wenzel CA rapidly decreases ($\cos\theta$ increases) and reaches zero at about $S_p^2=0.1$. The Cassie-Baxter CA also decreases with increasing roughness.

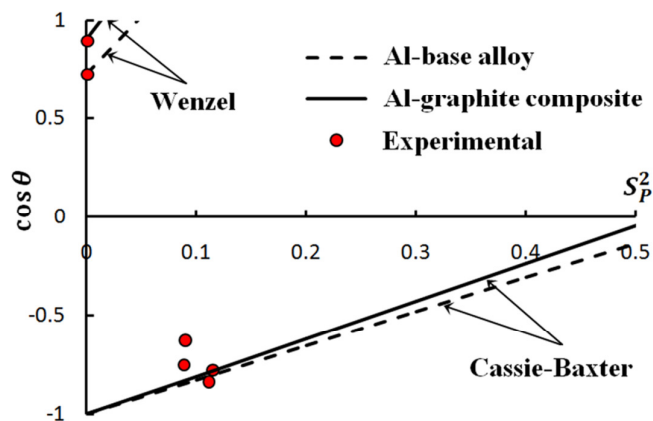


Figure 59. The contact angle versus the spacing factor, S_p^2 for Al and Al-graphite composite.

The experimental values corresponding to our observation of oleophobic surfaces are also shown in Figure 59 by red dots. Although our samples were not patterned and had random roughness, we assumed, on the basis of roughness measurements and atomic force microscopy (AFM) imaging, that the etched samples are equivalent, to some extent, to a micropatterned surface with $S_p^2=0.1$ whereas for non-etched samples we took $S_p^2=0$. The significant change of the contact angle is consistent with the transition between the Wenzel and Cassie-Baxter regimes. Thus, we concluded that the non-etched samples were in the Wenzel wetting states whereas the etched samples were in the Cassie-Baxter wetting state. Therefore, our data present evidence that the two wetting states, which are well known in the case of the solid-water-air systems, can coexist also in solid-oil-water systems.

4.2.4. Effect of surface topography on wetting transitions

We investigate the effect of surface roughness on wetting of brass solid surfaces immersed in water and demonstrate that these two states exist and that the surface roughness controls whether the system is in the Wenzel or Cassie-Baxter

state. The observations are crucial for the development of novel oleophobic, omniphobic, and anti-fouling surfaces.

Wetting transitions have been intensively studied recently due to their relevance and importance for the superhydrophobicity, oleophobicity and omniphobicity (Tsai et al., 2009; Manukyan et al., 2011; Kwon et al., 2011; Choi and Kim, 2006; Poetes et al., 2010; Hejazi & Nosonovsky, 2012; Nosonovsky, 2011). Whereas wetting transitions on superhydrophobic surfaces are well studied (Nosonovsky & Bhushan, 2008b; Nosonovsky & Bhushan, 2007c; Nosonovsky, 2007b; Nosonovsky & Bhushan, 2008c; Bormashenko et al., 2007b; Patankar, 2004a; Tadmor et al., 2009; Kietzig et al., 2009), little is known about wetting transition during the contact of non-polar liquids (such as organic oils) with rough solid surfaces. In our earlier study we suggested that such transitions are possible due to the occurrence of composite (Cassie-Baxter) and homogeneous (Wenzel) wetting states in underwater oleophobicity (Hejazi & Nosonovsky, 2012). In this Letter, we investigate the effect of surface topography on wetting transition of an underwater interface of solid-oil and demonstrate that roughening a solid surface can drive the transition from Wenzel to Cassie-Baxter state.

When a water droplet is placed on a rough solid surface, wetting can happen in accordance to one of the two scenarios: the homogeneous (Wenzel) or composite (Cassie-Baxter) regimes. These regimes correspond to two wetting states. In the Cassie-Baxter state, there are air pockets being trapped between the water droplet and the solid surface yielding a partially wetted surface, whereas in the W state, the water droplet completely wets the surface (Nosonovsky & Bhushan, 2008a). It is expected that similar wetting states can exist during wetting of a rough solid by other liquids,

such as oils and other non-polar organic liquids, and in systems involving more than one liquid, such as solid-oil-water.

Figure 60 shows an oil droplet deposited on a rough solid surface when immersed in water. In this case, when air bubbles or tiny water droplets are trapped between the oil droplet and the solid surface, the Cassie-Baxter state can occur (Figure 60b), whereas for a fully oil-wetted solid surface, the W state occurs (Figure 60a).

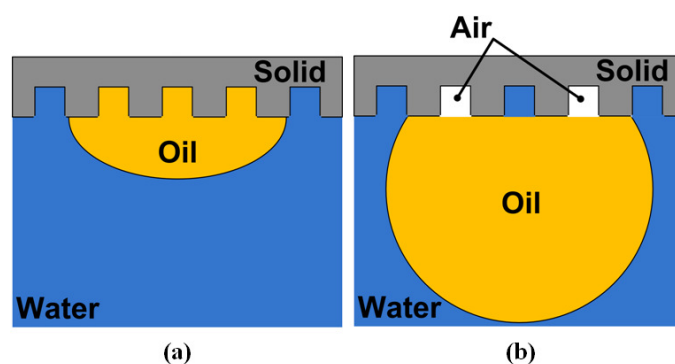


Figure 60. Schematic of underwater interface (a) Wenzel state. (b) CB state.

The CB state usually displays a larger contact angle (CA) of oil than the W state. When the CA is larger than 90° , the surface is called oleophobic, whereas otherwise it is called oleophilic. For a surface immersed in water, the phenomenon is called underwater oleophobicity/philicity. Wetting properties depend on the balance of interfacial free energies of different phases present at the interface.

Experimental results are reported here for oil droplets on solid substrates made by Brass 360 immersed in water. Brass was used due to its resistance to corrosion which is of importance for underwater applications. Distilled water and vegetable oil were used as the evaluation media. The 7 samples of Brass 360 were sectioned into $2.0 \text{ cm} \times 1.0 \text{ cm} \times 0.3 \text{ cm}$ pieces and mounted in epoxy resin using the Simplimet 3000 automatic mounting press and then washed and cleaned with deionized water. After that, the sample surface was roughened. In order to obtain the surface roughness

of different orders of magnitude, 6 samples were mechanically abraded with 50, 80, 180, 320, 600 and 1200 grit silicon carbide papers for 2 minutes and then polished with a soft cloth impregnated with 1 μm silica particles to remove debris. The last sample was only polished by the foregoing soft cloth. Finally, the polished samples with different surface roughness were air-dried (Nosonovsky et al., 2011).

The surface roughness of all samples was measured using a surface profilometer (Phase II, SRG-4500). The profilometer measured the value of the average surface roughness, R_a , as a roughness characteristic of the surface. The values of R_a of the samples surface were 3.3, 1.9, 1.2, 0.7, 0.5, 0.2 and 0.1 μm . The microstructure of the samples was evaluated with a Scanning electron microscope (SEM) SM-300, and it is shown in Figure 61.

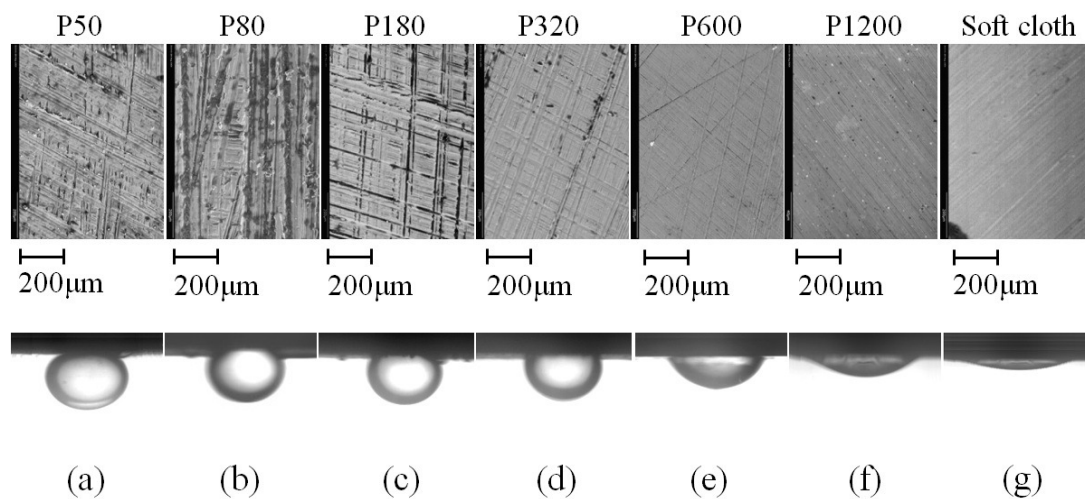


Figure 61. SEM of samples and underwater oil droplet pics. (a) Brass 360 abraded with SiC paper (336 μm particle size), (b) Brass 360 abraded with SiC paper (201 μm particle size), (c) Brass 360 abraded with SiC paper (82 μm particle size), (d) Brass 360 abraded with SiC paper (46 μm particle size), (e) Brass 360 abraded with SiC paper (26 μm particle size), (f) Brass 360 abraded with SiC paper (15 μm particle size), (g) Brass 360 abraded with soft cloth (1 μm particle size).

The CA of deionized water and vegetable oil droplets in air and for oil droplets in water deposited on the Brass 360 substrates was measured by a standard

model 250 ramé-hart goniometer/tensiometer. It is observed from Figure 61 that rougher surfaces, when immersed in water, have larger CA with oil than smoother surfaces.

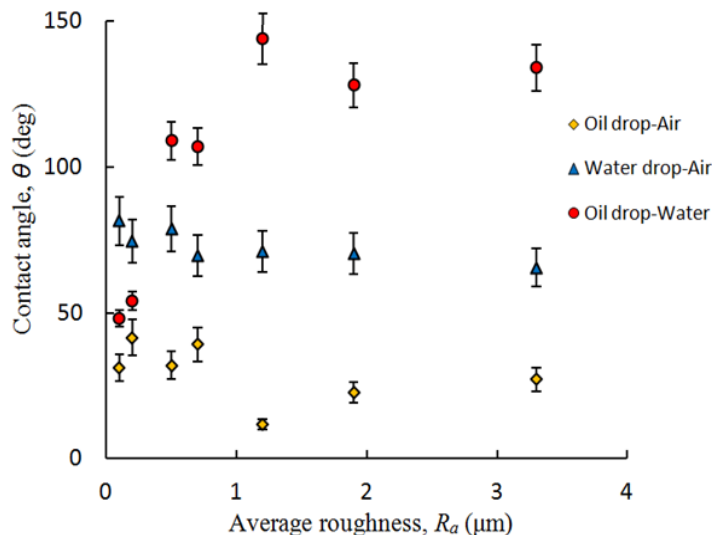


Figure 62. Oil CA, Water CA and underwater oil CA of samples versus average roughness, R_a .

The measurements were repeated five times at different locations on the sample surface, and for each sample the results were averaged. Figure 62 shows the CA of water and oil droplets on substrates with different average roughness, R_a , as well as the CA of oil droplet deposited on the substrates immersed in water. It is observed that for water droplets, there is no significant change in the CA with increasing R_a . The CA of oil droplets in air gradually decreases with increasing roughness from the value of about 42° and reaches its minimum of 15° at $R_a=1.2 \mu\text{m}$. With further increasing roughness the CA slightly grows up to the value of 27° .

For oil droplet in water, a steep increase of the CA is noticed when $R_a = 0.7 \mu\text{m}$. The values of the CA grow abruptly from 55° (underwater oleophilicity) to 110° (underwater oleophobicity). This abrupt increase of the CA and the change of the

wetting regime from oleophilicity to oleophobicity require an explanation. We attribute it the wetting transition from the W to CB regime.

4.2.5. Wetting transitions discussion

In the Wenzel regime, the CA for a rough surface, θ_W , is given by

$$\cos \theta_W = R_f \cos \theta_0 \quad (4.31)$$

where R_f is the roughness factor defined as a ratio of the surface area to its flat projection and θ_0 is the CA of the droplet with a smooth surface. Note that both R_f and R_a are the measures of surface roughness; however, $R_f \geq 1$ is a non-dimensional parameter, and $R_f = 1$ for a smooth surface, whereas $R_a \geq 0$ is a dimensional parameter, and $R_a = 0 \mu\text{m}$ for a perfectly smooth surface. It is however expected that increasing R_a corresponds to increasing R_f . According to equation (4.31), for initially oleophilic surface ($\cos \theta_0 > 0$), increasing roughness cannot result in the transition to oleophobicity ($\cos \theta_W < 0$). Therefore, the regime change from the oleophilicity to oleophobicity observed in Figure 62 cannot be explained by the Wenzel model.

In the Cassie-Baxter regime, the CA for a rough surface, θ_{CB} , is given by (Hejazi & Nosonovsky, 2012)

$$\cos \theta_{CB} = f_{SO} (R_f \cos \theta_0 + 1) - 1 \quad (4.32)$$

where θ_0 is the CA of an oil droplet in water with a smooth solid surface, R_f is roughness factor applied to the solid-oil contact area, and f_{SO} is the fractional solid-oil contact area. It is observed from equation (4.32) that the abrupt change of the underwater solid-oil CA, as reported in Figure 62, can be attributed to abrupt change of either f_{SO} or R_f . Roughening the surface with the sandpaper results in increasing R_a and can lead to increasing R_f . However, for a surface with a $\cos \theta_0 > 0$ (oleophilic) the increase of R_f cannot result in the change of the sign of $\cos \theta_0$ from positive

(oleophilic) to negative (oleophobic). Therefore, the only plausible explanation to the above-mentioned abrupt growth of the oil contact angle underwater from 55° to 110° is an abrupt change of the solid-oil contact area f_{SO} . A rougher surface has larger cavities so that air or water pockets can be trapped between the solid surface and oil droplet. Note that $f_{SO} = 1$ corresponds to the Wenzel regime and an abrupt drop of the contact area from $f_{SO} = 1$ means the wetting transition from Wenzel to Cassie-Baxter regime.

The values of the CA of oil with a solid in water are presented in Figure 63 as calculated from the W (equation (4.31)) and CB (equation (4.32)) models. It was assumed that R_f growth with R_a (measured in micrometers) $R_f = R_a / (3 + 0.5R_a) + 1$. For CB, it was assumed $f_{SO} = 0.15$. Such a choice of the parameters provides a reasonable fit of the experimental values for small roughness ($R_a < 0.3 \mu\text{m}$) with the W model and for large roughness ($R_a > 0.7 \mu\text{m}$) with the CB model. However, the assumption of the constant solid-oil contact area does not stand in the transition region ($0.3 \mu\text{m} < R_a < 0.7 \mu\text{m}$). To account for the change of f_{SO} during the Wenzel to Cassie-Baxter transition, we assumed a piece-wise dependency

$$f_{SO} = \begin{cases} -0.956R_a + 0.95 & ; \quad 0 \mu\text{m} \leq R_a < 0.7 \mu\text{m} \\ -0.06R_a + 0.33 & ; \quad 0.7 \mu\text{m} \leq R_a < 3.3 \mu\text{m} \\ 0.15 & ; \quad R_a \geq 3.3 \mu\text{m} \end{cases} \quad (4.33)$$

The CB model (equation (4.32)) with the account for the changing f_{SO} (equation (4.33)) can explain the experimental trend as seen in Figure 63.

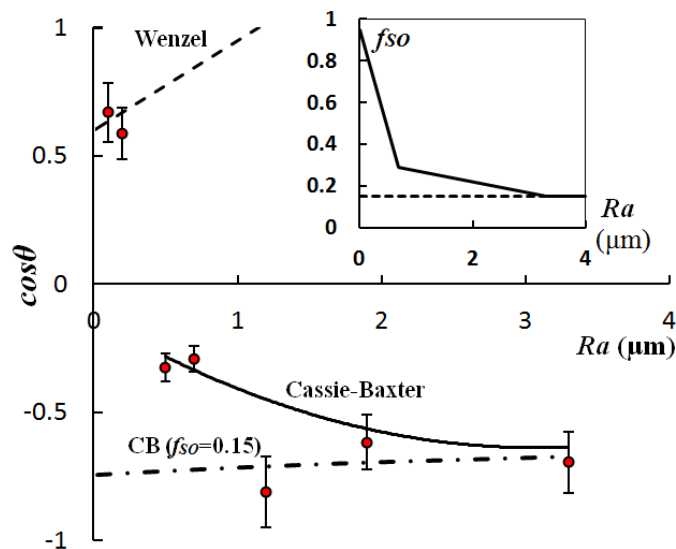


Figure 63. CA of oil with a rough Brass surface under water versus surface roughness, Ra , for W ($f_{so}=1$), CB with a constant solid-oil contact area fraction ($f_{so} = 0.15$) and CB with solid-oil contact area fraction dependent on roughness.

4.3. Conclusion

Wetting of rough surfaces can be more complex than what is predicted by two basic models (the Wenzel and Cassie-Baxter models). A multi-phase interface can form when water, oil and air are contacting with a rough solid surface. We developed models for three- and four-phase rough interfaces, which can be generalized for an arbitrary number of phases. We also used a phenomenological phase-field model for wetting transitions on the multi-phase interfaces. The model relates CA hysteresis, line tension, and energy barriers for wetting transitions. We investigated wetting transitions on a modeled patterned surface and reported observations of wetting transitions on solid-oil-water interfaces. Such interfaces can be used for the design of bio-inspired underwater self-cleaning, oleophobic and antifouling surfaces mimicking antifouling properties of fish scale. Multiphase interfaces can also form with lubricant-infused self-lubricating surfaces.

In addition, we investigated wetting of rough Brass surfaces by water, oil in air and oil in water. We found an abrupt increase of the contact angle for the oil underwater system. The increase cannot be explained by the standard Wenzel and Cassie-Baxter models; however, it is consistent with the wetting regime change (wetting transition) from Wenzel to Cassie-Baxter. Such wetting transitions are known for superhydrophobic surfaces; however, we report for the first time about such transition for wetting of a rough surface with an organic non-polar liquid.

CHAPTER FIVE

5. ICEPHOBICITY

Water freezing and ice formation during the cold weather can sometimes be disastrous. As explained in chapter 3, freezing the water trapped inside the pores of concretes used in a structure can cause concrete damages and a structural failure as a result. Also ice formation on exposed surfaces and structures such as electric power transmissions, telecommunication networks (towers and antennas), and transportation (vessels, airplanes, roads, and bridges) can cause disastrous problems. For instance, ice accumulation on these structures has caused communication towers, antennas and satellite dishes to overturn and be destroyed, caused accidents from falling ice off of bridges, and caused many injuries to people walking under cables with falling ice. The winter storm can cause serious damages to power lines and telecommunication networks. In addition, formation of ice and snow on aircrafts can seriously affect the aircraft operation during the flight or in take-off. Beginning in 1991, there have been tremendous efforts to develop de-icing systems and to design anti-icing materials. Numerous advancements in aircraft de-icing glycol-based fluids have emerged in recent years. However, these advancements have not eliminated the potential negative effects of these fluids on the environment. Propylene glycol is known to exert high levels of biochemical oxygen demand (BOD) during degradation in surface waters. This process can noxiously affect the environment and particularly the aquatic life. Moreover, considering that it takes approximately 1,000 gallons of glycol (costing about \$10 per gallon) to de-ice a typical aircraft, de-icing costs \$10,000 per aircraft. These negative impacts have developed a need for airlines to initiate new methods to remove ice, snow, or frost from the airplane wings, control surfaces, propeller, and

engine outlets. Anti-icing capability of the superhydrophobic surface is much encouraging to design low cost eco-friendly icephobic materials.

Many icephobic materials with low adhesion properties are commercially available. However these materials will not prevent ice buildup and the ice forms on these materials with the same rate as other types of materials. These materials basically reduce the adhesion force and the bond strength between the ice and the material's molecules. As a result, less energy is required to remove accreted ice from their surface. Therefore, icephobic materials are usually used simultaneously with other ice removal techniques including heating, electro-expulsion, pneumatic expulsion and so on.

In this chapter, the icephobicity of materials such as MMCs, concretes and polymers will be investigated. Models will be proposed to predict icephobic properties of these materials by analyzing the adhesion force of formed ice to them. In addition, experimental work will be employed to investigate the icephobicity and anti-icing properties of these materials.

5.1. Literature survey

The terms “icephobic” or “icephobicity” have been used in the literature recently (Meuler et al., 2010a; Meuler et al., 2010b; Kulinich and Farzaneh, 2004; Zheng et al., 2011; Jung et al, 2011; Nosonovsky and Hejazi, 2012; Kulinich et al., 2011; Bahadur et al., 2011; Dotan et al., 2009; Menini et al., 2011; Farhadi et al., 2011), although the words are relatively new and still absent from the Oxford English Dictionary. The keyword “icephobic” was used for the first time by Kulinich & Farzaneh (2004) as well as in some industrial reports (Sivas et al., 2007; Pratt & Whitney Company, 2004). Next time, in the form “ice phobic” it appears in 2008 (Ferrick et al., 2008) in the work done at NASA. After that, the term appears

many times in the literature. (Jung et al., 2011; Nosonovsky & Hejazi, 2012; Kulinich et al., 2011; Meuler et al., 2010b; Menini and Farzaneh, 2009; Kim et al., 2012).

The term is analogous to the hydrophobicity and other “-phobicities” (oleophobicity, lipophobicity, omniphobicity, amphiphobicity, etc); however, an exact thermodynamic definition of icephobicity is missing from the literature. The extensive controversy among scholars on whether the icephobicity is related to the superhydrophobicity came to a conclusion that there is no direct correlation (Jung et al., 2011; Nosonovsky & Hejazi, 2012; Kulinich et al., 2011).

In recent publications there are at least three different approaches to the characterization of surface icephobicity. First, icephobicity implies low adhesion force between ice and a solid surface. In most cases, the critical shear stress is calculated, although the normal stress is used as well. The researchers call “icephobic” surfaces with the shear strength between 150 kPa and 500 kPa (Meuler et al., 2010b; Menini and Farzaneh, 2009) and even as low as 15.6 kPa (Kim et al., 2012). Second, some scholars define icephobicity as the ability to prevent ice formation on the surface. Such ability depends on whether a droplet of supercooled water (below the normal freezing temperature of 0 °C) freezes at the interface and it can be characterized by time delay of heterogeneous ice nucleation (Jung et al., 2011; Jung et al., 2012; Gou et al., 2012). The mechanisms of droplet freezing are quite complex and depend on the temperature level, on whether cooling is performed from the side of the solid substrate or from vapor, and on other factors. Third, an impact test for bouncing-off droplets was suggested (Zheng et al., 2011) implying that icephobic surfaces repel incoming small droplets (e.g., of rain or fog) at the temperatures below the freezing point.

These three definitions of icephobicity correspond to three different, although related, properties of anti-icing surfaces: they should (i) prevent freezing of water condensing on the surface (ii) prevent freezing of incoming water (iii) if ice formed, it should have weak adhesion strength with the solid, so that it can be easily removed. Mechanical properties of ice and the substrate also of great importance since ice shedding occurs as fracture, either in the Mode I (normal) or Mode II (shear) cracking, so that crack concentrators are major contributors to the reduced strength (Nosonovsky and Hejazi, 2012).

All of the above considerations suggest that a universal definition of the icephobicity can be a difficult task and the parallel with the superhydrophobicity should be examined in depth. The superhydrophobicity is defined by the water contact angle (CA) $>150^\circ$ and by low CA hysteresis (Nosonovsky and Rohatgi, 2012; Nosonovsky et al., 2011), although very high CA can co-exist with high CA hysteresis (the rose petal effect) (Bhushan and Nosonovsky, 2010b). Low CA hysteresis corresponds to shear mode of loading at the solid-water interface while a high CA corresponds to the normal loading (Chapter 2; origins of CA hysteresis). The ability to bounce-off incoming droplets constitutes the third aspect of the superhydrophobicity (Nosonovsky and Bhushan, 2008c).

Besides the parallel between the icephobicity and superhydrophobicity for water / ice repellency, there are similarities on other levels including the hydrophobic effect / hydrophobic interactions, mechanisms of protein folding (random-structure coil protein folds into an ordered three-dimensional structure) and ice crystal formation.

5.2. Forces and interaction analysis

Dewetting and deicing are essentially mechanical processes involving three-phase line “friction” due to CA hysteresis (Dussan & Chow, 1983) and mode I or mode II fracture, respectively. Deicing occurs as fracture, either in mode I (normal) or mode II (shear) cracking, so the crack concentrators are major contributors to the reduced strength. To account for these effects we need to write the balance equations for mechanical forces and moments acting on the droplet and on ice particle.

5.2.1. Water droplet

For a water droplet placed on a surface (Figure 64a), we approximated the CA as

$$\begin{aligned} \cos \theta(\alpha) &= \cos \theta_0 + A \sin \psi \left(\sin^2 \left(\frac{\alpha}{2} + \frac{\pi}{4} \right) + (\xi - 1) \cos^2 \left(\frac{\alpha}{2} + \frac{\pi}{4} \right) \right) = \\ & \cos \theta_0 + \frac{A}{2} \sin \psi [\xi + (2 - \xi) \sin \alpha] \end{aligned} \quad (5.1)$$

where θ_0 is the water CA on a horizontal surface, ψ is the tilt angle, α is the angle of the position on the triple line in a cylindrical coordinate system with z-axis as its longitudinal axis (Figure 64b), A is a constant which characterizes the amplitude of CA hysteresis. To characterize the asymmetry in change of CA, we introduce the parameter $-1 < \xi < 1$. The symmetric case corresponds to $\xi = 0$ where the change in advancing and receding CAs is equal. When ξ is between 0 and 1, the decrease in receding CA is more than the increase in advancing CA whereas for ξ between 0 and -1, the increase in advancing CA is more than the decrease in receding CA. The value of ξ depends on the properties of the solid surface.

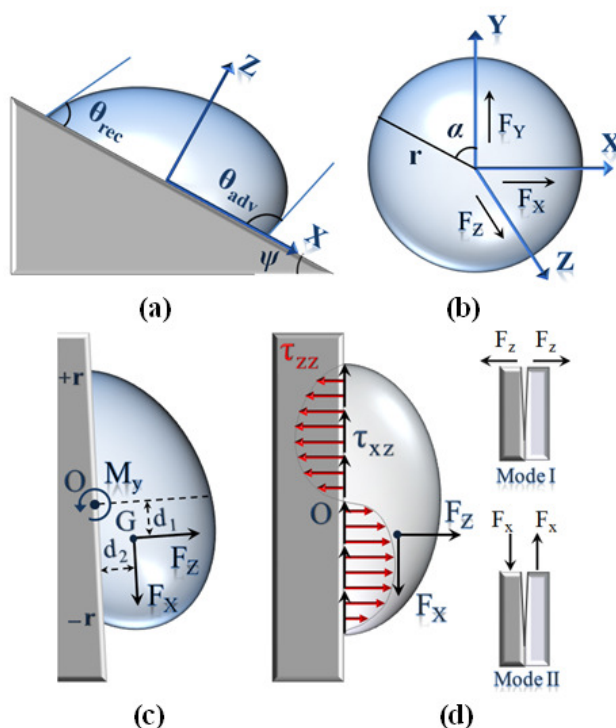


Figure 64. Schematic of the water droplet and ice on the surface (a) Side view of the water droplet placed on the surface with the tilt angle ψ (b) Top view of a water droplet placed on the surface (c) Side view of the water droplet placed on the tilted surface and forces and the moment applied to it (d) Side view of the ice formed on the vertical surface, forces applied to it. Ice detachment occurs as the Mode I (crack opening) and Mode II (shear) fracture (Hejazi et al., 2013).

The receding and advancing CAs on the tilted surface are given by substituting $\alpha = \pi/2$ and $\alpha = 3\pi/2$ into equation (5.1), respectively.

$$\cos \theta_{rec} = \cos \theta_0 + A \sin \psi \quad (5.2)$$

$$\cos \theta_{adv} = \cos \theta_0 + A(\xi - 1) \sin \psi \quad (5.3)$$

The CA hysteresis (the difference between the cosines of advancing and receding CA) is

$$\cos \theta_{adv} - \cos \theta_{rec} = A(\xi - 2) \sin \psi \quad (5.4)$$

The surface tension of a droplet placed on a solid surface at each point on the triple line can be presented in the vector form as

$$\vec{\gamma}(\alpha) = \gamma_x \vec{i} + \gamma_y \vec{j} + \gamma_z \vec{k} \quad (5.5)$$

where γ_x , γ_y and γ_z are x-, y- and z-component of water-air interfacial energy and given by

$$\gamma_x = \gamma \cos \theta \sin \alpha \quad (5.6)$$

$$\gamma_y = -\gamma \cos \theta \cos \alpha \quad (5.7)$$

$$\gamma_z = \gamma \sin \theta \quad (5.8)$$

Substituting equations (5.6), (5.7), and (5.8) into equation (5.5) yields

$$\vec{\gamma}(\alpha) = \gamma \cos \theta \sin \alpha \vec{i} - \gamma \cos \theta \cos \alpha \vec{j} + \gamma \sin \theta \vec{k} \quad (5.9)$$

where γ is the water-air interfacial energy (about 0.072 Jm^{-2} at room temperature).

Considering the free body diagram of the water droplet placed on the surface, the external forces F_x , F_y , and F_z applied in x, y, and z direction, the surface tension force of water droplet acting upon the triple line, and the reaction force of the surface to the Laplace pressure inside water droplet applied to the solid-liquid wetting area are present. One can assume that F_x , F_y , and F_z are the gravity forces applied to the center of gravity of the water droplet, G , as $F_x = Mg \sin \psi$, $F_y = 0$ and $F_z = -Mg \cos \psi$. The gravity force has no component in y direction. M is the mass of the droplet and g is the acceleration of gravity. The Laplace pressure has no components in x and y directions because it is applied perpendicular to the surface, therefore it should be considered only in z direction equation of force balance. Equations of balance of the forces and the moments per unit length can be presented as

$$F_x + \int_0^{2\pi} \gamma_x d\alpha = 0 \quad (5.10)$$

$$F_y + \int_0^{2\pi} \gamma_y d\alpha = 0 \quad (5.11)$$

$$F_z + \int_0^{2\pi} \gamma_z d\alpha + r \int_0^{2\pi} p(x) \cos^2 \alpha d\alpha = 0 \quad (5.12)$$

where $p(x) = (P_L + \rho g x)$ is the Laplace pressure applied to the solid-liquid interface. Laplace pressure is inversely proportional to the local droplet curvature.

The difference in the local curvature of the droplet induced by tilting the surface, results in change in internal Laplace pressure at each point at the solid-liquid interface. Since the droplet is in an equilibrium configuration, the forces are balanced. Substituting equation (5.1) into equation (5.6) and the result into equation (5.10) yields

$$F_x = - \int_0^{2\pi} \gamma \left(\cos \theta_0 + \frac{A}{2} \sin \psi [\xi + (2 - \xi) \sin \alpha] \right) \sin \alpha \, d\alpha \quad (5.13)$$

The y-components of surface tension at the triple line are balanced due to the symmetry, therefore $F_y = 0$.

Assuming $x = -r \sin \alpha$ and $y = r \cos \alpha$, substituting equation (5.8) into equation (5.12) and considering the value of $p(x)$ yields

$$F_z = - \int_0^{2\pi} \gamma \sin \theta \, d\alpha - r \int_0^{2\pi} (P_L - \rho g r \sin \alpha) \cos^2 \alpha \, d\alpha \quad (5.14)$$

Calculating the second integral, considering the value of $\sin \theta = (1 - \cos^2 \theta)^{1/2}$ and substituting equation (5.1) into equation (5.14) gives

$$F_z = - \int_0^{2\pi} \gamma \sqrt{1 - \left(\cos \theta_0 + \frac{A}{2} \sin \psi [\xi + (2 - \xi) \sin \alpha] \right)^2} \, d\alpha - \pi P_L r \quad (5.15)$$

where r is the radius of the droplet and P_L is the average Laplace pressure applied to the solid-liquid interface of a horizontal surface.

Assuming $f(\alpha) = \sqrt{1 - \left(\cos \theta_0 + \frac{A}{2} \sin \psi [\xi + (2 - \xi) \sin \alpha] \right)^2}$, The value of F_z can be obtained as

$$F_z = -\gamma \int_0^{2\pi} f(\alpha) \, d\alpha - \pi P_L r \quad (5.16)$$

For small values of A , $f(\alpha)$ can be approximated as

$$f(\alpha) = \sin \theta_0 + \frac{\cos \theta_0 \sin \psi (\xi + (2 - \xi) \sin \alpha)}{2 \sin \theta_0} A \quad (5.17)$$

Equations of balance of the moments per unit length can be presented as

$$M_y = F_x d_1 - F_z d_2 - r^2 \int_0^{2\pi} p(x) \sin \alpha \cos^2 \alpha \, d\alpha - r \int_0^{2\pi} \gamma_z \sin \alpha \, d\alpha \quad (5.18)$$

$$M_x = M_z = 0 \quad (5.19)$$

where d_1 and d_2 are the distances from the point G to the x and z axes, respectively (Figure 64c).

The force equations are

$$F_x = -\frac{\pi}{2}\gamma A(2 - \xi)\sin\psi \quad (5.20)$$

$$F_y = 0 \quad (5.21)$$

$$F_z = -2\gamma\pi \sin\theta_0 - \frac{\gamma\pi\xi \cos\theta_0 \sin\psi}{\sin\theta_0} A - \pi P_L r \quad (5.22)$$

Substituting equations (5.20) and (5.22) into equation (5.18) yields

$$M_y = -\left(\frac{\pi}{2}\gamma A(2 - \xi)\sin\psi\right) d_1 + d_2\gamma \left(2\pi \sin\theta_0 + \frac{\pi\xi \cos\theta_0 \sin\psi}{\sin\theta_0} A\right) + \pi P_L r d_2 - \frac{\pi\rho g r^3}{4} + \frac{r\gamma\pi(\xi-2)A \cos\theta_0}{2 \sin\theta_0} \sin\psi \quad (5.23)$$

For the water droplet placed on the tilted surface, considering equations (5.20), (5.22) and (5.23) and assuming $d_1 = 3r/8$, the balance of forces and the moment in matrix form can be given as

$$\begin{bmatrix} 0 & \frac{\pi}{2}\gamma & 0 & 0 & 0 \\ -\frac{2\pi\gamma\cos\theta_0}{\sin\theta_0} \sin\psi & -\frac{\pi\gamma\cos\theta_0}{\sin\theta_0} & 0 & 0 & -\pi P_L r - 2\pi r \sin\theta_0 \\ 0 & \frac{3\pi}{16} r\gamma & \pi P_L r + 2\pi r \sin\theta_0 & \frac{\pi\xi \cos\theta_0}{\sin\theta_0} \sin\psi & -\frac{\pi\rho g r^3}{4} \end{bmatrix} \times \begin{bmatrix} A \\ A(\xi - 2)\sin\psi \\ d_2 \\ Ad_2 \\ 1 \end{bmatrix} = \begin{bmatrix} F_x \\ F_z \\ M_y \end{bmatrix} \quad (5.24)$$

Figure 65 shows F_x , F_z and M_y versus the constant A for various values of ξ for a water droplet placed on a vertical solid surface and $\gamma = 0.072 \text{ N/m}$. It was assumed that $\theta_0 = 60^\circ$, $P_L = 144 \text{ Pa}$, $r = 2 \text{ mm}$, $d_1 = 1$ and $d_2 = 1 \text{ mm}$.

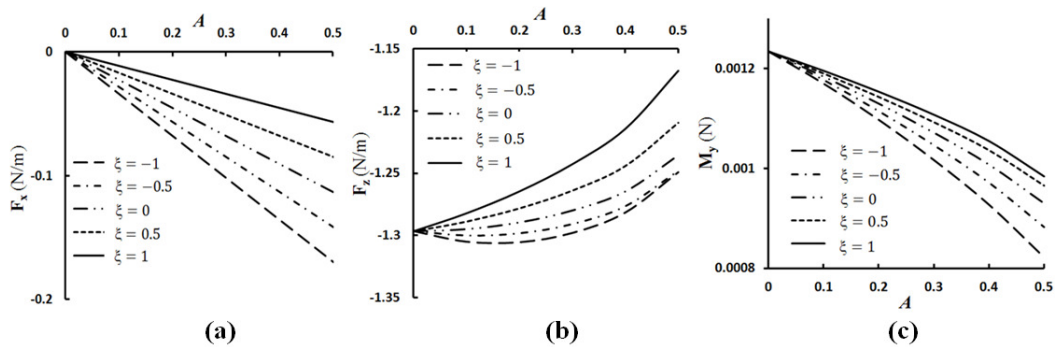


Figure 65. Force and moment versus A . (a) F_x versus the constant A for various values of ξ (b) F_z versus the constant A for various values of ξ (c) The moment versus the constant A for various values of ξ and $\gamma=0.072 \text{ Jm}^{-2}$ for $\theta_0=60^\circ$, $\psi=90^\circ$, $P_L=144 \text{ Pa}$ and $r=2$, $d_1=1$, $d_2=1 \text{ mm}$ (Hejazi et al., 2013).

5.2.2. Ice

To write the balance equations of forces, one has to consider the shear force applied to the solid-ice interface due to the weight of ice (Figure 64d). Considering the shear force applied to the solid-ice interface, the balance equations of force are given as

$$F_x + \beta \int_0^{2\pi} \gamma_x d\alpha - \delta \pi \tau_{xz} r = 0 \quad (5.25)$$

$$F_y + \beta \int_0^{2\pi} \gamma_y d\alpha + \delta \pi \tau_{yz} r = 0 \quad (5.26)$$

$$F_z + \beta \left(\int_0^{2\pi} \gamma_z d\alpha + r \int_0^{2\pi} p(x) \cos^2 \alpha d\alpha \right) + \delta \pi \tau_{zz} r = 0 \quad (5.27)$$

where τ_{yz} is the shear stresses between ice and the solid surface applied in y direction. The value of τ_{yz} is zero due to symmetry. β and δ are the coefficients which determine the phase of deposited object so that for water $\beta = 1$, $\delta = 0$ and for ice $\beta = 0$, $\delta = 1$. Equations (5.25), (5.26) and (5.27) can be applied to both water and ice deposited on the solid surface.

The balance equations of forces for ice particle on a tilted surface are

$$F_x = \pi \tau_{xz} r \quad (5.28)$$

$$F_y = 0 \quad (5.29)$$

$$F_z = \pi \tau_{zz} r \quad (5.30)$$

The balance equation of the moment of ice about the point O at the center of the solid-ice interface (Figure 64d) is given by

$$M_y = F_x d_1 - F_z d_2 = \pi r (\tau_{xz} d_1 - \tau_{zz} d_2) \quad (5.31)$$

where τ_{xz} is the shear stresses between ice and the solid surface applied in x direction. τ_{zz} is the distributed normal stress which balances the torque created by the shear force F_x applied at the offset d_1 .

Equations of the balance of forces and the moment for ice placed on vertical surfaces in matrix form can be given as

$$\begin{bmatrix} \pi r & 0 & 0 \\ 0 & \pi r & 0 \\ 0 & 0 & \pi r \end{bmatrix} \times \begin{bmatrix} \tau_{xz} \\ \tau_{zz} \\ \tau_{xz} d_1 - \tau_{zz} d_2 \end{bmatrix} = \begin{bmatrix} F_x \\ F_z \\ M_y \end{bmatrix} \quad (5.32)$$

5.3. Experimental study

5.3.1. Adhesion strength of ice

We experimentally studied the adhesion strength of ice on four metallic samples of aluminum, copper, brass 84400, stainless steel, and four non-metallic samples of nylon 6.6, nylon6.6 + glass fiber, co-polypropylene (PP+PE) and TiO₂ coated tile and also measured the CA hysteresis of water droplet on the same samples as well as the surface roughness (with Phase II Surface Roughness Tester SRG-4500) for all samples except the tile, which was above the resolution (Table 8). The experiments were repeated 3 times for each sample and the error bars show the variation of these data.

The most common method to measure ice adhesion to the surface is applying a compressive or tensile force resulting in shear stress on the ice confined between two surfaces. Cylindrical or rectangular ice samples can be used. In order to measure the

adhesion force of ice to different materials, we used a PASCO stress/strain apparatus 750 interface equipped with an economy force sensor (PASCO CI-6746, Figure 66a). The DataStudio software was used to record and analyze the data. We used various samples as the substrates and let the water being frozen on them using a plastic cylindrical mold. The sample was placed in the apparatus and the horizontal shear force was applied to the base of the ice column through a ring set around the ice and by rotating the apparatus handle until the ice was separated from the substrate (Figure 66b). The dependency of the force vs. the time of deformation (approximately proportional to the displacement) was recorded by the computer (Figure 66c).

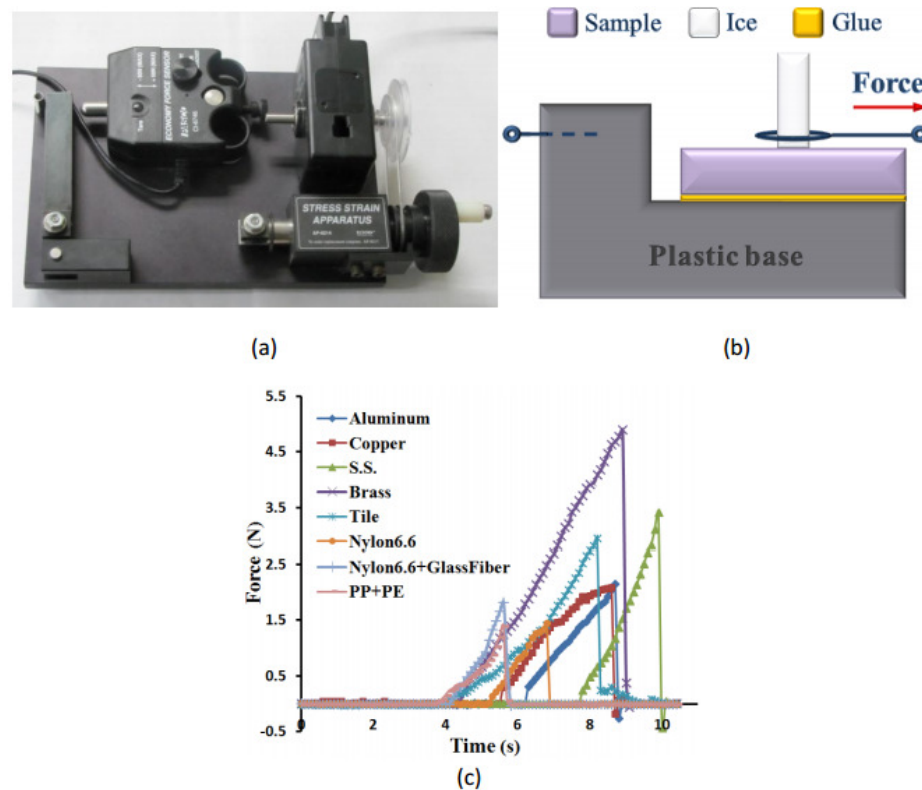


Figure 66. Schematic of the apparatus (a) PASCO stress/strain apparatus (b) Horizontal force applied to the ice column (c) Force versus time of deformation. Color lines show the applied forces to the ice on various substrates versus time (Hejazi et al., 2013).

We prepared eight samples. The metallic samples were polished with a soft cloth impregnated with 1 μm silica and then were washed and cleaned with deionized water and finally were air dried. In order to freeze water column on substrates surface, thin tubes of plastic cut from a common drinking straw with 5 mm inside diameter and 10 mm height were used as molds. The plastic molds were placed vertically on substrates surface and a Permatex black silicone sealant was gently applied to the outside surface of mold's base on substrates to prevent water leakage. The molds were then filled with water using a syringe and left inside the freezing room at -20°C until the water was entirely frozen, and then the sealant was removed.

In order to measure the force applied to the ice column, each sample was transferred separately to the other freezing room with the temperature of -5 to -1°C where the stress/strain apparatus was located. Then the horizontal shear force was applied to the base of the ice column until it was separated from the substrate (Figure 66b). The magnitude of the applied force was recorded in a laptop located outside the freezing rooms using the DataStudio software. In order to investigate the wetting behavior of above-mentioned samples, the static advancing and receding water CAs were measured using a ramé-hart 250 goniometer/tensiometer (Table 8).

Table 8. Water CAs of the samples and shear strength of the ice.

Material		Max. Force (N)	Roughness (μm)	Strength (kPa)	Water CA $^{\circ}$	Adv. CA $^{\circ}$	Rec. CA $^{\circ}$	CA hysteresis $^{\circ}$
Metallic	Aluminum	2.16	0.6	110	78.01	78.39	74.33	4.06
	Copper	2.1	0.076	106.95	85.26	88.34	84.41	3.93
	Brass	4.95	0.047	252.1	83.8	84.87	76.38	8.49
	S.S.	3.41	0.32	173.67	83.57	87.22	81.99	5.23
Non-Metallic	Tile	2.99	>10	152.28	111.38	113	103.21	9.82
	Nylon6.6	1.46	0.058	74.36	74.34	76.79	73.14	3.65
	Nylon6.6+GF	1.86	0.7	94.73	73.43	75.71	71.85	3.86
	PP+PE	1.41	1.19	71.81	77.85	78.1	76.66	1.44

Our study showed that the highest CA corresponds to the tile in non-metallic samples which also has the highest shear strength of ice (Table 8). It shows that the superhydrophobic or hydrophobic materials are not necessarily icephobic. However, the opposite behavior is observed in metallic samples. The highest CA corresponds to the copper which has the lowest shear strength of ice (Figure 67). This can be attributed to the various ranges of surface energy as well as the different surface roughness that these materials possess. The lowest CA hysteresis is on the PP+PE in non-metallic samples and copper in metallic samples which both have the lowest adhesion strength to the ice.

As far as the correlation of the shear strength with surface roughness, it is observed from Table 8 that smoother samples tend to correspond to higher strength, which can be attributed to lower probability of interface void and crack formation in these samples.

The results show that CA hysteresis correlates with the ice adhesion strength on the hydrophilic samples (Figure 67). However, for the adhesion strength did not correlate with the receding contact angle, as it was described in the literature earlier (Meuler et al., 2010a; Meuler et al., 2010b; Nosonovsky & Hejazi, 2010) but rather low adhesion strength correlated with low CA hysteresis. This can be explained by considering the effect of surface roughness so that the rougher surfaces may have lower or higher receding CA depending on where the triple point is located.

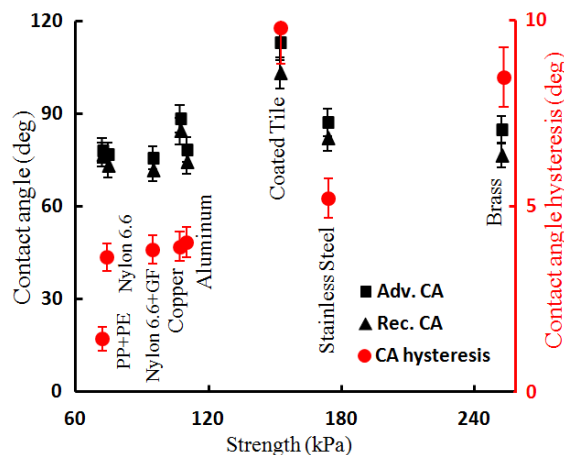


Figure 67. Contact angle and contact angle hysteresis. Right axis shows the data corresponding to CA hysteresis (Red dots) and left axis shows the data related to advancing and receding CA (Black squares and triangles).

The results affirm that the CA hysteresis and the adhesion strength of ice to the samples are approximately proportional (linear) for hydrophilic surfaces (Figure 67). This is because the materials with higher surface energy have the higher CA angle hysteresis which results in higher adhesion strength of ice to the samples. The results also reveal that the icephobicity for hydrophilic surfaces do not follow the governing energy law for the Mode I (during the crack opening only energy of separation corresponding to receding CA matters) but it is more precisely related to low CA hysteresis rather than receding CA or superhydrophobicity.

5.3.2. Concrete-ice adhesion strength

To measure the adhesion strength of ice to concrete materials, we prepared 6 cubic concrete samples with 2 different compositions of W_1 and W_2 with sand to cement ratio (S/C) of 2.75, as well as water to cement ratio (W/C) of 0.5 and 0.7, respectively.

Samples were cast and compacted using a vibrating table at 150 Hz for 20 seconds, then allowed to harden for 24 hours at 23 ± 3 °C and at least 90% of relative

humidity. After 24 hours, samples were de-molded and the surface was roughened with a silicon carbide grinding paper with a grit of 320 for 1 minute in order to expose the fresh surface and sand aggregates. A soft brush and water were used to remove any loose particles from the tile surface. Samples were allowed to dry for 24 hours at 40 ± 2 °C and after this were exposed to room conditions for 24 hours.

The samples were split into 2 equal pieces using a compression set-up (Figure 69b). Three broken samples of each composition type were coated with hydrophobic solution by immersing into the PHMS emulsion for 20 seconds. Coated samples were dried at a room temperature for 48 hours. After that samples were placed into the cubic mold and water was poured into the half empty space of the mold. Molds were placed in the freezing room at the temperature of -20°C until the water was completely frozen. Then the samples were de-molded (Figure 68).



Figure 68. Coated and non-coated ice-concrete samples.

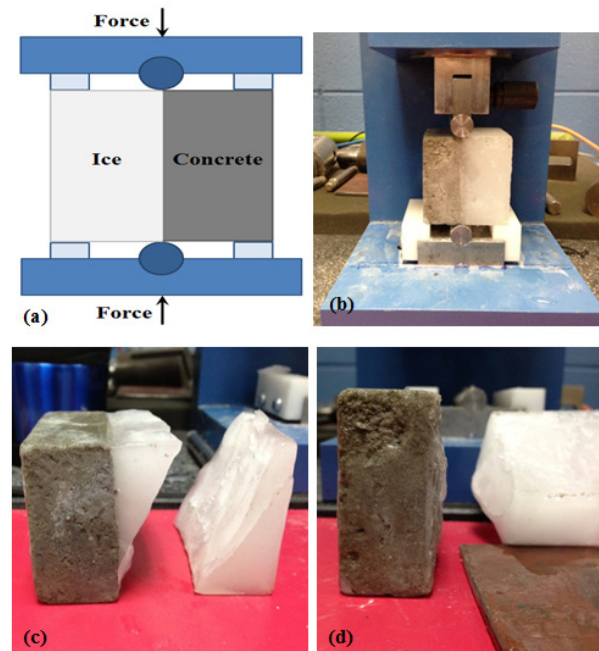


Figure 69. Schematic of the compression test set-up (b) compression test set-up (c) broken ice on non-coated concrete (d) broken ice on coated concrete.

In order to measure the adhesion strength of ice to the concrete samples, a compression set-up was prepared (Figure 69b). the vertical force was applied to the border of ice-concrete samples till the ice was separated from the concrete (Figure 69a). Figure 69c, d show the broken ice particles after the compression experiments.

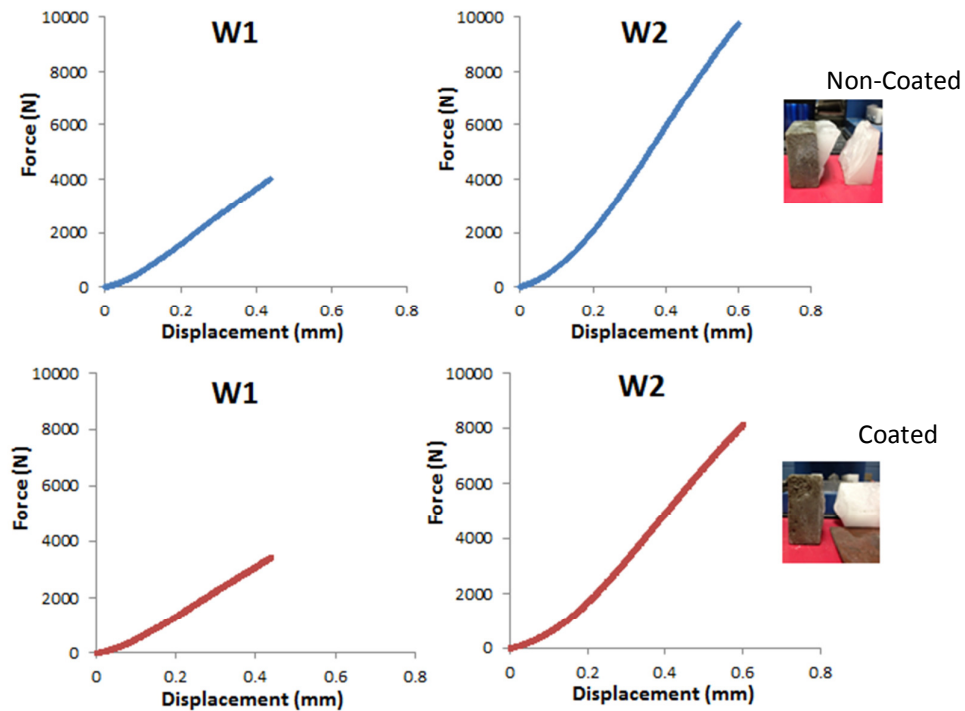


Figure 70. Force versus displacement for coated and non-coated concrete samples.

Figure 70 illustrates the adhesion force of ice to the coated (lower row) and non-coated (upper row) concrete samples with different compositions of W_1 and W_2 versus the displacement. Comparing the data and graphs shown in this figure reveals that there is not considerable difference between the adhesion strength of ice to the coated and non-coated samples. This demonstrates although applying hydrophobic coating on the surface slightly decrease the adhesion strength of ice to it, in general, superhydrophobic surfaces do not necessarily show the anti-icing properties.

5.3.3. Water impact test

Besides the parallelism between the dewetting and deicing, the effect of impacting water droplets on superhydrophobic surfaces below the water freezing temperature was investigated. A superhydrophobic surface was produced by coating glass substrate by soot. The water CA with the soot coated glass was 127° . The surface was kept for 5 minutes in the freezing room at -22°C . A syringe filled with tap

water at $3\pm 2^\circ\text{C}$ was used to drop the water on the substrate from the height of about 5 cm. The volume of each droplet was about 7 ml. It was observed that the droplets did not stick to the substrate, but jumped off the surface (Figure 71). Thus, the ability of a superhydrophobic surface to bounce off incoming droplets reduces the time of contact with the solid, so that there is not enough time for water droplet to freeze. The results demonstrated some correlation between the hydrophobic and icephobic properties as defined in terms of local adhesion forces and the effect of incoming water droplet.

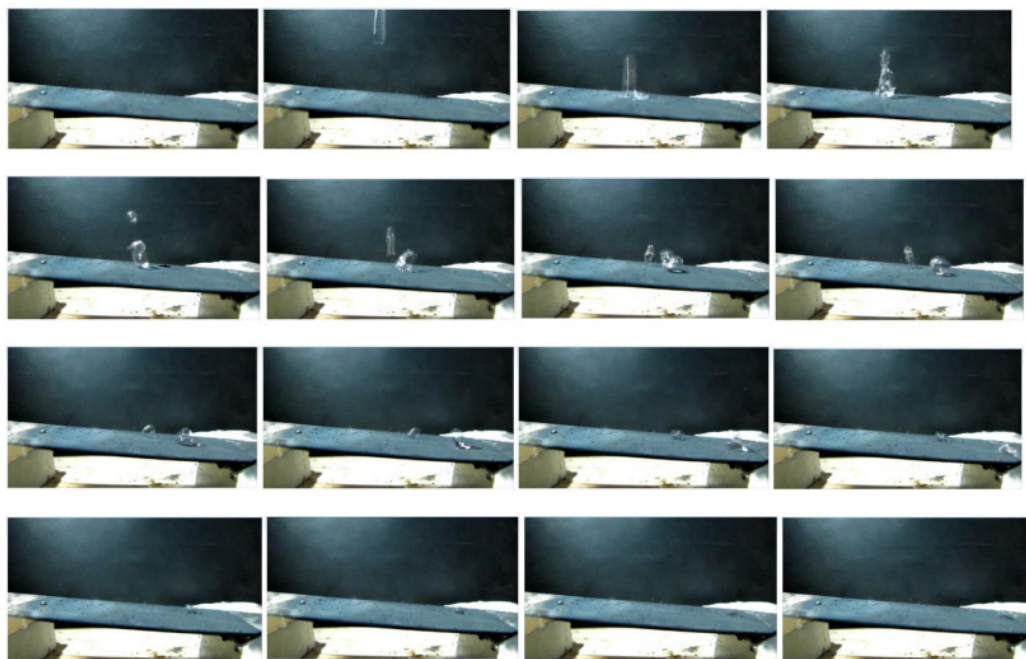


Figure 71. The water droplet jumped off a tilted glass substrate coated by soot at -20°C (Hejazi et al., 2013).

5.4. Icephobicity of superhydrophobic surfaces

In several recently published papers published (Meuler et al., 2010a; Meuler et al., 2010b; Zheng et al., 2011; Jung et al., 2011; Kulinich et al., 2011; Bahadur et al., 2011; Cao et al., 2009; Kulinich and Frazaneh, 2009; Dotan et al., 2009; Menini et al., 2011; Farhadi et al., 2011; Wong et al., 2011; Yang et al., 2008; Nosonovsky and Bhushan, 2008e), it was suggested that surface-roughness-induced

superhydrophobicity can be used to design icephobic or anti-icing coatings. The assumption behind this suggestion was that mechanisms of ice and water adhesion are similar, and therefore, by designing a surface with low surface energy (large water contact angle), one can achieve also weak adhesion between the surface and ice. However, the mechanisms of water and ice adhesion are different. Water can withstand pressure, either positive (compressive) or negative (tensile) (Nosonovsky and Bhushan, 2008e; Nosonovsky, 2011), but it cannot support shear stress since the stress tensor τ of liquid is spherical in the static limit ($\tau_{xy} = 0$).

The situation changes when the droplet freezes. Ice can support shear load τ_{xy} and a distributed normal stress τ_{yy} , which balances the torque created by the shear force F_x applied at the offset d . However, ice detachment from a solid surface occurs through fracture, and therefore, it is different from the dewetting mechanism. Fracture can occur within the ice itself when the interface with the substrate is strong or at the substrate-ice interface if defects (e.g., cracks) are present (Raraty & Tabor, 1958). Fracture occurs in accordance with the mode I (opening) or mode II (edge sliding) cracking scenarios, which correspond to normal and shear loading (Anderson, 1995). The critical strength above which the fracture occurs in mode I is given by

$$\tau_{yy} = \sqrt{\frac{EG}{\pi a}} \quad (5.33)$$

where E is the Young modulus, G is the surface energy of the crack, and a is the crack length. The analysis for mode II crack fracture is similar. Typically, it is assumed that the surface

energy has a constant value $G = \gamma_{SA} + \gamma_{IA} - \gamma_{SI}$, where γ_{IA} and γ_{SI} are the ice-air and solid-ice interfacial energies. However, a more detailed analysis shows that the value of surface energy depends on whether it is measured during the approach of two

surfaces or during their separation. This is because of the so-called adhesion hysteresis (Israelachvili, 1992). The energy needed to separate surfaces is greater than that gained by bringing them together. This can be described by the physical bonding between two surfaces during their contact. Adhesion hysteresis is related to CA hysteresis, so that the former is one of the underlying causes of the latter (Nosonovsky & Bhushan, 2008c). Note the analogy with the Young equation

$$G = \gamma_{IA}(1 + \cos \theta) \quad (5.34)$$

where $\cos \theta = (\gamma_{SA} - \gamma_{SI})/\gamma_{IA}$. If the interfacial energies of two phases of water are close to each other, $\gamma_{IA} \approx \gamma_{WA}$ and $\gamma_{SI} \approx \gamma_{WI}$, then the values of θ for water and ice are also comparable

and thus superhydrophobicity corresponds to a high value of θ for ice. During the detachment of the solid surfaces or opening the crack, the energy of separation matters, which is related to the receding CA, as opposed to the energy of bringing the surfaces together, which is related to the advancing CA. Therefore, when the crack is opening, only the receding value matters, $G_{rec} = \gamma_{IA}(1 + \cos \theta_{rec})$. The critical stress is related to the receding CA as

$$\tau_{yy} = \sqrt{\frac{EG_{rec}}{\pi a}} = \sqrt{\frac{E\gamma_{IA}(1 + \cos \theta_{rec})}{\pi a}} \quad (5.35)$$

From equation (5.35), we conclude that (i) shear strength correlates with the receding contact angle; (ii) superhydrophobic surface has low shear strength because high CA, $\theta_{rec} \rightarrow 180^\circ$, corresponds to low values of $(1 + \cos \theta_{rec})$; and (iii) the effect of initial crack size is very significant. Thus, for the values of $E = 9.7$ GPa, $\gamma_{IA} = 0.109$ N/m (Petrovic, 2003), $\cos \theta_{rec} = -0.9$, and $a = 100$ μm , the shear strength is $\tau_{yy} = 58$ kPa.

For an ice particle with the contact area of 1 mm^2 , this corresponds to the shear force of 58 mN, which is about 4 orders of magnitude larger than for a droplet.

For a superhydrophobic surface with the same properties but smaller cracks of $a = 1 \mu\text{m}$, the force will be 580 mN. For hydrophilic surfaces, roughening the surface can increase its adhesion to ice, as water penetrated the cavities between the asperities. However, most superhydrophobic surfaces are in the so-called Cassie state, with air pockets trapped between the solid and water droplet. When water freezes, the pockets become air voids and they can serve as stress concentrators. While superhydrophobic surfaces can be beneficial to prevent ice formation through condensation of water droplets, ice shedding should be targeted for robust icephobicity. It is therefore desirable to have a surface that supports both the Cassie superhydrophobic regime and crack formation in ice. In addition, many superhydrophobic surfaces have dual tier roughness; however, the effect of dual tier on ice adhesion shedding should be investigated separately.

5.5. Discussion

Our results are consistent with the concept of the parallelism between the definitions of the superhydrophobicity and icephobicity (Table 9). Thus, the requirement of low surface energy and high CA for superhydrophobic surfaces corresponds to low solid-ice adhesion and low normal strength in the icephobicity. Low CA hysteresis corresponds to shear loading and thus to low shear strength in icephobic surfaces. The condition of bouncing-off incoming droplet is similar in superhydrophobicity and icephobicity. Finally, delayed crystallization of ice corresponds to the “antifogging” property of superhydrophobic surfaces.

Table 9. The comparison of the hydrophobicity and icephobicity.

Property	Water	Ice
Definition of "phobicity"	Low surface energy/low adhesion High contact angle Low CA hysteresis Bouncing-off	Low adhesion Low normal strength (maximum stress) Low shear strength Bouncing-off supercooled droplets
Interaction Thermodynamic relationship	Hydrophobic interaction Minimization of $\Delta G = \Delta H - T\Delta S$	Crystallization of ice and snowflakes Surface roughening transition $\Delta G = \Delta H - T\Delta S = 0$ and similar
Typical manifestation of the interactions	Hydrocarbone molecules in water environment	Ice molecules in saturated vapor environment at negative temperatures
Effects	Protein folding (including fractal shape), self-organized criticality, long-range hydrophobic force, wetting transitions	Snowflakes (diverse but symmetric, fractal)

All these features should be considered for a universal and robust definition of the icephobicity (Moret and Zebendeh, 2007). We therefore, suggest that a surface should be called icephobic if it delays ice formation from condensed or incoming water in the situation where normally ice would form (i.e., negative temperature, saturated vapor) and/or if it has weak shear and normal adhesion strength to ice (e.g., lower than 100 kPa).

Besides wetting, hydrophobicity is crucial for many important effects, such as the "hydrophobic effect" and hydrophobic interactions. For two hydrophobic molecules (e.g., hydrocarbons) placed in water, there is an effective repulsive hydrophobic force due to their interaction with the water medium. The hydrophobic effect is responsible for folding of proteins and other macro-molecules (Kauzmann, 1959; Figure 72a). A special type of self-organized behavior, so-called self-organized criticality (SOC), may result from hydrophobic folding of proteins which is evidenced by power law exponents of the accessible surface area correlated with the hydrophobicity scales in protein amino-acids (Boinovich & Emelyanenko, 2013; Phillips, 2009). SOC is the major mechanisms with creates complexity in many systems and it has a specific "signature" on the quantitative characteristics of the system, such as the "one-over-frequency" noise, power exponents and fractalness (Bak et al., 1987). Protein folding is a typical example of hydrophobically self-organized criticality.

Are there any effects with similar signature related to the icephobicity? An obvious candidate is snowflake crystallization. Snowflakes are known to have fractal shape. Furthermore, their shape is very diverse with “no two flakes similar to each other.” On the other hand, many snow crystals are symmetric with each of the six branches almost identical to other five branches (Figure 72b). The perceived “synchronization” of branch growth is stipulated by the history of the flake formation. The snow crystals grow in oversaturated vapor under negative temperatures, whereas the direction of their crystal growth is very sensitive to the variation of the temperature T and humidity (or oversaturation density ρ) varying from prisms to thin, solid, and sectorized plates to dendrites to needles and columns. Each of these shapes is characterized by a fractal dimension $D(T, \rho)$. When a snowflake falls, it passes through a unique history of temperature $T(t)$ and humidity $\rho(t)$ which defines the unique shape of a branch, however, similar for all six branches of the crystal. This is because the lattice of the ice crystal corresponds to a hexagonal close-packed (HCP) arrangement of molecules. While perhaps one can speak about the “icephobic interaction” only in a metaphoric sense, the essence of the effect – the apparent “synchronization” of remote branches due to the interaction with the medium (oversaturated vapor) – is somewhat similar to the hydrophobic effect – the apparent repulsion of the hydrophobic particles due to their interaction with the medium (water). Furthermore, both effects can lead to quite complex phenomena, such as SOC-driven complexity as a result of hydrophobic interactions (during wetting of rough/heterogeneous surfaces or during polypeptide chain folding and looping (Boinovich and Emelyanenko, 2013; Phillips, 2009)) or ice crystallization (fractal snowflakes) (Nosonovsky and Bhushan, 2008f).



Figure 72. Parallelism of hydrophobic interaction and ice formation (a) The attractive force between hydrophobic molecules (hydrocarbons) is a result of Gibbs energy $\Delta G = \Delta H - T\Delta S$ minimization due to entropy increase ΔS in water molecular network (hydrocarbon-water- hydrocarbon system) prevailing over enthalpy ΔH (b) The synchronization of branch growth during formation of a snow crystal due to ΔS prevailing over ΔH (ice-saturated vapor-ice system) (Hejazi et al., 2013).

Note that thermodynamically both the hydrophobic interactions and ice formation are driven by the minimization of the Gibbs surface energy, $\Delta G = \Delta H - T\Delta S$. This is because in the hydrophobic interactions large positive value of $T\Delta S$ prevails over a small positive value of ΔH making spontaneous hydrophobic interaction energetically profitable (Nosonovsky and Bhushan, 2008f). The so-called surface roughening transition (Furukawa, 2007) governs the direction of ice crystal growth and occurs at the critical temperature (depends on epitaxy), above which the entropic contribution into the Gibbs energy, $T\Delta S$, prevails over the enthalpic contribution, ΔH , thus making it more energetically profitable for the ice crystal to be rough rather than smooth (Furukawa, 2007). This suggests that thermodynamically both the icephobic and hydrophobic behaviors can be viewed as entropic effects.

5.6. Conclusion

In conclusion, we investigated the parallelism between the hydrophobicity and icephobicity and suggested a definition of icephobicity which combines various requirements for anti-icing surfaces, namely, weak adhesion with the solid substrate

and the ability to repel incoming droplets. We conducted a comparative study of wetting and anti-icing behavior. The theoretical force analysis shows that the main parameter affecting droplet adhesion to a solid surface is CA hysteresis, while for ice particles both receding CA and the size of voids/defects are important (Eqs. 5.34 & 5.35). However, in practice ice adhesion does always not correlate with the receding CA or with CA hysteresis. This parallelism between the hydrophobicity and icephobicity is in how these phenomena are defined: the key parameters are the normal and shear strength for icephobic surfaces and the CA and CA hysteresis for hydrophobic surfaces. Furthermore, the thermodynamic descriptions of the hydrophobic interaction and icephobicity may be similar. This is because both of them depend on the entropic term, $2T\Delta S$, in the Gibbs free energy which dominates over the enthalpic term, ΔH , during the hydrophobic interaction and also governs the roughening transition during ice formation. The effects of the hydrophobic interactions and icephobicity are also similar since both can involve the self-assembly of new structures such as snow crystals or complex molecules (e.g., protein folding). Therefore, besides the practical application of the icephobicity to design novel ice-repellent surfaces, the phenomenon is also of interest from the theoretical point of view.

CHAPTER SIX

6. CONCLUSION

The standard method to design superhydrophobic surfaces implies roughening the surface and applying hydrophobic coating on it. In our research, we suggested introducing hydrophobic reinforcement into the bulk of the composite material rather than only at its surface.

In chapter two, we developed a theoretical model to predict the overall contact angle of such a composite material and then solved the equation for the reinforcement volume fraction needed to make the material superhydrophobic. We also conducted experiments with low-energy graphite-reinforced Al- and Cu-matrix composites and showed that the contact angle can be obtained from the model with appropriate assumptions of the roughness factors and solid-liquid fractional contact areas. In order to decouple the effects of reinforcement and roughness, the experiments were conducted for initially smooth and etched matrix and composite materials. Although the experiments did not demonstrate the superhydrophobicity, the distinct difference between the wetting properties in composite materials and base alloys was found only in Cu-based samples. This is due to a combination of the optimized surface roughness as well as the low surface energy of Cu-based material. Furthermore, for these samples, we observed a decrease of the contact angle. The experimental data showed that the CU-based MMCs are in the Cassie-Baxter wetting regime, which is required for superhydrophobicity. We concluded that decoupling of the effects of roughness and composition is promising and shows that Cu-based MMCs have the potential to be used in the future to synthesize durable superhydrophobic surfaces.

We studied the CA hysteresis, measured as a difference between the advancing and receding CAs, and showed that is an important parameter to characterize wetting of a solid surface by a liquid. Our results revealed that the CA hysteresis exists not only in two-phase solid-water and three-phase solid-water-air systems, but also in solid-oil and solid-oil-water and solid-oil-water-air systems. We experimentally studied CA hysteresis in two types of solid-water-air systems: first with water droplets in air and second with air bubbles in water against the same metal samples. Although the solid-water-air triple line is the same in these two systems, the adhesion of water droplets was significantly stronger, which indicates the role of the 2D interface. The hysteresis with the oil droplet was weaker than with air bubbles and water droplets, which indicates that weaker dispersion forces were involved in that system.

In chapter three, we investigated the technology of hydrophobic emulsions and their application on portland cement mortar tiles. To optimize the design of hydrophobic emulsions, we developed a model and a relationship between the droplet size and the size of irregularities on the surface of coating. We examined the wetting properties of coated concretes versus non-coated concretes by developing new theoretical models. An optimized distance between the aggregates where the CA reaches to its highest value was predicted based on proposal models. The effect of hierarchical roughness of concrete surface on CA was theoretically investigated.

The proposed emulsion types were successfully realized by using different mixing procedures. Wetting of mortar tile surfaces by water was experimentally investigated. The highest water-repellency corresponded to the samples coated with the MK2 solution due to its microroughness and hydrophobization. In general, we

reported a method to produce over-hydrophobic concrete with water CAs approaching the superhydrophobicity values.

In chapter four, we studied the wetting transitions for two-, three-, and four-phase interface of MMCs. We developed models for three- and four-phase rough interfaces, which can be generalized for an arbitrary number of phases. We showed that the wetting transitions can be treated as a phase transition using a phase field model on the multi-phase interfaces. We investigated wetting transitions on a modeled patterned surface and reported observations of wetting transitions on solid-oil-water interfaces. Such interfaces can be used for the design of bio-inspired underwater self-cleaning, oleophobic and antifouling surfaces mimicking antifouling properties of fish scale.

We also investigated wetting of rough Brass surfaces by water and oil in air as well as oil in water. An abrupt increase of the contact angle for the oil underwater system was observed. We showed that the increase cannot be explained by the standard Wenzel and Cassie-Baxter models; however, it is consistent with the wetting regime change (wetting transition) from Wenzel to Cassie-Baxter. Although such wetting transitions are known for superhydrophobic surfaces, it was the first time such a transition for wetting of a rough surface with an organic non-polar liquid was reported.

In chapter five, we suggested a definition of icephobicity which combines various requirements for anti-icing surfaces, namely, weak adhesion with the solid substrate and the ability to repel incoming droplets. We also studied the hydrophobicity versus icephobicity and showed how they are different. We conducted a comparative study of wetting and anti-icing behavior. We presented a theoretical model to analyze the force interactions of a water droplet and an ice particle with a

solid substrate upon which they are deposited. The model showed that the main parameter affecting droplet adhesion to a solid surface is CA hysteresis, while for ice particles both receding CA and the size of cracks are important. However, in practice ice adhesion does always not correlate with the receding CA or with CA hysteresis. This parallelism between the hydrophobicity and icephobicity is in how these phenomena are defined: the key parameters are the normal and shear strength for icephobic surfaces and the CA and CA hysteresis for hydrophobic surfaces.

APPENDIX

Materials and experimental procedure

In this section we present the experimental assessment of the hydrophobicity of mortar surfaces using different emulsion concepts (the so-called “simple”, “core,” and “shell” emulsions). Optical and Scanning Electron Microscope (SEM) were used to characterize the emulsions and coating treatment. The droplet size, the surface profile, along with the CA, were used as parameters to model the hydrophobicity of the specimens coated with single- and double- layers of hydrophobic emulsions; these models were compared with experimental results.

For emulsion stabilization, water soluble polyvinyl alcohol (PVA) was selected because of its nonionic character and perfect compatibility with concrete materials (Kim *et al.* 1999). A highly hydrolyzed (98%) PVA with molecular weight of 16,000 from Across Chemicals was used to reduce the tendency of foam formation. Deionized water (DI water) was used as the dispersion medium for the emulsions. Polymethyl-hydrogen siloxane oil, PMHS (XIAMETER MHX-1107) from Dow Corning with a specific gravity of 0.997 (at 25°C) and a viscosity of 30 cSt was used as hydrophobic agent. This product contains 85-100% of methylhydrogen siloxane as an active agent. Metakaolin (MK) from Burgess Optipozz was added to the emulsions to induce the micro roughness. The SEM (Figure 73), as well as the X-ray diffraction (Figure 74) were used to analyze the morphology and phases of MK. Rough and flaky particles with sizes from 0.8 to 12 μm with a certain degree of agglomeration were found in metakaolin.

Mortar tiles were prepared using a commercial Type I portland cement (PC) from Lafarge. The chemical and physical properties and the X-ray diffraction of NPC are presented in Table 10 and Figure 74, respectively. The morphology of PC is

presented in Figure 73. ASTM C778-graded standard quartz sand with average particle size of 425 μm and tap water were used to produce mortar tiles.

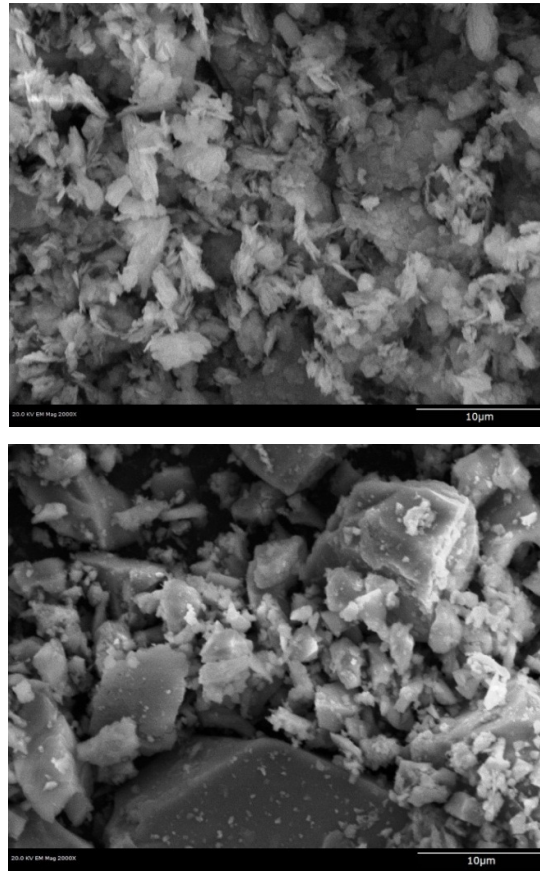


Figure 73. SEM images of metakaolin (left) and portland cement (right), (2000x magnification) (Flores et al., 2013).

CPS, A.U.

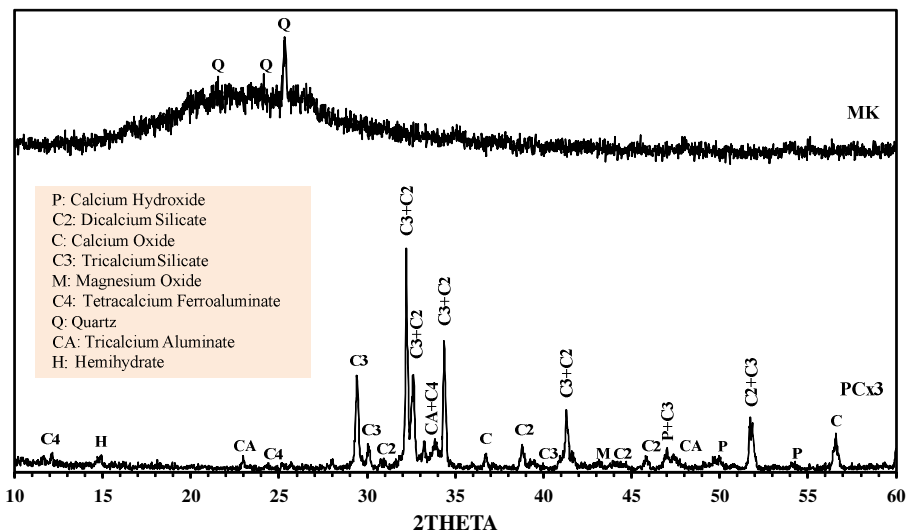


Figure 74. X-ray diffraction of MK (top) and PC (bottom) (Flores et al., 2013).

Table 10. Test results of portland cement Type I compared to ASTM C150 requirements.

CHEMICAL			PHYSICAL		
Item	Spec. Limit	Test Result	Item	Spec. Limit	Test Result
SiO ₂ , %		20.6	Air content, % (C-185)	12 max	7.5
Al ₂ O ₃ , %		4.7	Blaine fineness, m ² /kg (C-204)	260 min	380
Fe ₂ O ₃ , %		2.7	Autoclave expansion, % (C-151)	0.8 max	0.02
CaO, %		63.9	Compressive strength, MPa		
MgO, %	6.0 max	2.3		1 day	12.4
SO ₃ , %	3.0 max	2.4		3 days	12.0 min
Ignition loss, %	3.0 max	2.1		7 days	19.0 min
Ins. residue, %	0.75 max	0.36	28 days	28.0 min	37.9
Free lime, %		1.1	Time of setting, minutes		
CO ₂ , %		1.3		Initial	45 min
Limestone, %		3.4	Final	375 max	225
CaCO ₃ in LS, %		93.0	Heat of hydration at 7 days, kJ/kg		411
Potential, %			Percent Passing 325 Mesh (C-430)		95.4
	C ₃ S		54.5		
	C ₂ S		17.9		
	C ₃ A		7.9		
	C ₄ AF		8.2		
	C ₄ AF+2(C ₃ A)		24.2		
C ₃ S+4.75(C ₃ A)		93.0			
Na ₂ O _{equi}	0.6 max	0.55			

Preparation of hydrophobic coatings

To prepare the emulsion, water was used as a dispersion medium, water-soluble PVA as surfactant and PMHS as the dispersion phase. Metakaolin was used to stabilize (Binks *et al.*, 2000, Aveyard *et al.*, 2003 and Ngai *et al.*, 2006) and modify the emulsion using three different approaches. Figure 75 represents the three differences between simple, “shell” and “core” emulsion concepts that were tested. The concentration of surfactant and siloxane was kept constant at 4.4 and 25%, respectively, by the weight of the emulsion. The water-soluble PVA swells quickly in water and then clumps together. To avoid clumping, it was gradually added to de-ionized water and stirred for 10 minutes at $23\pm 3^{\circ}\text{C}$, using a magnetic stirrer with a hot plate. Then, to achieve a complete dissolution, temperature was increased to $95\pm 2.5^{\circ}\text{C}$, and kept constant for 40 minutes while stirring. The solution was allowed to cool in a water bath until temperature of $23\pm 3^{\circ}\text{C}$ was achieved. The mixing procedure of PHMS and metakaolin in PVA solution is explained in Figure 76. High speed mixer (HSM, model LSM-A from Silverson) was used to prepare the emulsions. To stabilize the plain emulsions (without particles), a high speed/shear mixed at 10,000 rpm was used to produce the small droplet size. Medium speed (5000 rpm) was used only when particles were added. The emulsions were characterized by an optical microscope (Olympus BH-2) at 1000x magnification.

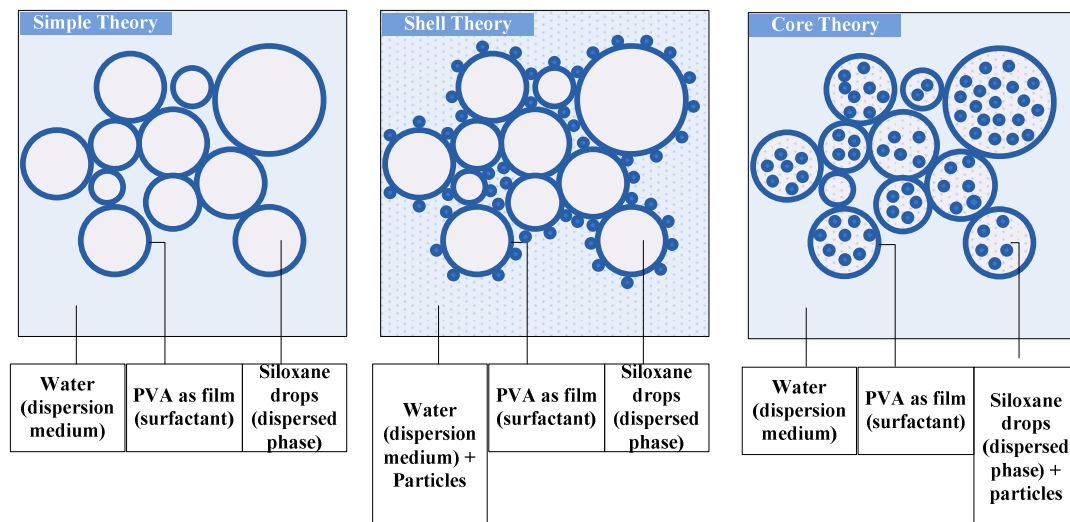


Figure 75. The explanation of simple, core and shell concepts used to design PMHS emulsions (Flores et al., 2013).

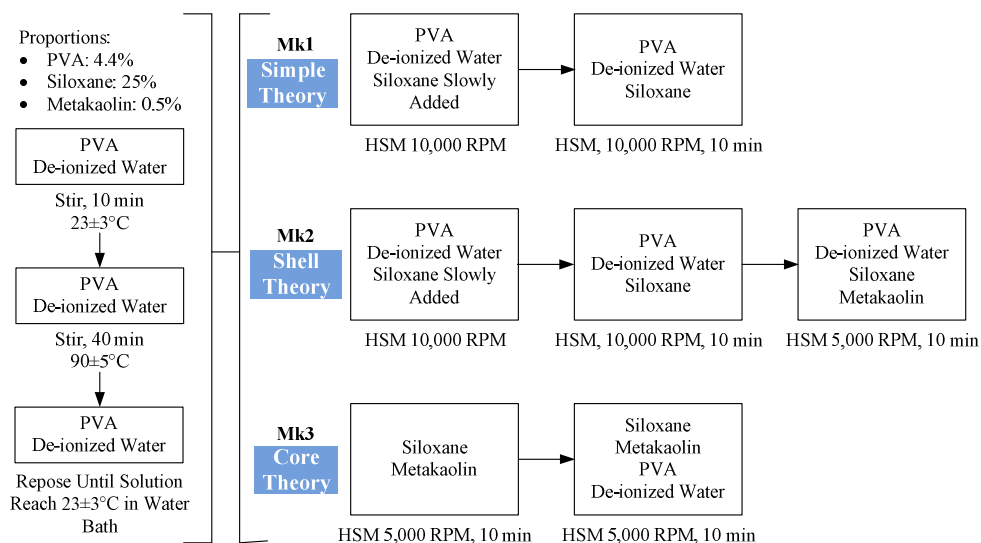


Figure 76. The procedure for preparation of PHMS emulsions (Flores et al., 2013).

Sample tile preparation

Standard mortar (ASTM C109) tiles of $10 \times 10 \times 5$ mm were prepared for test on hydrophobicity using water to cement ratio (W/C) of 0.5 and sand to cement ratio (S/C) of 2.75. Tiles were cast and compacted using a vibrating table at 150 Hz for 20 seconds. Tiles were allowed to harden for 24 hours at $23 \pm 3^\circ\text{C}$ and at least 90% of relative humidity. After 24 hours, tiles were de-molded and the surface was

roughened with a silicon carbide grinding paper with a grit of 320 for 1 minute in order to expose the fresh surface and sand aggregates. High porosity and scratches revealed on the specimens after this procedure. The porosity of non-covered specimens is shown at different magnifications in Figure 77. A soft brush and water were used to remove any loose particles from the tile surface. Tiles were allowed to dry for 24 hours at 40 ± 2 °C and after this were exposed to room conditions for 24 hours. The tiles were immersed into the PHMS emulsion for 20 seconds. Excess emulsion from the tiles was removed using a soft plastic spatula. Specimens were dried at a room temperature for 48 hours. This procedure was repeated when two coating layers were required.

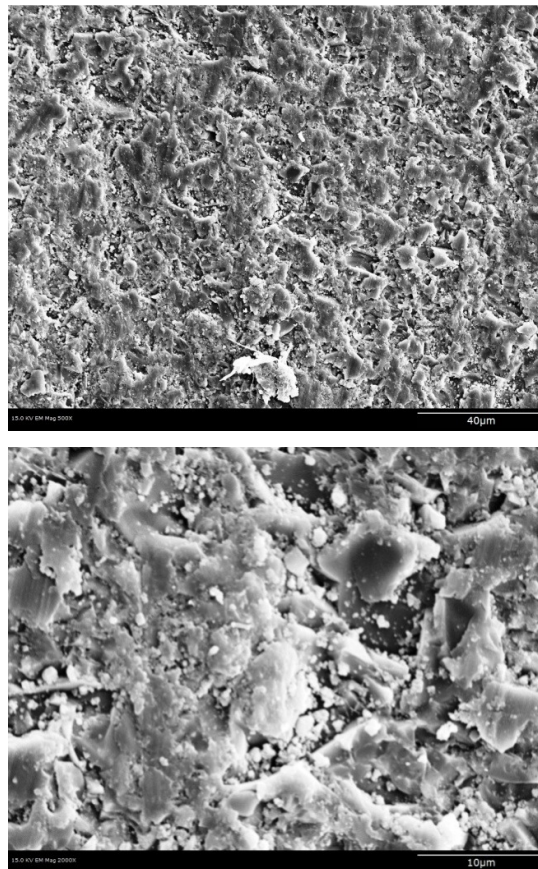


Figure 77. The surface of mortar tiles observed by SEM at 500x (left) and 2000x (right) magnifications (Flores et al., 2013).

Results and discussion

Characterization of coatings

The droplet sizes and the dispersion of metakaolin in the emulsions are shown in Figure 78. Emulsion Mk1 (Figure 78a) is mainly presented by uniform droplets of approximately 2 μm with few inclusions of larger droplets ($<20 \mu\text{m}$). Emulsion Mk2 (Figure 78b) is presented by well-distributed droplets with sizes from 3 to 30 μm . Particles of metakaolin were found on droplet boundaries. Emulsion Mk3 (Figure 78c) is mainly presented by well-distributed droplets with sizes from 2 to 5 μm with some inclusions of larger droplets ($<40 \mu\text{m}$). In this emulsion, the metakaolin particles were found to be embedded within the droplets.

These three emulsions successfully represent the proposed concepts detailed in Figure 75. The speed selected allows the formation of an emulsion with small droplets (Figure 78a), which is one of the key parameter for the stability of the emulsion (Charles Ross). Due to its hydrophilic surface (Barnes *et al.*, 2002 and Dhir *et al.*, 2003), metakaolin particles increase the coalescence of the emulsion during the mixing procedure, acting as an attraction force that combines the smallest droplets observed in Figure 78a, into bigger droplets observed in Figure 78b. Contrary to Mk2 emulsions, encapsulated particles of metakaolin in the oil-phase of Mk3 emulsion (Figure 78c), prevented the droplets from coalescence.

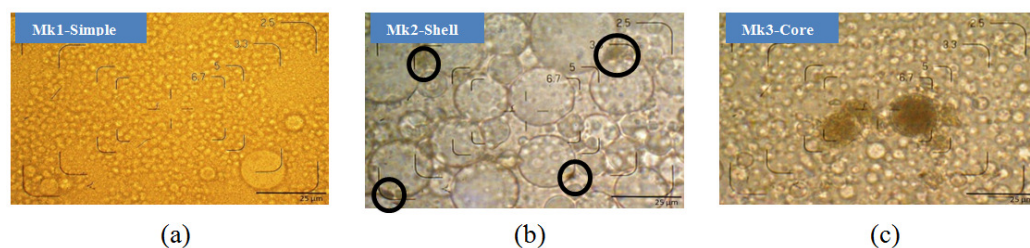


Figure 78. Emulsion images taken by optical microscope at 1000x magnification for: (a) Mk1; (b) Mk2; and (c) Mk3 (Flores *et al.*, 2013).

Two-layer superhydrophobic coatings were analyzed by SEM technique (Figure 79). The coating is directly related to the method that was used to produce the emulsions. Irregular surface structure is produced by collapsed bubbles with the size of 3 to 13 μm and by smaller bubbles of 1 to 2.5 μm as observed for Mk1 coating (Figure 79a). The collapsed bubbles are dominating in Mk1 sample, it can be concluded that the simple emulsion (Figure 75) had no capability of preserving the bubble structure on a surface resulting in the appearance of “moon craters”. The Mk2 coating (Figure 79b) appears to mimic the relief of the surface, leaving a uniform foam free self-assembled particle coating a “bump” size of 0.5 to 8 μm . The Mk3-core emulsion with incorporated particles allows the formation of “intact” bubbles reinforced by MK particles as a coating structure. Bubbles of 0.5 to 22 μm remained on the surface of the specimens and some collapsed bubbles of 1 to 19 μm can be observed on these coatings (Figure 79c). At higher magnification (Figure 79d), Mk2 surface reveals the bubble formation of the coating due to the first coating application. With the second application of Mk2 emulsion covers the voids left by the irregularities of the tile surface (Figure 77) and partially cover the bubbles and particles (Figure 79d).

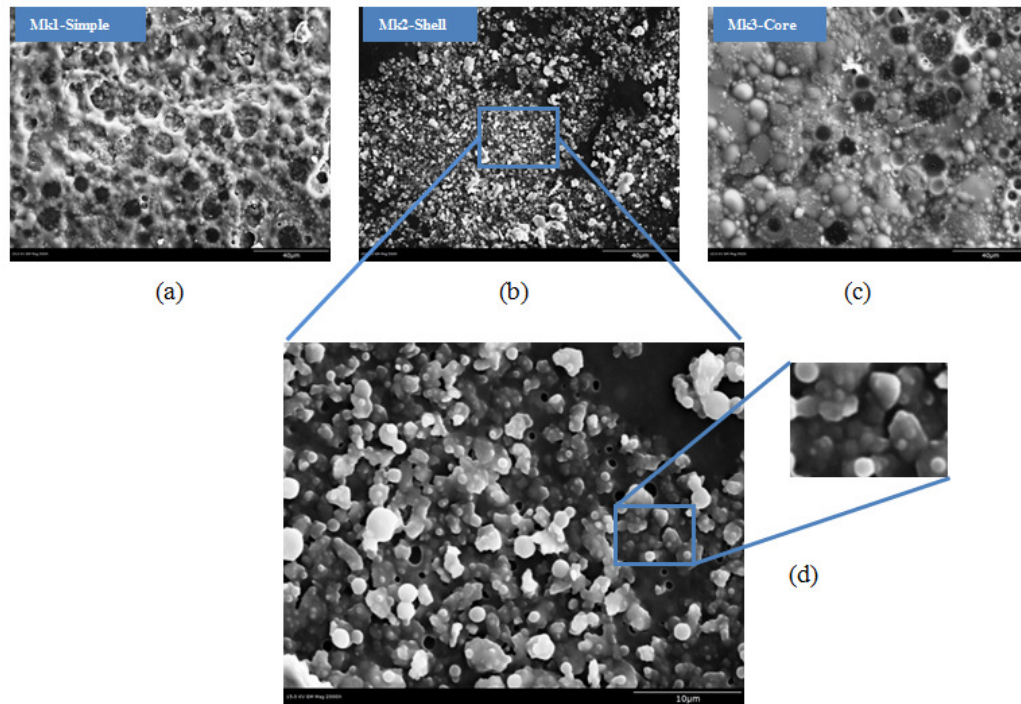


Figure 79. SEM images of superhydrophobic coatings at 500x magnification for: a) Mk1; b) Mk2; c) Mk3; and d) Mk2 at 2000x magnification (Flores et al., 2013).

REFERENCES

- Ablett, R., *Phil. Mag.*, 46, 224 (1923).
- Adam, N. K., and Jessop, G., *J. Chem. Soc.*, 127, 1863 (1925).
- Adamson A. V., *Physical Chemistry of Surfaces*, Wiley, New York, (1990).
- Anderson, T. L., “Fracture Mechanics: Fundamentals and Applications”, CRC Press, Boca Raton, FL, (1995).
- ASTM C 109, American Society for Testing and Materials; Compressive Strength of Hydraulic Cement Mortars (Using 2-in or 50-mm Cube Specimens); ASTM C 109-12; 4.01, (2012).
- ASTM C 150, American Society for Testing and Materials; Standard specification of portland cement; ASTM C 150-12; 4.01, (2012).
- Autumn, K., Liang, Y. A., Hsieh, S. T., Zesch, W., Chan, W. P., Kenny, T. W., Fearing, R. and Full, R. J., “Adhesive force of a single gecko foot-hair,” *Nature* 405, 681–685, (2000).
- Aveyard, R., Binks, B. P., Clint, J. H., Emulsions stabilised solely by colloidal particles, *Advances in Colloid and Interface Science*, Vol. 100-102, 28 February, pp. 503-546, (2003).
- Bahadur, V., Mishchenko, L., Hatton, B., Taylor, J. A., Aizenberg, J., and Krupenkin, T., *Langmuir*, 27 (23), pp 14143–14150, (2011).
- Baier, R. E., Sharfin, E. G., Zisman, W. A., "Adhesion: Mechanisms that Assist or Impede It." *Science*, 162, 1360 (1968).
- Bak, P., Tang, C., Wiesenfeld, K., “Self-organized criticality: An explanation of the $1/f$ noise”, *Phys Rev Lett*, 59:381–384, (1987).
- Ball, P., “Engineering Shark Skin and Other Solutions” *Nature*, 400, 507-509, (1999).
- Bar-Cohen, Y., *Biomimetics: biologically inspired technologies*, Boca Raton, FL: Taylor and Francis, (2006).
- Barnes, P., Bensted, J., *Structure and Performance of Cements*, Taylor & Francis, Edition 2, Nov 1, (2002).
- Barthlott, W. and Neinhuis, C., “Purity of the Sacred Lotus, or Escape from Contamination in Biological Surfaces,” *Planta* 202 1-8, (1997).

- Bechert, D. W., Bruse, M., and Hage, W., "Experiments with three-dimensional riblets as an idealized model of shark skin," *Exp. Fluids* 28 403-412, (2000).
- Bhushan, B., *Tribology and Mechanics of Magnetic Storage Systems*, second ed., Springer-Verlag, New York, (1996).
- Bhushan, B., *Tribology Issues and Opportunities in MEMS*, Kluwer Academic Pub., Dordrecht, Netherlands, (1998).
- Bhushan, B., *Principles and Applications of Tribology*, Wiley, New York, (1999).
- Bhushan, B., *Introduction to Tribology*, Wiley, New York, (2002).
- Bhushan, B., "Adhesion and Stiction: Mechanisms, Measurement Techniques and Methods for Reduction," *J. Vac. Sci. Technol. B* 21, 2262-2296, (2003).
- Bhushan, B., *Nanotribology and Nanomechanics – An Introduction* (Springer-Verlag, Heidelberg), (2005a).
- Bhushan B., "Nanotribology and Nanomechanics," *Wear*, 259, 1507-1531, (2005b).
- Bhushan, B., "Adhesion of multi-level hierarchical attachment systems in gecko feet," *J. Adhes. Sci. Technol.* 21, 1213–1258, (2007a).
- Bhushan, B., *Springer Handbook of Nanotechnology*, second ed., Springer, Heidelberg, Germany, (2007b).
- Bhushan, B., Nanotribology and nanomechanics of MEMS/NEMS and BioMEMS/BioNEMS materials and devices *Microelectron. Eng.*, 84, 387, (2007c).
- Bhushan, B., *Nanotribology and Nanomechanics – An Introduction*, 2nd ed., Springer-Verlag, Heidelberg, Germany, (2008).
- Bhushan, B., "Biomimetics: Lessons from Nature – An Overview," *Phil. Trans. R. Soc. A* 367, 1445-1486, (2009).
- Bhushan, B., Israelachvili, J. N., and Landman, U., "Nanotribology: Friction, Wear and Lubrication at the Atomic Scale," *Nature* 374, 607-616, (1995).
- Bhushan, B. and Jung, Y. C., "Micro and Nanoscale Characterization of Hydrophobic and Hydrophilic Leaf Surface," *Nanotechnology* 17, 2758-2772, (2006).
- Bhushan, B., Nosonovsky M., and Jung, Y. C., "Towards Optimization of Patterned Superhydrophobic Surfaces" *J. Royal Soc. Interface* 4, 643-648, (2007).

- Bhushan, B., Jung, Y. C., and Koch, K., "Micro-, Nano- and Hierarchical Structures for Superhydrophobicity, Self-Cleaning and Low Adhesion," *Phil. Trans. R. Soc. A* 367, 1631-1672, (2009b).
- Bhushan, B., and Nosonovsky, M., *Phil. Trans. R. Soc. A*, 368, 4713-4728, (2010a).
- Bhushan, B. and Nosonovsky, M., "The rose petal effect and the modes of superhydrophobicity" *Phil. Trans Royal. Soc. A.*, Vol. 368:4713-4728, (2010b).
- Bikerman, "Sliding of drops from surfaces of different roughnesses", *J. J. J. Colloid Sci.*, 5, 349, (1950).
- Bico, J., Thiele, U., and Quéré, D., "Wetting of Textured Surfaces," *Colloids and Surfaces A*, 206, 41-46, (2002).
- Binks B. P. and Lumsdon S. O., Influence of Particle Wettability on the Type and Stability of Surfactant-Free Emulsions, *Langmuir* 16 (23), pp 8622-8631, (2000).
- Boinovich, L., Emelyanenko, A., *Adv Colloid Interface Sci*, 165, 60-69, (2011).
- Boinovich, L. B. & Emelyanenko, A. M. Anti-icing potential of superhydrophobic coatings. *Mendelev Commun.* 23, 3–10, (2013).
- Bonn, D., Eggers, J., Indekeu, J., Meunier, J., and Rolley, E., "Wetting and Spreading," *Reviews of Modern Physics*, 81, 739-805, (2009).
- Bormashenko, E., *Am. J. Phys.* 78, 1309-1311, (2010).
- Bormashenko, E., *J. Adhesion Sci Technol.*, in press, (2012).
- Bormashenko, E. et al., "Wetting properties of the multiscaled nanostructured polymer and metallic superhydrophobic surfaces," *Langmuir*, 22, 9982–9985, (2006a).
- Bormashenko, E. et al. "Micrometrically scaled textured metallic hydrophobic interfaces validate the Cassie–Baxter wetting hypothesis," *J. Colloid Interface Sci.*, 302, 308–311, (2006b).
- Bormashenko, E., Bormashenko, Y., Stein, T., Whyman, G., and Pogreb, R., *Langmuir*, 23, 4378–4382, (2007a).
- Bormashenko, E., Bormashenko, Y., Whyman, G., Pogreb, R., Musin, A., Jager, R., and Barkay, Z., *Langmuir*, 24 (8), 4020-4025, (2008).
- Bormashenko, E., Stein, T., Pogreb, R., and Aurbach, D., *J. Phys. Chem. C* , 113, 5568–5572, (2009).

- Bormashenko, E., Pogreb, R., Whyman, G., Bormashenko, Y., Erlich, M., *Appl. phys. Lett.* 90, 201917, (2007b).
- Bormashenko, E., *Am. J. Phys.* 78, 1309-1311, (2010).
- Boruvka, L.; Neumann, A. W. J. *Chem. Phys.*, 66, 5464-5476, (1977).
- Burton, Z., and Bhushan, B., "Hydrophobicity, Adhesion, and Friction Properties of Nanopatterned Polymers and Scale Dependence for Micro- and Nanoelectromechanical Systems," *Nano Lett.* 5, 1607-1613, (2005).
- Burton, Z. and Bhushan, B., "Surface Characterization and Adhesion and Friction Properties of Hydrophobic Leaf Surfaces," *Ultramicroscopy* 106, 709-719, (2006).
- Cammarata, R.C., *Prog. Surf. Sci.*, 46, 1-38, (1994).
- Cao, L.-L.; Jones, A. K.; Sikka, V. K.; Wu, J.; Gao, D. Anti-Icing Superhydrophobic Coatings. *Langmuir*, 25, 12444-12448, (2009).
- Carré, A., and Mittal, K. L., Superhydrophobic surfaces, VSP/Brill, Leiden, (2009).
- Cassie, A. and Baxter, S., "Wettability of Porous Surfaces," *Trans. Faraday Soc.* 40, 546-551, (1944).
- Chang, F. M., Hong, S. J., Sheng, Y. J., and Tsao, H. K., *Appl. Phys. Lett.*, 95, 064102, (2009).
- Charles Ross & Son Company, Improve emulsion stability through ultra-high shear mixing, Mixing Technology Insight #17, http://www.mixers.com/insights/mti_17.pdf.
- Chawla, K.K., Composites Materials: Science and Engineering, 2nd ed., Springer-Verlag, New York, NY, pp. 164-211, (1998).
- Choi, C-H., and Kim, C-J., *Phys. Rev. Lett.*, 96, 066001, (2006).
- Clauser, H. R., *Scientific American*, 229, 36, (1973).
- Cornie, J. A., Chiang, Y-M., Uhlmann, D. R., Mortensen, A. S., Collins, J. M., *Ceram. Bull.*, 65, 293, (1986).
- De Gennes, P. G., Brochard-Wyart, F., and Quéré, D., "Capillarity and wetting phenomena: drops, bubbles, pearls, waves", *Springer*, (2004).
- Derjaguin, B. V., *Acta Physicochim URSS*, 12, 171, (1940).

- Derjaguin, B. V., Churaev, N. V., Muller, V. M., Surface forces. New York and London: Consultants Bureau, (1987).
- Deutsch, G. S., 23rd National SAMPLE Symposium, 34, May (1978).
- Dhir R., Hewlett P., Concrete in the Service of Mankind: Radical concrete technology, Taylor & Francis, Volume 4, 758 pages, (2003).
- Dietrich, S., M. N. Popescu, and M. Rauscher, “Wetting on structured substrates,” J. Phys.: Condens. Matter 17, S577, (2005).
- Dotan, A., Dodiuk, H.; Laforte, C.; and Kenig, S. “The Relationship between Water Wetting and Ice Adhesion”, *J. Adhes. Sci. Technol.*, 23, 1907-1915,(2009).
- Du Pont, “What is Kevlar?”, Retrieved, (2012).
- Dussan, E. B. & Chow, R. T.-P. On the ability of drops or bubbles to stick to nonhorizontal surfaces of solids. *J Fluid Mechanics* 137, 1–29, (1983).
- Eadie, L., Ghosh, T.K., Biomimicry in textiles: Past, present and potential. An overview. *Journal of the Royal Society Interface* 8: 761–775, (2011).
- Erbil, H. Y., Demirel, A. L., and Avci, Y., “Transformation of a Simple Plastic into a Superhydrophobic Surface,” *Science* 299, 1377-1380, (2003).
- Extrand, C. W., *J. Colloid Interface Sci*, 207, 11–19, (1998).
- Extrand, C.W., “Model for Contact Angles and Hysteresis on Rough and Ultraphobic Surfaces,” *Langmuir*, 18, 7991-7999, (2002).
- Farhadi, S.; Farzaneh, M.; Kulinich, S. A., “Anti-icing Performance of Superhydrophobic Surfaces”, *Appl. Surf. Sci.*, 257, 6264-6269, (2011).
- Feng, L., Zhang, Y., Xi, J., Zhu, Y., Wang, N., Xia, F., and Jiang, L., *Langmuir*, 24, 4114–4119, (2008).
- Ferrick, M. G., Mulherin, N. D., Haehnel, R. B., Coutermarsh, B. A., Durell, G. D., Tantillo, T. J., Curtis, L. A., St. Clair, T. L., Weiser, E. S., Cano, R. J., Smith, T. M., Martinez, E. C., “Evaluation of ice release coatings at cryogenic temperature for the space shuttle”, *Cold Regions Science and Technology*, Volume 52, Issue 2, Pages 224-243, April (2008).
- Flores-Vivian, I., Hejazi, V., Sobolev, K., Nosonovsky, M., “Self-assembling particle-siloxane coatings for transferring concrete towards superhydrophobicity”, *Applied Material and Interfaces*, (2013).

- Fowkes, F. M.; Harkins, W. D., " The state of the monolayers adsorbed at the interface solid–liquid solution", *J. Am. Chem. Soc.*, 62, 2(12), 3377-3377, (1940).
- Furukawa, Y. & Wettlaufer, J. S. Snow and ice crystals. *Phys. Today* 12, 70–71, (2007).
- Gao, H., Wang, X., Yao, H., Gorb, S. and Arzt, E., "Mechanics of hierarchical adhesion structures of geckos," *Mech. Mater.* 37, 275–285, (2005).
- Gao, L., and McCarthy, T. J., *Langmuir*, 24, 9184–9188, (2008).
- Gao, X. F. and Jiang, L., "Biophysics: Water-repellent Legs of Water Striders," *Nature* 432, 36, (2004).
- Gao, X., Yan, X., Yao, X., Xu, L., Zhang, K., Zhang, J., Yang, B., and Jiang, L., "The dry-style antifogging properties of mosquito compound eyes and artificial analogues prepared by soft lithography," *Adv. Mater.* 19, 2213–2217, (2007).
- Genzer, J. and Efimenko, K., "Recent developments in superhydrophobic surfaces and their relevance to marine fouling: a review," *Biofouling* 22, 339-360, (2006).
- Good, R. J., *J. Am. Chem. Soc.*, 79, 5041, (1952).
- Gorb, S., "Fundamental surfaces in biology: mechanisms and applications" in *Biomimetics: Biologically Inspired Technologies* (ed. by Y.Bar-Cohen, Taylor and Francis, Boca Raton), pp. 381-397, (2005).
- Guo, P., Zheng, Y., Wen, M., Song, C., Lin, Y., Jiang, L., *Adv. Mater.*, 24, 2642–2648, (2012).
- He, B., Patankar, N.A., and Lee, J., "Multiple Equilibrium Droplet Shapes and Design Criterion for Rough Hydrophobic Surfaces," *Langmuir*, 19, 4999-5003, (2003).
- Hejazi, V., and Nosonovsky, M., *Langmuir*, 28 (4), pp 2173–2180, (2012).
- Hejazi V., Sobolev K., Nosonovsky M., "From superhydrophobicity to icephobicity: forces and interaction analysis" *Nature's Sci. Rep.* 3:2194, (2013).
- Herminghaus, S., 2000, "Roughness-Induced Non-Wetting," *Europhys. Lett.*, 52, 165-170, (2000).
- Israelachvili, J. N., *Intermolecular and Surface Forces*, 2nd edition, Academic Press, London, (1992).

- Israelachvili, J. N., *Intermolecular and Surface Forces*, 3rd Ed., Academic Press, London (2011).
- Itoh, M., Tamano, S., Iguchi, R., Yokota, K., Akino, N., Hino, R., and Kubo, S. "Turbulent Drag Reduction by the Seal Fur Surface," *Phys Fluids*, 18, 065102, (2006).
- Jin, M., Feng, X., Feng, L., Sun, T., Zhai, J., Li, T., Jiang, L., *Adv. Mater.*, 17, 1977–1981 (2005).
- Johnson, R. E. and Dettre, R. H., "Contact Angle Hysteresis," *Contact Angle, Wettability, and Adhesion, Adv. Chem. Ser.*, Vol. 43 (Ed. By F. M. Fowkes American Chemical Society, Washington, D. C.), pp. 112-135, (1964).
- Jung, Y. C. and Bhushan, B., "Contact Angle, Adhesion, and Friction Properties of Micro- and Nanopatterned Polymers for Superhydrophobicity," *Nanotechnology* 17, 4970-4980, (2006).
- Jung, Y. C. and Bhushan, B., "Wetting transition of water droplets on superhydrophobic patterned surfaces," *Scripta Mater.* 57, 1057-1060, (2007).
- Jung, Y. C. and Bhushan, B., "Dynamic Effects Induced Transition of Droplets on Biomimetic Superhydrophobic Surfaces," *Langmuir* 25, 9208-9218, (2009a).
- Jung, Y. C. and Bhushan, B., "Wetting Behavior of Water and Oil Droplets in Three Phase Interfaces for Hydrophobicity/philicity and Oleophobicity/philicity," *Langmuir*, 25 (24), pp 14165–14173, (2009b).
- Jung, Y. C. and Bhushan, B., "Biomimetic Structures for Fluid Drag Reduction in Laminar and Turbulent Flows," *J. Phys.: Condens. Matter* 22, 03510, (2010a).
- Jung, S., Dorrestijn, M., Raps, D., Das, A., Megaridis, C. M., and Poulikakos, D., *Langmuir*, 27 (6), pp 3059–3066, (2011).
- Jung, S., Tiwari, M. K., Doan, N. V., Poulikakos, D., "Mechanism of supercooled droplet freezing on surfaces", *Nature Comm*, 3:615, (2012).
- Kauzmann, W., "Some factors in the interpretation of protein denaturation". *Advances in Protein Chemistry* 14: 1–63, (1959).
- Kestursayta, M., Kim, J. K., Rohatgi, P. K. *Metall. Mater. Trans.*, 32A, 2115–2125, (2001).
- Kietzig, A.M., Hatzikiriakos, S.G., Englezos, P., "Patterned Superhydrophobic Metallic Surfaces" *Langmuir*, 25, 4821-4827, (2009).

- Kijlstra, J., Reihs, K., and Klami, A., "Roughness and Topology of Ultra-Hydrophobic surfaces," *Colloids and Surfaces A: Physicochem. Eng. Aspects* 206, 521-529, (2002).
- Kim, P., Wong, T.-S., Alvarenga, J., Kreder, M. J., Adorno-Martinez, W. E., Aizenberg, J., *ACS Nano.*, DOI: 10.1021/nn302310q, (2012).
- Kim, J. H., Robertson, R. E. "Structure and properties of poly(vinyl alcohol)-modified mortar and concrete", *Cement and Concrete Research*, 29(3), 407-415, (1999)
- Koch, K., Dommisse, A., and Barthlott, W., "Chemistry and crystal growth of plant wax tubules of Lotus (*Nelumbo nucifera*) and Nasturtium (*Tropaeolum majus*) leaves on technical substrates," *Crystl. Growth Des.* 6, 2571-2578, (2006a).
- Koch, K., Bhushan, B., and Barthlott, W., "Diversity of Structure, Morphology, and Wetting of Plant Surfaces (invited)," *Soft Matter* 4, 1943-1963, (2008a).
- Koch, K., Bhushan, B., and Barthlott, W., "Multifunctional Surface Structures of Plants: An Inspiration for Biomimetics (invited)," *Prog. Mater. Sci.* 54, 137-178, (2009a).
- Koch, K., Bhushan, B., Jung, Y. C., and Barthlott, W., "Fabrication of artificial Lotus leaves and significance of hierarchical structure for superhydrophobicity and low adhesion," *Soft Matter* 5, 1386-1393, (2009b).
- Koch, K., Bhushan, B., Eniskat, H. -J., and Barthlott, W., "Self-Healing of Voids in the Wax Coating on Plant Surfaces," *Phil. Trans. R. Soc. A* 367, 1673-1688, (2009c).
- Krasovitski, B., and Marmur, A., *Langmuir*, 21, 3881-3885, (2005).
- Kreider K. G., Prewo, K. M.,: *Composite Materials*, vol. 4, Academic Press, New York, 400, (1974).
- Kulinich, S. A., Farhadi, S., Nose, K., and Du, X. W., *Langmuir*, 27 (1), pp 25-29, (2011).
- Kulinich, S. A., and Farzaneh, M., *Appl. Surf. Sci.*, 230:232-240, (2004).
- Kulinich, S. A.; Farzaneh, M. How Wetting Hysteresis Influences Ice Adhesion Strength on Superhydrophobic Surfaces. *Langmuir*, 25, 8854-8856, (2009).
- Kwon, H- M., Paxson, A. T., Varanasi, K. K., and Patankar, N. A., *Phys. Rev. Lett.*, 106, 036102, (2011).
- Laboratory Ice Adhesion test Results for Commercial Icephobic Coatings for Pratt & Whitney, CRREL, May (2004).

- Lafuma, A., and Quèrè, D., "Superhydrophobic states", *Nature Mater.*, 2, 457-460, (2003).
- Li, W., and Amirfazli, A., *Adv. Mater.*, 19, 3421-3422, (2007).
- Ling, W. Y. L.; Ng, T. W.; Neild, A. *Langmuir*, 26, 17695-17702, 2010.
- Ling, W. Y. L.; Ng, T. W.; Neild, A.; Zheng, Q. *Journal of Colloid and Interface Science*, 354, 832-842, (2011).
- Liu, M., Wang, S., Wei, Z., Song, Y., Jiang, L., *Adv. Mater.*, 21, 665-669, (2009).
- Liu, Y.Y., Chen, X.Q., and Xin, J.H., *Bioinspir. Biomim.*, 3, 046007, (2008).
- Manukyan, G., Oh, J. M., van den Ende, D., Lammertink, R., Wesseling, M., and Mugele, F., *Phys. Rev. Lett.*, 106, 014501, (2011).
- Marmur, A., "Wetting on Hydrophobic Rough Surfaces: to be Heterogeneous or Not to be?" *Langmuir*, 19, 8343-8348, (2003).
- Marmur A., "The Lotus Effect: Superhydrophobicity and Metastability," *Langmuir*, 20, 3517-3519, (2004).
- McHale, G., *Langmuir*, 25, 7185-7187, (2009).
- Menini, R., Farzaneh, M., *Surf. Coat. Technol.*, 203, 1941-1946, (2009).
- Menini, R., Ghalimi, Z., Farzaneh, M., *Cold Reg. Sci. Technol.*, 65, 65-69, (2011).
- Meuler, A. J., McKinley G. H., Cohen R. E., *ACS Nano.*, 4, 7048-7052, (2010a).
- Meuler, A. J., Smith, J. D., Varanasi, K. K., Mabry, J. M., McKinley, G. H., Cohen, R. E., *ACS Appl. Mater. Interfaces.*, 11, 3100-3110, (2010b).
- Miwa, M., Fujishima, A., Hashimoto, K. & Watanabe, T. Effects of the surface roughness on sliding angles of water droplets on superhydrophobic surfaces, *Langmuir* 16, 5754-5760 (2000).
- Morcos, " Surface Tension of Stress-Annealed Pyrolytic Graphite", *I. J. Chem. Phys.*, 57 (4), 1801-180, (1972).
- Moret, M.A., and Zebende, G. F., "Amino acid hydrophobicity and accessible surface area", *Phys Rev E*, 75:011920, (2007).
- Mortazavi, V., Nosonovsky, M., "Wear-induced microtopography evolution and wetting properties of self-cleaning, lubricating and healing surfaces", *Journal of Adhesion Science and Technology*, Vol. 25, 12, 1337-1359, (2011a).

- Mortazavi V., Nosonovsky, M., "Friction-Induced Pattern-Formation and Turing systems" *Langmuir*, 27 (8), 4772-4779, (2011b).
- Mueller, T., "Biomimetics design by nature," *National Geographic*, 68-90, April (2008).
- Muzenski S.W., Flores-Vivan I., Beyene M.A., Sobolev K., "Air Void Structure and Mechanical Performance of Fiber Reinforced Composites with Nano-Particle Based Polymethyl Hydrosiloxane Emulsions", August 1, (2013) (Submitted).
- Neinhuis, C., and Barthlott, W., "Characterization and Distribution of Water-Repellent, Self-Cleaning Plant Surfaces," *Annals of Botany* 79, 667-677, (1997).
- Ngai, T., Auweter, H., and Behrens, S.H., "Environmental responsiveness of microgel particles and particle-stabilized emulsions." *Macromolecules* 39.23 pp. 8171-8177, (2006).
- Nicolis, G., Prigogine, I., *John Wiley & Sons: New York* (1977).
- Nosonovsky, M., *J. Chem. Phys.*, 126, 224701, (2007a).
- Nosonovsky, M., Multiscale roughness and stability of superhydrophobic biomimetic interfaces *Langmuir* 23 (6), 3157-3161, (2007b).
- Nosonovsky, M., "Slippery when wetted" *Nature*, 477, 412-413 (2011).
- Nosonovsky, M. and Bhushan, B., "Roughness optimization for biomimetic superhydrophobic surfaces," *Microsyst. Technol.* 11, 535-549, (2005).
- Nosonovsky, M. and Bhushan, B., "Stochastic model for metastable wetting of roughness-induced superhydrophobic surfaces," *Microsyst. Technol.* 12, 231-237, (2006a).
- Nosonovsky, M. and Bhushan, B., "Wetting of Rough Three-Dimensional Superhydrophobic Surfaces," *Microsyst. Technol.* 12, 273-281, (2006b).
- Nosonovsky, M.; Bhushan, B. *Nano Lett.*, 7, 2633-2637, (2007c).
- Nosonovsky, M. and Bhushan, B., "Hierarchical Roughness Makes Superhydrophobic Surfaces Stable," *Microelectronic Eng.* 84, 382-386, (2007b).
- Nosonovsky, M. and Bhushan, B., Multiscale Dissipative Mechanisms and Hierarchical Surfaces: Friction, Superhydrophobicity, and Biomimetics, Springer-Verlag, Heidelberg, Germany, (2008a).
- Nosonovsky, M., and Bhushan, B., *Adv. Funct. Mater.* 18, 843 (2008b).

- Nosonovsky, M., and Bhushan, B., *J. Phys. Condens. Matter* 20, 395005 (2008c).
- Nosonovsky, M. and Bhushan, B., “Patterned Non-Adhesive Surfaces: Superhydrophobicity and Wetting Regime Transitions,” *Langmuir* 24 1525-1533, (2008d).
- Nosonovsky, M.; Bhushan, B. Phase Behavior of Capillary Bridges: Towards Nanoscale Water Phase Diagram. *Phys. Chem. Chem. Phys.*, 10, 2137–2144, (2008e).
- Nosonovsky, M., and Bhushan, B., “Do Hierarchical Mechanisms of Superhydrophobicity Lead to Self-organized Criticality?” *Scripta Mater.* 59 (opinion) 941-944, (2008f).
- Nosonovsky, M. and Bhushan, B., “Superhydrophobicity for Energy Conversion and Conservation Applications,” *J. Adhesion Sci. Tech.* 22 2105-2115, (2008h).
- Nosonovsky, M. and Bhushan, B., *Phil. Trans. Royal. Soc. A*367, 1511-1539, (2009a).
- Nosonovsky, M. and Bhushan, B., “Superhydrophobic Surfaces and Emerging Applications: Non-Adhesion, Energy, Green Engineering,” *Curr. Opin. Colloid Interface Sci.* 14 270-280, (2009b).
- Nosonovsky, M., Hejazi, V., *ACS Nano.*, 6 (10), pp 8488–8491, (2012).
- Nosonovsky, M.; Hejazi, V.; Nyong, A. E.; Rohatgi, P. K. *Langmuir*, 27 (23), pp 14419–14424, (2011).
- Nosonovsky, M., and Rohatgi, P. K., “Biomimetics in Materials Science: Self-healing, self-lubricating, and self-cleaning materials”, (Springer Series in Materials Science, ISBN 978-1-4614-0925-0), (2012).
- Patankar, N.A., “On the Modeling of Hydrophobic Contact Angles on Rough Surfaces” *Langmuir*, 19, 1249-1253, (2003).
- Patankar, N.A., “Transition Between Superhydrophobic States on Rough Surfaces” *Langmuir*, 20, 7097-7102, (2004a).
- Patankar, N.A., “Mimicking the Lotus Effect: Influence of Double Roughness Structures and Slender Pillars,” *Langmuir*, 20, 8209-8213, (2004b).
- Petrovic, J. J. Review: Mechanical Properties of Ice and Snow. *J. Mater. Sci.*, 38, 1–6, (2003).
- Phillips, J. C., “Scaling and self-organized criticality in proteins”, *PNAS* vol. 106 :3107-3112, (2009).

- Pockels, A., *Physik. Z.*, 15, 39-46, (1914).
- Poetes, R., Holtzmann, K., Franze, K., Steiner, U., *Phys. Rev. Lett.* 105, 166104, (2010).
- Polidori, G., Taïar, R., Fohanno, S., Mai, T., and Lodini, A. "Skin-friction Drag Analysis from the Forced Convection Modeling in Simplified Underwater Swimming," *J. Biomech.*, 39 2535-2541, (2006).
- Poole B., *Biomimetics: Borrowing from Biology*, The Naked Scientists, <http://www.thenakedscientists.com/HTML/articles/article/biomimeticsborrowingfrombiology/>, (2007).
- Porro, A., Dolado JS, Campillo I, Erkizia E, Miguel Y, Effects of nanosilica additions on cement pastes, in: R.K. Dhir, M.D. Newlands, L.J. Csetenyi (Eds.), *Application of Nanotechnology in Concrete Design*, (2005).
- Qian, B., and Shen, Z., "Fabrication of Superhydrophobic Surfaces by Dislocation-Selective Chemical Etching on Aluminum, Copper, and Zinc Substrates", *Langmuir*, 21, 9007-9009, (2005).
- Raraty, L. E., and Tabor, D., *Proc. R. Soc. A.*, 245, 184–201, (1958).
- Rayleigh, L., *Nature*, 43, 437-439, (1891).
- Rechenberg, I and El Khyeri, A.R., "The Sandfish of the Sahara. A Model for Friction and Wear Reduction." Department of Bionics and Evolution Techniques, Technical University of Berlin website <http://www.bionik.tu-berlin.de/institut/safiengl.htm>, accessed on August 14, (2007).
- Rohatgi P.K, *Metal-matrix Composites*, Defence Science Journal, Vol 43, No 4, pp 323-349, (1993).
- Rohatgi, P. K.; Liu, Y.; Barr, T. L. *Metallurgical and Materials Transactions*, 22, 1435-1441, (1991).
- Rowlinson, J. S., Widom, B., *Molecular Theory of Capillarity* (Clarendon, Oxford), (1982).
- Schier, J. F., Juergens, R. J., *Astronautics and Aeronautics*, 44, (1983).
- Semal, S., Blake, T. D., Geskin, V., de Ruijter, M. L., Castelein, G., and De Coninck, J., "Influence of Surface Roughness on Wetting Dynamics," *Langmuir* 15, 8765- 8770, (1999).
- Shepard, J. W., and Bartell, F. E. J., *J. Phys. Chem.*, 57, 458, (1953).

- Shibuichi, S., Onda, T, Satoh, N., and Tsujii, K., “Super-Water-Repellent Surfaces Resulting from Fractal Structure,” *J. Phys. Chem.*, 100, 19512-19517, (1996).
- Shirtcliffe, N. J., and McHale, G., Newton, M. I., and Perry, C. C., “Wetting and Wetting Transitions on Copper-Based Super-Hydrophobic Surfaces”, *Langmuir*, 21, 937-943, (2005).
- Shuttleworth, R. and Bailey, G.L.J., “The Spreading of Liquid over a Rigid Solid,” *Discussions of the Faraday Society*, 3, 16-22, (1948).
- Sivas, S. L., Riegler, B., Thomaier, B., Hoover, K., “A Silicone-Based Ice-Phobic Coating for Aircraft ”, NuSil Technology LLC, 37th ISTC, (2007).
- Smith, P. R., Froes, F. H., *J. Met.* Vol. 36, no. 3, pp. 19-26. Mar. (1984).
- Sobolev K. and Ferrada-Gutiérrez M., How Nanotechnology Can Change the Concrete World: Part 1. *American Ceramic Society Bulletin*, No. 10, pp. 14-17, (2005).
- Sobolev K. and Ferrada-Gutiérrez M., How Nanotechnology Can Change the Concrete World: Part 2. *American Ceramic Society Bulletin*, 11, pp. 16-19, (2005).
- Sobolev K. and Batrakov V., The Effect of a PEHSO on the Durability of Concrete with Supplementary Cementitious Materials. *ASCE Journal of Materials in Civil Engineering*, 19(10), pp. 809-819, (2007).
- Sobolev K., Flores I., Hermosillo R. and Torres-Martínez L.M.; Application of nanomaterials in high-performance cement composites; *Proceedings of the ACI Session on Nanotechnology of Concrete: Recent Developments and Future Perspectives – 2006*; edited by K. Sobolev and S.P. Shah, Denver, USA, ACI SP-254, , pp. 93-120, (2008).
- Sobolev K., Tabatabai H., Zhao J., Flores I., Muzenski S., Oliva M.G., Rauf R., Rivero R., Superhydrophobic Engineered Cementitious Composites for Highway Applications: Phase I, *CFIRE 04-09*, May (2013).
- Sobolev K., Tabatabai H., Zhao J., Flores I., Muzenski S., Oliva M.G., Rauf R., Superhydrophobic Engineered Cementitious Composites for Highway Applications: Phase II, *CFIRE 05-10*, June (2013).
- Sommers, A. D., and Jacobi, A. M., “Creating micro-scale surface topology to achieve anisotropic wettability on an aluminum surface”, *J. Micromech. Microeng.*, 16, 1571–1578, (2006).

- Spenko, M. J., Haynes, G.C., Saunders, J.A., Cutkosky, M.R., Rizzi, A.A., Full, R.J., Koditschek, D.E., Biologically inspired climbing with a hexapedal robot. *J Field Robot* 25:223–42, (2008).
- Stefanidou, M., Matziaris K. and Karagiannis G., Hydrophobization by Means of Nanotechnology on Greek Sandstones Used as Building Facades, *Geosciences*, 3, 30-45; doi:10.3390/geosciences3010030, (2013).
- Sun, M, Luo, C., Xu, L., Ji, H., Ouyang, Q., Yu, D., and Chen, Y., “Artificial Lotus Leaf by Nanocasting,” *Langmuir*, 21, 8978-8981, (2005).
- Tadmor, R.; Chaurasia, K.; Yadav, P. S.; Leh, A.; Bahadur, P.; Dang, L.; Hoffer, W. R. *Langmuir*, 24, 9370-9374, (2008).
- Tadmor, R. et al., “Measurement of Lateral Adhesion Forces at the Interface between a Liquid Drop and a Substrate” *Phys. Rev. Lett.*, 103, 266101, (2009).
- Taha, Z., H. K. Ielana, H Aoyama, R Ariffin, J Gonzales, N. Sakundani, and S. Bhakti, "Effect of insert geometry on surface roughness in the tuning process of AISI D2", The 11th Asia pacific industrial Engineering and management systems Conference. 7-10 December, (2010).
- Tsai, P., Pacheco, S., Pirat, C., Lefferts, L., and Lohse, D., *Langmuir* 25, 12293 (2009).
- Tuteja, A., Choi, W., Ma, M., Mabry, J. M, Mazzella, S. A., Rutledge, G. C., McKinley, G. H., and Cohen, R. E., “Designing Superoleophobic Surfaces,” *Science* 318, 1618-1622, (2007).
- Vedantam, S.; Panchagnula, M. V. *Phys Rev Lett.*, 99, 176102, (2007).
- Verho, T., Bower, C., Andrew, P., Franssila, S., Ikkala, O., and Ras, R. H. A., *Adv. Mater.*, 23, 673–678, (2011).
- Wagner, P., Furstner, R, Barthlott, W. and Neinhuis, C., “Quantitative Assessment to the Structural Basis of Water Repellency in Natural and Technical Surfaces,” *J. Exper. Botany* 54, 1295-1303, (2003).
- Wainwright, S. A . , Biggs, W. D., Currey, J. D., and Gosline, J. M., *Mechanical Design in Organisms*. Princeton University Press , Princeton, NJ, (1976).
- Wainwright, S.A., Vosburgh, F., and Hebrank, J.H., “Shark Skin: Function in Locomotion” *Science*, 202 747-749, (1978).
- Walter, J. L., *In Situ Composites IV*, Elsevier, NewYork, 85, (1982).
- Wang, S., and Jiang, L., *Adv. Mater.*, 19, 3423–3424, (2007).

- Wang, S., Lin Fen, Huan Liu, Taolei Sun, Xi Zhang, Lei Jiang, Daoben Zhu, "Manipulation of Surface Wettability between Superhydrophobicity and Superhydrophilicity on Copper Films", *ChemPhysChem*, 6, 1475 –1478, (2005).
- Wenzel, R. N., "Resistance of Solid Surfaces to Wetting by Water," *Indust. Eng. Chem.* 28 988-994, (1936).
- Wong, T. -S., Kang, S. H., Tang, S. K. Y., Smythe, E. J., Hatton, B. D., Grinthal, A., and Aizenburg, J., *Nature*, 477, 443–447, (2011).
- Wu, D. Y., Meure, S., Solomon, D., *Prog. Polym. Sci.*, 33, 479, (2008).
- Xia, F., and Jiang, L., *Adv. Mater.*, 20, 2842–2858, (2008).
- Yang, S. H.; Nosonovsky, M.; Zhang, H.; Chung, K.-H. Nanoscale Water Capillary Bridges under Deeply Negative Pressure. *Chem. Phys. Lett.* (2008), 451, 88–92.
- Yost, F.G, Michael, J.R., and Eisenmann, E.T., "Extensive Wetting Due to Roughness," *Acta Metall. Mater.*, 45, 299-305, (1995).
- Zheng, L., Li, Z., Bourdo, S., Khedir R. K., Asar, M. P., Ryerson, C. C., and Biris, A.S., *Langmuir*, 27 (16), pp 9936–9943, (2011).

CURRICULUM VITAE

EDUCATION

- ❖ BSc in Mechanical Engineering (2004), Iran University of Science and Technology, Tehran, Iran.
Thesis Title: Analysis and investigation on cooling water piping system of Tehran petroleum refinery.
- ❖ MSc in Mechanical Engineering (2007), University of Tehran, Tehran, Iran.
Thesis Title: Experimental investigation on heat transfer and pressure drop during the condensation inside tubes with twisted tape inserts.
- ❖ PhD in Mechanical Engineering (2014), University of Wisconsin-Milwaukee, (GPA: 4.0 out of 4.0).
Thesis Title: Wetting, superhydrophobicity and icephobicity in biomimetic composite materials.

HONORS AND AWARDS

- ❖ CEAS Deans Scholarship Award, University of Wisconsin-Milwaukee, January 2014.
- ❖ CEAS Academic Excellence Award, University of Wisconsin-Milwaukee, December 2013.
- ❖ Distinguished Dissertation Fellowship award, University of Wisconsin-Milwaukee, 2013-2014.
- ❖ Distinguished Graduate Student Fellowship award, University of Wisconsin-Milwaukee, 2012-2013.
- ❖ Chancellor's graduate student award, University of Wisconsin-Milwaukee, 2013-2014.
- ❖ Chancellor's graduate student award, University of Wisconsin-Milwaukee, 2012-2013.
- ❖ Chancellor's graduate student award, University of Wisconsin-Milwaukee, 2011-2012.
- ❖ Chancellor's graduate student award, University of Wisconsin-Milwaukee, 2010-2011.
- ❖ Nominated for Iranian Society of Mechanical Engineers' best BSc thesis award.

PUBLICATION

JOURNAL PAPERS

- ❖ Ismael V. Flores, Vahid Hejazi, Konstantin Sobolev, Michael Nosonovsky, "Self-assembling particle-siloxane coatings for superhydrophobic concrete", 2013, *Applied Materials and Interfaces* (Submitted).
- ❖ Vahid Hejazi, Konstantin Sobolev, Michael Nosonovsky, " From superhydrophobicity to icephobicity; forces and interaction analysis", *Scientific reports*, 2013, DOI:10.1038/srep02194.
- ❖ Vahid Hejazi, Michael Nosonovsky, " Contact angle hysteresis in multiphase systems ", *Colloid and Polymer Science journal*, 2012, DOI: 10.1007/s00396-012-2838-0.
- ❖ Michael Nosonovsky and Vahid Hejazi, " Why superhydrophobic surfaces are not always Icephobic ", *ACS Nano*, 2012, DOI: 10.1021/nn302138r.
- ❖ V. Hejazi, A. E. Nyong, P. K. Rohatgi, M. Nosonovsky, " Wetting transition in underwater oleophobic surface of brass ", *Advanced Material*, 2012, DOI: 10.1002/adma.201202516.
- ❖ Vahid Hejazi, Michael Nosonovsky, " Wetting transition in two-, three- and four phase systems", *Langmuir*, 2012, 28 (4), pp 2173–2180.

- ❖ Michael Nosonovsky, Vahid Hejazi, Aniedi E. Nyong, Pradeep K. Rohatgi, "Metal Matrix Composites for Sustainable Lotus-Effect Surfaces", *Langmuir*, 2011, 27 (23), pp 14419–14424.
- ❖ V.Hejazi, M.A. Akhavan-Behabadi and A. Afshari, "Experimental investigation of twisted tape inserts performance on condensation heat transfer enhancement and pressure drop", *International Communication in Heat and Mass Transfer Journal*, Vol. 37, Issue. 9, pp. 1376-1387, Nov 2010.
- ❖ M.A. Akhavan-Behabadi and V. Hejazi, "Evaluation of Twisted Tapes Performance in Enhancement of Condensing Heat Transfer and Pressure Drop", *Journal of University College of Engineering*, University of Tehran, Vol.43, Issue 1, pp. 1-9, 2009.
- ❖ M.A. Akhavan-Behabadi and Vahid Hejazi, "Prediction of Pressure Drop of Two Phase Swirl Flow in Condensers", *Amirkabir Journal*, Amirkabir University of Technology, I.R. Iran, Vol. 19, No. 68b, pp. 45-52, June 2008.

CONFERENCE PAPERS

- ❖ Michael Nosonovsky, Vahid Hejazi, Pradeep K. Rohatgi, Aniedi E. Neyong, Emanuel Wornyo, " Sustainable Lotus-Effect Metal Matrix Composites and Influence of Wear on the Contact Angle", ASME/STLE International Joint Tribology Conference, Los Angeles, USA, October 24-26, 2011.
- ❖ V. Hejazi, M.A. Akhavan-Behabadi and S.G. Mohseni, "An Empirical Investigation on Convective Condensation Pressure Drop inside a Twisted Tape Inserted Tube", 12th Fluid Dynamics Conference, Babol, I.R. Iran, April 28-30, 2009.
- ❖ M.A. Akhavan-Behabadi, Vahid Hejazi, Vahid Akbari-Pazouki and S. Mohseni-Garakani, "Augmentation of Convective Condensation Heat Transfer and Pressure Drop by Twisted Tape and Coiled Wire Inserts", 11th. Fluid Dynamics Conference, Tehran, I.R. Iran, May 27-29, 2008.

BOOK CHAPTERS

- ❖ Michael Nosonovsky, Vahid Hejazi, Vahid Mortazavi, "Green and biomimetic tribology", 2013, Tribology for scientists and engineers.
- ❖ Vahid Mortazavi, Vahid Hejazi, Roshan D' Souza, Michael Nosonovsky, "Computational and experimental study of contact angle hysteresis in multiphase systems", 2013, Advances in contact angles, wettability and adhesion, Edited by K. L. Mittal.
- ❖ Vahid Hejazi and Michael Nosonovsky, "Wear resistant and oleophobic biomimetic composite materials", Green Tribology, Springer, 2012, XV, 931p. 329 illus.

PUBLISHED REPORT

- ❖ Konstantin Sobolev, Michael Nosonovsky, Tom Krupenkin, Ismael Flores-Vivian, Sunil Rao, Marina Kozhukhova, Vahid Hejazi, Scott Muzenski, Brandon Bosch, Rossana Rivero, "Anti-Icing and De-Icing Superhydrophobic Concrete to Improve the Safety on Critical Elements of Roadway Pavements", National Center for Freight & Infrastructure Research & Education (CFIRE 07-03), Sep 2013.

MEMBERSHIP

- ❖ American Society of Mechanical Engineers (ASME)
- ❖ Society of Tribologists and Lubrication Engineers (STLE)
- ❖ American Chemical Society (ACS)

- ❖ American Society of Heating, Refrigerating and Air Conditioning Engineers (ASHRAE)
- ❖ American Physical Society (APS)
- ❖ American Ceramic Society (ACerS)
- ❖ Iranian Society of Heating, Ventilation and Air Conditioning Systems Engineers.
- ❖ Iranian Society of Mechanical Engineers.